Rational Catalyst Design for Carbon Nanotube Carpet Growth and Fischer-Tropsch Synthesis

by

Xu Li

B.S., Beijing University of Chemical Technology, 2013

AN ABSTRACT OF A DISSERTATION

submitted in partial fulfillment of the requirements for the degree

DOCTOR OF PHILOSOPHY

Tim Taylor Department of Chemical Engineering
College of Engineering

KANSAS STATE UNIVERSITY
Manhattan, Kansas

2019

Abstract

The first part of this research involves the growth of vertically aligned carbon nanotube (CNT) arrays (or CNT carpets) that are desired in many important applications. Growth of high-quality, dense CNT carpets via catalytic chemical vapor deposition (CCVD) has been largely limited to catalysts supported on amorphous alumina or silica. Although catalyst design and CCVD process optimization have been extensively investigated, scalable growth of CNT carpets especially on nontraditional substrates remains largely a challenge. To develop a rational basis for designing efficient CNT catalysts, a deeper understanding of the role of substrates in CNT carpet growth during CCVD is required. In this study, a fundamental investigation of the effects of substrate properties on CNT carpet growth from supported catalysts under different reaction conditions and feedstock is carried out. To illuminate the interrelationships between properties of catalyst supporting layers on CNT carpet growth behaviors, CNT growth experiments from Fe catalyst supported on a variety of nontraditional substrates including stainless steel (SS), MgO, $MgAl_2O_4$ (100, 110, and 111 crystalline phases), and ZrO_2 were carried out. This study reveals that ion beam bombardment of 316 SS decreases the film thickness of Al_xO_y required for CNT growth to 5 nm Al_xO_y. The role of ion beam bombardment is to transform a highly crystalline surface into an amorphous surface, resulting in favorable catalyst-substrate interactions that enhances CNT growth. Our results reveal that Fe catalyst supported on different phases of $MgAl_2O_4$ spinel substrates show different CNT growth behaviors due to their different surface chemistries and surface energies.

The second part of this research is motivated by the drive to seek new routes that yield clean fuels and chemicals via Fischer-Tropsch synthesis (FTS). FTS provides a pathway for the transformation of biomass, coal or natural gas into fuels and chemicals using a transition metal

catalyst. Co-based catalysts are of interest because they exhibit relatively higher activity and selectivity to long-chain paraffins, high resistance to deactivation, and a low water-gas shift (WGS) reaction activity. Catalytic performance is sensitive to the catalyst preparation method and type of catalyst precursor. To investigate the effect of the type of catalyst precursor used during synthesis on physicochemical properties and efficiency of FTS process, SiO_2-supported Co catalysts were synthesized via an incipient wetness impregnation method from four different precursors: $Co(NO_3)_2$ (Co-Nit), $Co(C_2H_3O_2)_2$ (Co-Ace), $CoCl_2$ (Co-Chl), and $Co(OH)_2$ (Co-Hyd). This study reveals the type of Co precursor used during synthesis has significant effects on catalyst dispersion, size, crystalline phase, reducibility, stability, and FTS performance (CO conversion, C5+ selectivity, turnover frequency, and catalyst lifetime). Prenatal and postmortem characterization of the catalyst reveal sintering and formation of Co_2C in all catalysts except Co-Nit, which may explain the various degrees of deactivation observed. Further, XANES and EXAFS data confirm the superior structural stability of Co-Hyd and presence of hydroxyl groups even after reaction.

Rational Catalyst Design for Carbon Nanotube Carpet Growth and Fischer-Tropsch Synthesis

by

Xu Li

B.S., Beijing University of Chemical Technology, 2013

A DISSERTATION

submitted in partial fulfillment of the requirements for the degree

DOCTOR OF PHILOSOPHY

Tim Taylor Department of Chemical Engineering
College of Engineering

KANSAS STATE UNIVERSITY
Manhattan, Kansas

2019

Approved by:

Major Professor
Placidus B. Amama

Copyright

Abstract

The first part of this research involves the growth of vertically aligned carbon nanotube (CNT) arrays (or CNT carpets) that are desired in many important applications. Growth of high-quality, dense CNT carpets via catalytic chemical vapor deposition (CCVD) has been largely limited to catalysts supported on amorphous alumina or silica. Although catalyst design and CCVD process optimization have been extensively investigated, scalable growth of CNT carpets especially on nontraditional substrates remains largely a challenge. To develop a rational basis for designing efficient CNT catalysts, a deeper understanding of the role of substrates in CNT carpet growth during CCVD is required. In this study, a fundamental investigation of the effects of substrate properties on CNT carpet growth from supported catalysts under different reaction conditions and feedstock is carried out. To illuminate the interrelationships between properties of catalyst supporting layers on CNT carpet growth behaviors, CNT growth experiments from Fe catalyst supported on a variety of nontraditional substrates including stainless steel (SS), MgO, $MgAl_2O_4$ (100, 110, and 111 crystalline phases), and ZrO_2 were carried out. This study reveals that ion beam bombardment of 316 SS decreases the film thickness of Al_xO_y required for CNT growth to 5 nm Al_xO_y. The role of ion beam bombardment is to transform a highly crystalline surface into an amorphous surface, resulting in favorable catalyst-substrate interactions that enhances CNT growth. Our results reveal that Fe catalyst supported on different phases of $MgAl_2O_4$ spinel substrates show different CNT growth behaviors due to their different surface chemistries and surface energies.

The second part of this research is motivated by the drive to seek new routes that yield clean fuels and chemicals via Fischer-Tropsch synthesis (FTS). FTS provides a pathway for the transformation of biomass, coal or natural gas into fuels and chemicals using a transition metal

catalyst. Co-based catalysts are of interest because they exhibit relatively higher activity and selectivity to long-chain paraffins, high resistance to deactivation, and a low water-gas shift (WGS) reaction activity. Catalytic performance is sensitive to the catalyst preparation method and type of catalyst precursor. To investigate the effect of the type of catalyst precursor used during synthesis on physicochemical properties and efficiency of FTS process, SiO_2-supported Co catalysts were synthesized via an incipient wetness impregnation method from four different precursors: $Co(NO_3)_2$ (Co-Nit), $Co(C_2H_3O_2)_2$ (Co-Ace), $CoCl_2$ (Co-Chl), and $Co(OH)_2$ (Co-Hyd). This study reveals the type of Co precursor used during synthesis has significant effects on catalyst dispersion, size, crystalline phase, reducibility, stability, and FTS performance (CO conversion, C5+ selectivity, turnover frequency, and catalyst lifetime). Prenatal and postmortem characterization of the catalyst reveal sintering and formation of Co_2C in all catalysts except Co-Nit, which may explain the various degrees of deactivation observed. Further, XANES and EXAFS data confirm the superior structural stability of Co-Hyd and presence of hydroxyl groups even after reaction.

Table of Contents

List of Figures

List of Tables

Acknowledgements

I would like to express my sincere gratitude to my advisor Dr. Placidus B. Amama for his generous support, guidance and encouragement throughout my Ph.D. I am especially indebted to him for his guidance in both professional development and personal growth. He has always been inspirational to me for his vision, dedication, and knowledge and moral. I could not have imagined having a better advisor and mentor for my Ph.D. study. Many thanks to all my committee members Dr. James H. Edgar, Dr. Keith Hohn, Dr. Jun Li and outside chair Dr. Jeremy Schmit for their professional guidance and help. I am grateful to all my group members whom I have had the pleasure to work during my Ph.D. for their advice and help. I must acknowledge Dr. Haider Almkhelfe and Dr. Huan Wang for their invaluable help in my research. I would like to thank to Dr. Quanxing Zheng and Jiahan Li for their help in different characterizations.

No words are adequate to express my feelings towards my parents Mr. Donghua Li and Mrs. Yan Wang whose unconditional love, support, blessing and affection is the source of inspiration and encouragement for my studies. I am extremely obliged to my parents for their love, caring and sacrifices for educating and preparing me for my future. Most importantly, special thanks to my wife Dr. Mingxia Zhou. Her love and support have kept me strong even during the most difficult days.

I also would like to extend thanks and appreciation to everyone who helped directly or indirectly to my Ph.D.

Chapter 1 - Introduction

1.1 Introduction

A carbon nanotube (CNT) is a graphene sheet rolled up to form a cylindrical structure with a diameter on the nanometer scale. Structures formed with a single layer of graphene are called single-wall CNTs (SWCNTs) [1] while structures roll up with two or more layers of graphene sheets are multi-wall CNTs (MWCNTs) [2]. Since CNTs were first observed by Iijima in 1991 [2], they have continued to attract great attention due to their excellent material properties including high mechanical strength, excellent electrical and thermal conductivity, and good thermal stability [3]. Anticipated applications of CNTs are broadening in various areas ranging from energy storage [4, 5], thermally conductive materials [6, 7], catalysis [8, 9] to sensing devices [10, 11]. Given the strong dependence of CNT properties on its geometry, many applications not only require scalable amounts of CNTs, but also highly uniform CNTs with specific geometries. Therefore, the development of an efficient technique for controlled synthesis of CNTs remains a major requirement for successful and widespread application of CNTs.

Concerns about dwindling crude oil reserves and their negative impact on the environment are forcing researchers to seek new routes that yield clean fuels and chemicals [12, 13]. The conversion of natural gas to higher hydrocarbons via Fischer-Tropsch synthesis (FTS) is of great interest due to the increasing demand for clean fuels. The model catalyst used in FT synthesis is typically prepared by dispersing a Co precursor on porous SiO_2, Al_2O_3 or activated carbon. Co-based catalysts exhibit relatively higher activity and selectivity to long-chain paraffins, high resistance to deactivation, and a low water-gas shift (WGS) reaction activity [14, 15]. While reasonable catalytic performance can be achieved with SiO_2- and Al_2O_3-supported Co catalysts, there are fundamental problems associated with these catalysts that have hampered

efforts in further improving the FTS process: (1) SiO_2-supported Co catalysts are characterized by relatively weak catalyst-support interactions that leads to better Co reducibility, but lower Co dispersion; conversely, the catalyst-support interactions in Al_2O_3-supported Co catalysts are stronger, which results in highly dispersed small Co crystallites that react with the substrate to form cobalt aluminate spinel [16-18]. The Co compounds or mixed oxides formed in the latter are catalytically inactive and can only be reduced at elevated temperatures (exceeding 1000 K) [19, 20]. (2) Even though an enormous amount of work has been dedicated to improving the dimensions and accessibility of the pores of SiO_2, Al_2O_3 and activated carbon supports, their pores are still largely limited to sub-nanometer scale, which limits mass transport of the reactants and products inside the catalyst matrix [20]. (3) Further, the heat produced during the exothermic FTS reaction is not well dissipated in the presence of catalysts supported on the relatively poor thermally conductive SiO_2, Al_2O_3 and activated carbon supports, resulting in a temperature gradient in the packed bed reactors. To mitigate these problems and improve the FTS process, a catalyst support that is characterized by mesoporosity, high thermal conductivity and the possibility of achieving favorable catalyst-support interactions via surface modification is required.

We have demonstrated that cobalt hydroxide is a promising precursor for synthesis of well-dispersed Co catalysts on CNTs via a modified photo-Fenton process [21]. The resulting CNT-supported Co catalyst does not require a calcination step due to the absence of possible catalyst inhibitors usually present in conventional catalyst precursors such as nitrates, chlorides, acetates, and carbonyls. The use of the as-synthesized catalyst (without calcination) in FTS reaction resulted in high CO conversion (~80%) and outstanding C5+ selectivity (~70%). An important point to note is, while a number of Co precursors have been used for synthesis of Co

catalysts on SiO_2 support [22-26], there is not a single study involving the use of cobalt hydroxide as a precursor. Also, fundamental questions related to how the type of metal precursor affects catalyst reducibility, hydrocarbon product distribution, and catalyst lifetime remain unanswered.

The *goal of this study* is to conduct fundamental investigations towards the development of unconventional routes to synthesize well-dispersed FT catalysts (free of agglomeration) with superior performance (higher activity, longer lifetime, and higher C5+ selectivity) than current conventional catalysts. Our strategy for achieving this goal involves the use of a 'green' catalyst precursor [$Co(OH)_2$] and CNT matrix as a catalyst support. A precursory part of this goal is to establish an efficient process for scalable growth of CNTs that will be used as catalyst supports in packed-bed reactors during FTS. The study is guided by the following objectives:

- Investigate the effect of substrate modification on CNT growth behavior (CNT nucleation density, catalyst activity, and catalyst lifetime). The hypothesis is that activity and lifetime of catalysts during CNT carpet growth can be enhanced by high surface porosity and Lewis basicity of the catalyst supporting layers. The strategies for creating porosity and basicity in "inactive substrates" are ion beam bombardment and deposition of a thin alumina layer, respectively.
- Investigate the combined effect of using a gaseous waste mixture (products) from FTS (FTS-GP) and an engineered catalyst on CNT carpet yield and properties. The following hypothesis, which is supported by our experimental data, is evaluated: The unique composition of FTS-GP, consisting of C1-C4 saturated and unsaturated hydrocarbon and unreacted syngas (CO and H_2), enables the feedstock and resulting gas-phase species to maintain the required balance between oxygenated species and carbon atoms over a wide

parameter space. The oxygenated species serve as a cleaning agent that oxidizes amorphous carbon from the catalyst surface while the high flux of carbon atoms to the catalysts contribute to the growth of CNTs.

- Design efficient SiO_2- and CNT-supported Co catalysts for FTS process and establish systematic inter-relationships between the catalyst structure as a whole (active phase and support) and the catalyst behavior (activity, lifetime, and product selectivity) in FTS. The hypothesis of this task is that catalyst properties, activity, and selectivity are sensitive to the type of support and catalyst precursor used during synthesis.
- Acquire a better molecular-level understanding of the (1) formation of Co oxide and carbidic species on SiO_2 and CNTs during the FTS and (2) reducibility and deactivation mechanisms of Co catalyst supported on CNTs and SiO_2.

The proposed research is expected to contribute an in-depth understanding of catalyst-substrate interactions and catalyst evolution under different reaction conditions in FTS and CNT carpet growth. Synthesis techniques will be implemented based on the new mechanistic insights derived from our fundamental studies to increase catalyst dispersion and formation of active sites via a photo-Fenton process in FTS process and improve CNT carpet growth efficiency. The body of knowledge developed from this study is expected to have broad applicability: (1) enabling rational development of guidelines for scalable production of CNT carpets with controlled properties on nontraditional substrates such as metallic, dielectric, and non-alumina oxidic substrates; (2) establishing a rational basis for producing CNT-supported Co catalysts in FTS and related hydrocarbon reactions.

Chapter 2 focuses on the modification of stainless steel (SS), a well-known inactive substrate for CNT growth, via a two-step process involving ion beam bombardment and

deposition of a thin Al_xO_y layer. The modification approach implemented in this study results in dense growth of CNT arrays on SS. In particular, our results show that ion beam bombardment of 316 SS decreases the film thickness of Al_xO_y required for CNT growth to 5 nm Al_xO_y, a thickness that does not impede electronic transport across the barrier.

Chapter 3 builds upon our work presented in chapter 2 [27] and focuses on CNT growth from catalyst supported on substrates with different properties (composition, crystalline phase, Lewis basicity, and surface porosity). Interrelationships between physicochemical properties of the different catalyst supports (before and after ion beam bombardment) and CNT growth behavior were established for the first time. A comparison between the growth profiles from FTS-GP CVD and conventional CVD (C_2H_4 CVD) was carried out to determine the growth efficiency of our newly developed process. The time evolution of CNT carpet growth is modeled using the radioactive-decay equation [28]; by fitting to our growth data, we were able to determine catalyst lifetime and initial growth rate. Our results show the use of FTS-GP as a feedstock for CNT carpet growth enhances catalyst lifetime and CNT growth rate. We attribute the excellent performance of FTS-GP (or FTS-GP CVD) to the combined high flux of carbon to the catalyst and possible in situ generation of H_2O at the catalyst site during growth that prevents deactivation induced by coking. This study has provided new insights into the activity and carbon selectivity of several catalyst-substrate combinations in FTS-GP CVD, a new CVD process designed by our group.

In Chapter 4, we have investigated the properties and performance of SiO_2- and CNT-supported Co catalysts synthesized via incipient wetness impregnation method using different Co precursors derived from $Co(OH)_2$, $Co(NO_3)_2$, $Co(C_2H_3O_2)_2$, and $CoCl_2$. The synthesized catalysts are characterized using a wide range of techniques including transmission electron microscopy

(TEM), X-ray diffraction (XRD), temperature-programmed reduction (TPR), X-ray photoelectron spectroscopy (XPS), and X-ray absorption spectroscopy (XAS). The catalytic performance (CO conversion, turnover frequency, and product distribution) and stability of the synthesized catalysts during FTS are evaluated and compared. The results reveal that catalysts from $Co(OH)_2$ outperforms other catalysts from the other precursors. Further, post-mortem characterization of the catalysts are conducted using TEM, XAS, and XRD to elucidate the structural and chemical changes.

1.2 References

[1] S. Iijima, T. Ichihashi, Single-shell carbon nanotubes of 1-nm diameter, *Nature*, 363 (1993) 603.

[2] S. Iijima, Helical microtubules of graphitic carbon, *Nature*, 354 (1991) 56.

[3] R. Saito, G. Dresselhaus, M.S. Dresselhaus, Physical properties of carbon nanotubes, World Scientific1998.

[4] W. Wang, P.N. Kumta, Nanostructured hybrid silicon/carbon nanotube heterostructures: reversible high-capacity lithium-ion anodes, *ACS Nano*, 4 (2010) 2233-2241.

[5] C.L. Pint, N.W. Nicholas, S. Xu, Z. Sun, J.M. Tour, H.K. Schmidt, R.G. Gordon, R.H. Hauge, Three dimensional solid-state supercapacitors from aligned single-walled carbon nanotube array templates, *Carbon*, 49 (2011) 4890-4897.

[6] H. Chen, M. Chen, J. Di, G. Xu, H. Li, Q. Li, Architecting three-dimensional networks in carbon nanotube buckypapers for thermal interface materials, *The Journal of Physical Chemistry C*, 116 (2012) 3903-3909.

[7] B.A. Cola, J. Xu, C. Cheng, X. Xu, T.S. Fisher, H. Hu, Photoacoustic characterization of carbon nanotube array thermal interfaces, *Journal of Applied Physics*, 101 (2007) 054313.

[8] W. Li, C. Liang, W. Zhou, J. Qiu, Z. Zhou, G. Sun, Q. Xin, Preparation and characterization of multiwalled carbon nanotube-supported platinum for cathode catalysts of direct methanol fuel cells, *The Journal of Physical Chemistry B*, 107 (2003) 6292-6299.

[9] K. Gong, F. Du, Z. Xia, M. Durstock, L. Dai, Nitrogen-doped carbon nanotube arrays with high electrocatalytic activity for oxygen reduction, *Science*, 323 (2009) 760-764.

[10] K. Saetia, J.M. Schnorr, M.M. Mannarino, S.Y. Kim, G.C. Rutledge, T.M. Swager, P.T. Hammond, Spray‐Layer‐by‐Layer Carbon Nanotube/Electrospun Fiber Electrodes for

Flexible Chemiresistive Sensor Applications, *Advanced Functional Materials*, 24 (2014) 492-502.

[11] E. Llobet, Gas sensors using carbon nanomaterials: A review, *Sensors and Actuators B: Chemical*, 179 (2013) 32-45.

[12] M.E. Dry, The fischer–tropsch process: 1950–2000, *Catalysis Today*, 71 (2002) 227-241.

[13] H. Jahangiri, J. Bennett, P. Mahjoubi, K. Wilson, S. Gu, A review of advanced catalyst development for Fischer–Tropsch synthesis of hydrocarbons from biomass derived syn-gas, *Catalysis Science & Technology*, 4 (2014) 2210-2229.

[14] G.L. Bezemer, J.H. Bitter, H.P. Kuipers, H. Oosterbeek, J.E. Holewijn, X. Xu, F. Kapteijn, A.J. van Dillen, K.P. de Jong, Cobalt particle size effects in the Fischer− Tropsch reaction studied with carbon nanofiber supported catalysts, *Journal of the American Chemical Society*, 128 (2006) 3956-3964.

[15] J.-S. Girardon, E. Quinet, A. Griboval-Constant, P. Chernavskii, L. Gengembre, A. Khodakov, Cobalt dispersion, reducibility, and surface sites in promoted silica-supported Fischer–Tropsch catalysts, *Journal of Catalysis*, 248 (2007) 143-157.

[16] A.Y. Khodakov, W. Chu, P. Fongarland, Advances in the Development of Novel Cobalt Fischer−Tropsch Catalysts for Synthesis of Long-Chain Hydrocarbons and Clean Fuels, *Chemical Reviews*, 107 (2007) 1692-1744.

[17] G. Jacobs, T.K. Das, Y. Zhang, J. Li, G. Racoillet, B.H. Davis, Fischer–Tropsch synthesis: support, loading, and promoter effects on the reducibility of cobalt catalysts, *Applied Catalysis A: General*, 233 (2002) 263-281.

[18] P.J. van Berge, J. van de Loosdrecht, S. Barradas, A.M. van der Kraan, Oxidation of cobalt based Fischer–Tropsch catalysts as a deactivation mechanism, *Catalysis Today*, 58 (2000) 321-

334.

[19] R.C. Reuel, C.H. Bartholomew, Effects of support and dispersion on the CO hydrogenation activity/selectivity properties of cobalt, *Journal of Catalysis*, 85 (1984) 78-88.

[20] P. Serp, M. Corrias, P. Kalck, Carbon nanotubes and nanofibers in catalysis, *Applied Catalysis A: General*, 253 (2003) 337-358.

[21] H. Almkhelfe, X. Li, P. Thapa, K.L. Hohn, P.B. Amama, Carbon nanotube-supported catalysts prepared by a modified photo-Fenton process for Fischer–Tropsch synthesis, *Journal of Catalysis*, 361 (2018) 278-289.

[22] S. Sun, N. Tsubaki, K. Fujimoto, The reaction performances and characterization of Fischer–Tropsch synthesis Co/SiO2 catalysts prepared from mixed cobalt salts, *Applied Catalysis A: General*, 202 (2000) 121-131.

[23] N. Tsubaki, S. Sun, K. Fujimoto, Different Functions of the Noble Metals Added to Cobalt Catalysts for Fischer–Tropsch Synthesis, *Journal of Catalysis*, 199 (2001) 236-246.

[24] J.S. Girardon, E. Quinet, A. Griboval-Constant, P.A. Chernavskii, L. Gengembre, A.Y. Khodakov, Cobalt dispersion, reducibility, and surface sites in promoted silica-supported Fischer–Tropsch catalysts, *Journal of Catalysis*, 248 (2007) 143-157.

[25] J.-S. Girardon, A.S. Lermontov, L. Gengembre, P.A. Chernavskii, A. Griboval-Constant, A.Y. Khodakov, Effect of cobalt precursor and pretreatment conditions on the structure and catalytic performance of cobalt silica-supported Fischer–Tropsch catalysts, *Journal of Catalysis*, 230 (2005) 339-352.

[26] J.W. Bae, S.-M. Kim, S.-H. Kang, K.V. Chary, Y.-J. Lee, H.-J. Kim, K.-W. Jun, Effect of support and cobalt precursors on the activity of $Co/AlPO_4$ catalysts in Fischer–Tropsch synthesis, *Journal of Molecular Catalysis A: Chemical*, 311 (2009) 7-16.

[27] X. Li, M. Baker-Fales, H. Almkhelfe, N.R. Gaede, T.S. Harris, P.B. Amama, Rational Modification of a Metallic Substrate for CVD Growth of Carbon Nanotubes, *Scientific Reports*, 8 (2018) 4349.

[28] D.N. Futaba, K. Hata, T. Yamada, K. Mizuno, M. Yumura, S. Iijima, Kinetics of Water-Assisted Single-Walled Carbon Nanotube Synthesis Revealed by a Time-Evolution Analysis, *Physical Review Letters*, 95 (2005) 056104.

Chapter 2 - Rational Modification of a Metallic Substrate for CVD Growth of Carbon Nanotubes

Chapter 2 is reproduced in part with permission from:

X. Li, M. Baker-Fales, H. Almkhelfe, N. R. Gaede, T. S. Harris, P. B. Amama, Rational Modification of a Metallic Substrate for CVD Growth of Carbon Nanotubes, Scientific Reports 8 (2018) 4349.

2.1 Introduction

To harness the unique properties of carbon nanotube (CNT) arrays for applications in energy storage and thermal management, it is necessary for them to be supported on metallic substrates. Hitherto, efficient growth of high quality, dense CNT arrays via catalytic chemical vapor deposition (CCVD) occurs mainly from a catalyst supported on an insulator such as amorphous alumina (Al_xO_y) or silica, which is usually unsuitable in applications that require electrically conductive substrates such as energy storage [1, 2], thermal interface materials [3, 4], and sensing devices [5, 6]. On the other hand, extending the high CNT growth efficiency observed on alumina to non-alumina supports such as metals has remained a challenge for a number of reasons. First, high surface energies of metallic substrates hamper formation of catalyst nanoparticles during the annealing process [7-9]. Second, metallic substrates are unable to stabilize the catalyst and prevent high rates of intermetallic diffusion and catalyst poisoning that typically occurs during CNT growth [10-12]. Therefore, significant interest exists in developing rational modification approaches that transform nontraditional “inactive” substrates to “active” substrates with physicochemical properties that support high CNT nucleation and growth.

CNT growth on metallic substrates such as Al [13], Cu [14], Inconel [15], and stainless steel (SS) [16] has been achieved through implementation of different strategies. A commonly used strategy involves depositing a barrier layer, such as Ti [14] or Al_2O_3 [15-17], that is sandwiched between a layer of catalyst (Ni [13, 14] or Fe [15, 16]) at the top and metallic substrate at the bottom. The barrier layer prevents direct interaction of the catalyst with the underlying metal to prevent the problems delineated above. For metallic substrates that contain an active catalyst for CNT growth such as SS and Inconel, direct CNT growth is possible (without deposition of a catalyst) after conducting specific surface modification or pretreatment. Pretreatment methods investigated include acid-etching using HCl [16, 18] or H_2SO_4 [19], plasma treatment [20, 21], air annealing [22-24], Ar ion bombardment [25], and magnetron sputtering [26]. All these methods favor formation of catalyst particles on the substrate that serve as seeds for CNT growth. Based on studies involving CNT growth on different types of SS (316 SS and 304 SS), catalytic activity of pretreated SS during CNT growth shows high sensitivity to the composition of SS. The type of SS used in our study is 316 SS contains 2–3% Mo to enhance its corrosion resistance and thermal stability [24]. The presence of Mo in 316 SS makes it a relatively inactive substrate for CNT growth [27]. Conversely, 304 SS contains no Mo and is active for CNT growth; in fact, a number of prior studies [16, 19, 22] involving direct CNT growth on SS utilize 304 SS as the growth substrate.

In this study, we focus on modification of 316 SS, a well-known inactive substrate for CNT growth, via a two-step process involving ion beam bombardment and deposition of a thin Al_xO_y layer (Figure 2.1). The modification approach implemented in this study results in growth of CNT arrays on 316 SS. The approach is inspired by previous investigations [28-32] on the role of Al_xO_y as a catalyst support in CNT carpet growth, whereby the high growth efficiency for

a supported Fe catalyst was attributed to the combined effects of surface porosity and Lewis basicity of Al_xO_y. In particular, our results show that ion beam bombardment of 316 SS decreases the film thickness of Al_xO_y required for CNT growth to 5 nm Al_xO_y, a thickness that does not impede electronic transport across the barrier [17, 33]. In elucidating the role of ion beam bombardment in CNT growth, we have focused on probing the evolution of the catalyst during CCVD, given that prior studies [34-37] have illuminated the effect of ion beam bombardment on substrates including SS.

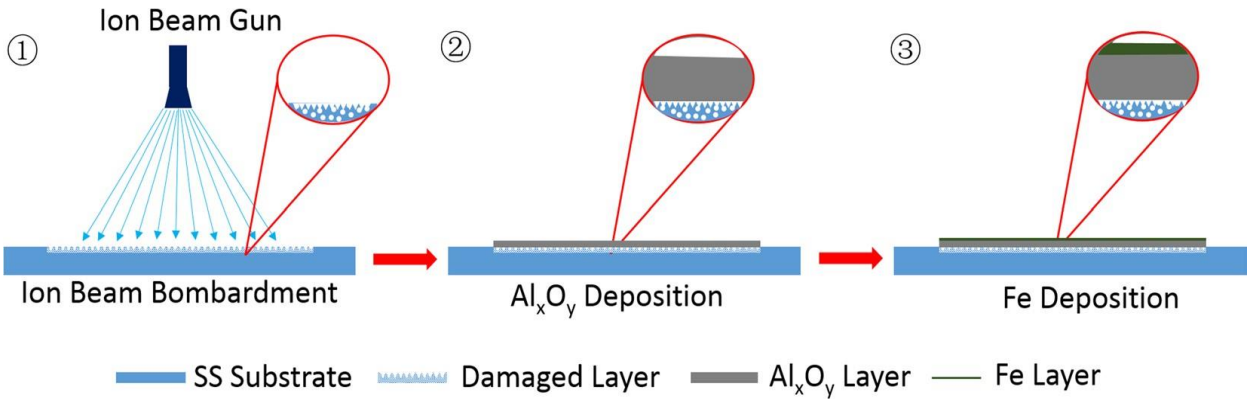

Figure 2.1 A schematic illustration of ion beam bombardment of SS (Step 1), Al_xO_y deposition on the damaged surface (Step 2) followed by Fe deposition (Step 3).

2.2 Experimental

2.2.1 Materials and Preparation

316 SS substrates used as catalyst supports were modified by ion beam bombardment in an ion beam sputter deposition and etching system (IBS/e) obtained from South Bay Technology. The substrates were placed directly opposite the Ar ion source (spot size ~3 mm) with adjustments made to ensure the beam line is perpendicular to the substrate. Ion beam damage was conducted for 10 min at an acceleration voltage of 6 kV and a beam current of 3.5 mA. The total ion dose was calculated to be 1.85×10^{18} cm^{-2} [28]. Thereafter, damaged and pristine SS

substrates were deposited with different thicknesses of Al_xO_y films (0, 5, 10, and 20 nm). A thin Fe catalyst film with a nominal thickness of 1 nm was then deposited on each SS-supported Al_xO_y layer. The Al_xO_y and Fe films were sequentially deposited on substrates in the IBS/e without exposure to air.

2.2.2 CVD Growth

CNT growth was carried out at atmospheric pressure using an EasyTube 101 CVD system (CVD Equipment Corporation) equipped with a LabView-based process control software, a static mixer for optimum gas mixing, and a precise temperature control system. A typical growth run involved heating the catalyst sample to 750 °C at a rate of 50 °C/min in a flowing Ar atmosphere. At the growth temperature, the sample was exposed to a copious amount of H_2 in combination with Ar for 10 min to reduce the catalyst; respective flow rates were 250 standard cubic centimeters per minute (sccm) H_2 and 250 sccm Ar. Thereafter, CNT growth was initiated by introducing the growth gas mixture (100 sccm C_2H_4, 250 sccm H_2, and 250 sccm Ar). At the end of growth, the samples were rapidly cooled in H_2, followed by slow cooling to room temperature in 700 sccm Ar.

2.2.3 Characterization

Raman spectra of products were collected at multiple spots from the samples using a Renishaw inVia Raman microscope with a 532-nm laser as the excitation source. Growth products and catalyst morphology were characterized with a Hitachi S5200 field-emission scanning electron microscope (SEM) operated at 5 kV. Transmission electron microscopic (TEM) images were obtained using FEI Tecnai F20 XT operating at 200 kV. The samples were

prepared by dispersing in ethanol by sonication for 5 min and dropping on a copper microgrid coated with lacy carbon film.

2.3 Results

2.3.1 Modification of SS

Surface porosity and basicity on 316 SS were created via a two-step process (Steps 1 and 2 in Figure 2.1) prior to catalyst deposition (Step 3). In Step 1, the 316 SS substrates were modified by ion beam bombardment, while in Step 2, the damaged and pristine SS substrates were deposited with different thicknesses of Al_xO_y films (0, 5, 10, and 20 nm). A thin Fe catalyst film with a nominal thickness of 1 nm was then deposited on each SS-supported Al_xO_y layer. Note that Al_xO_y and Fe films were sequentially deposited on two sets of SS samples: (1) Fe deposited on ion beam-damaged SS substrate with different thicknesses of Al_xO_y: 0 nm Al_xO_y (Damaged-0), 5 nm Al_xO_y (Damaged-5), 10 nm Al_xO_y (Damaged-10), and 20 nm Al_xO_y (Damaged-20). (2) Fe deposited on pristine SS substrate with different thicknesses of Al_xO_y: 0 nm Al_xO_y (Pristine-0), 5 nm Al_xO_y (Pristine-5), 10 nm Al_xO_y (Pristine-10), and 20 nm Al_xO_y (Pristine-20). The samples are hereinafter referred to by the condition of the SS surface (damaged or pristine) followed by thickness of the Al_xO_y barrier layer (in nanometers) as stated above in parentheses.

2.3.2 Effects of ion beam bombardment and Al_xO_y thickness on CNT growth

Figure 2.2 shows SEM images of products formed after CCVD on pristine and ion beam-damaged substrates with different Al_xO_y barrier layer thicknesses sandwiched between Fe catalysts and SS. Panel a in Figure 2.2 shows large Fe particles with no CNTs on Pristine-0.

Panel b shows poor and non-uniform CNT growth on Pristine-5, and the Fe catalyst particles appear to be covered with amorphous carbon as verified by Raman spectroscopy. For pristine SS samples, uniform and efficient CNT growth from Fe catalysts becomes apparent on Pristine-10 and denser on Pristine-20, as shown in panels c and d of Figure 2.2, respectively. In contrast, panel f shows a catalyst on damaged substrates start to grow CNTs with a barrier layer thickness of only 5 nm (Damaged-5), and become denser with increasing barrier layer thickness (Damaged-10 and Damaged-20). Although CNT density and growth uniformity was higher on Damaged-5 than Pristine-5, the density was still lower than what is required to create CNT carpets. Al_xO_y layer thickness of 20 nm was required for CNT carpet growth on damaged and pristine SS, albeit with higher CNT density on the former. A related work by Hiraoka et al. [17] demonstrated growth of single- and double-wall CNTs from catalyst supported on nickel alloy, 304 SS, and 310 SS substrates, albeit with a thicker alumina barrier layer (30 nm), further illustrating the difficulty in achieving CNT growth on metallic substrates with a thin barrier layer. SEM images of pristine and damaged SS demonstrate that surface modification via ion beam bombardment can in fact decrease the barrier layer thickness required for CNT growth, which may explain the successful growth of unaligned (5–10 nm-thick Al_xO_y) and vertically aligned CNTs (20 nm-thick Al_xO_y) on thinner alumina layers

in our study. As shown by Zhong et al. [33], a thin barrier thickness of $\leq$ 5 nm is within the threshold for the substrate to remain conductive. Therefore, with optimization of reaction conditions for each catalyst, this new approach can potentially benefit applications that require CNT arrays supported on a conductive substrate.

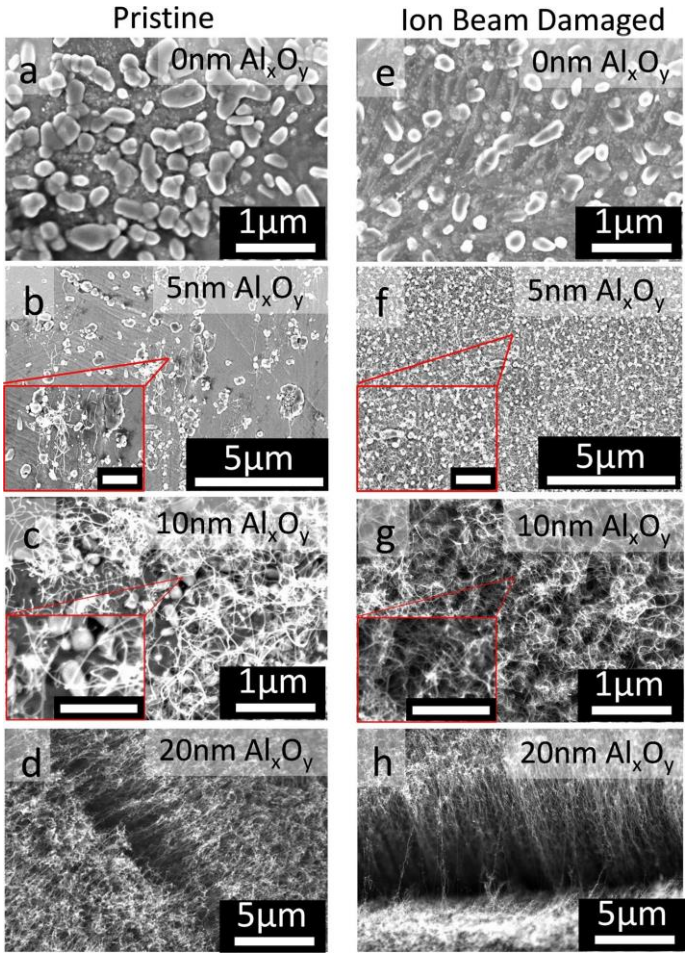

Figure 2.2 SEM characterization of SS surface after CCVD growth. Images of products formed on pristine and ion beam-damaged SS-supported Fe catalyst with different thicknesses of Al_xO_y after CNT growth process: (a) Pristine-0, (b) Pristine-5, (c) Pristine-10, (d) Pristine-20, (e) Damaged-0, (f) Damaged-5, (g) Damaged-10, and (h) Damaged-20. Scale bars of inserts in panels b and f are 1 µm while those of panels c and g are 500 nm.

The Raman spectra of products formed on the surface of pristine and ion beam-damaged substrates with different Al_xO_y barrier layer thicknesses after a CCVD process are shown in Figure 2.3. A photograph of the sample surface is placed beside each spectrum to show coverage of the growth product on SS. The Raman spectra show characteristic modes of CNTs: tangential stretch mode (G-band) at ~1593 cm^{-1} that represents the highly oriented lattice structure of graphitic carbon, and disorder-induced mode (D-band) around 1345 cm^{-1} that is indicative of the

presence of defects or amorphous carbon. The ratio of G-band to D-band intensities (I_G/I_D) has been used as an index to evaluate the quality of the grown CNTs, and the value for each spectrum is provided in Figure 2.3. Additionally, a shoulder on the right side of the G-band (~1600 cm^{-1}) is referred to as the D' line and is also indicative of disorders in the graphitic crystal structure [38, 39]. Raman spectra of Pristine-0, Pristine-5, and Damaged-0 samples have an additional peak at 660 cm^{-1}, which comes from the SS substrate. Unlike Pristine-0, Pristine-5, and Damaged-0, the absence of the D′peak and the peak at 660 cm^{-1} (attributed to SS) in the spectrum of Damaged-5 supports evidence from SEM data (Figure 2.2) that growth on this substrate is due to the combined effect of ion beam bombardment and presence of a thin Al_xO_y layer.

Pictures shown on the side of the Raman spectra reveal that carbon deposition during CCVD was limited to the circular area with ion beam bombardment even though the catalyst was deposited across the entire substrate; this result emphasizes the critical role played by ion beam bombardment in combination with a basic surface. Ion beam bombardment can induce changes in the surface and diffusion properties of the substrate as well as composition due to vacancies that may be created. From Figure 2.2, coverage of CNTs on pristine and damaged SS increases with barrier-layer thickness, which based on previous studies correlates with increased surface porosity and the basic environment provided by the Al_xO_y barrier layer [28-30, 32]. Also, from the Raman data in Figure 2.3, I_G/I_D for CNTs grown on pristine and damaged SS increase with Al_xO_y barrier layer thickness, indicating the quality of CNTs improves with increasing Al_xO_y thickness. Substrate basicity also enhances nanoparticle formation and stabilization during annealing and growth steps [29, 31, 40, 41]. Note that for the same Al_xO_y thickness, CNTs grown on damaged substrates have higher coverage and I_G/I_D demonstrating that ion beam

bombardment enhances CNT growth efficiency from Fe catalysts. We observed similar improvement in growth efficiency on c-cut sapphire substrates after ion beam bombardment, which was attributed to changes in Lewis basicity, porosity, and damage depth of substrates [28]. Note that unlike c-cut sapphire, in the present study, ion beam damage alone does not transform SS to an "active" catalyst support for CNT growth, as evidenced by the lack of growth on Damaged-0. In fact, Raman spectra of Damaged-0, Pristine-0, and Pristine-5 after CNT growth are characterized by G- and D-bands with relatively low signal-to-noise ratio and a signal ~660 cm^{-1} from the background; we attribute this observation to the low amount of carbon formed, causing most of the signal to emanate from the substrate.

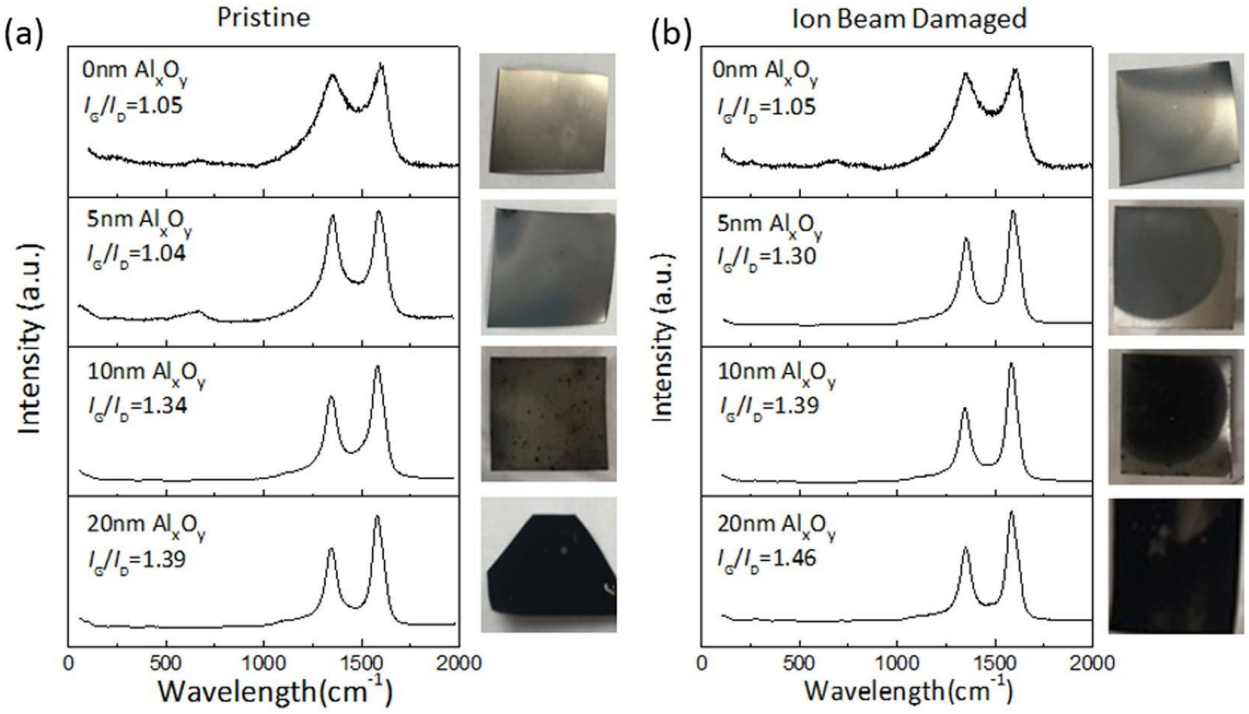

Figure 2.3. Characterization of products formed on pristine and ion beam-damaged SS. Raman spectra of products formed on pristine SS-supported Fe catalysts with different thicknesses of Al_xO_y barrier layer (a) and ion beam-damaged SS-supported Fe catalysts with different thicknesses of Al_xO_y barrier layer (b).

2.3.3 CNT growth rate and density

To investigate the effect of ion beam bombardment of SS on CNT growth efficiency, the heights of CNT carpets grown on Pristine-20 and Damaged-20 for various growth times, ranging from 10 to 120 min, were investigated. The results, presented in Figure 2.4, reveal that CNT carpets grown on Damaged-20 are taller than carpets grown on Pristine-20 especially at longer growth time (> 60 min) when catalysts become prone to deactivation. Growth rates of CNT carpets from catalysts supported on Pristine-20 and Damaged-20 catalysts are 1.08 μm/min and 1.92 μm/min, respectively. Modification of SS via ion beam bombardment enhances the CNT growth rate by almost a factor of two. It is noteworthy that the positive impact of ion beam bombardment is still apparent for a barrier-layer thickness of 20 nm, suggesting the influential role it plays in CNT growth.

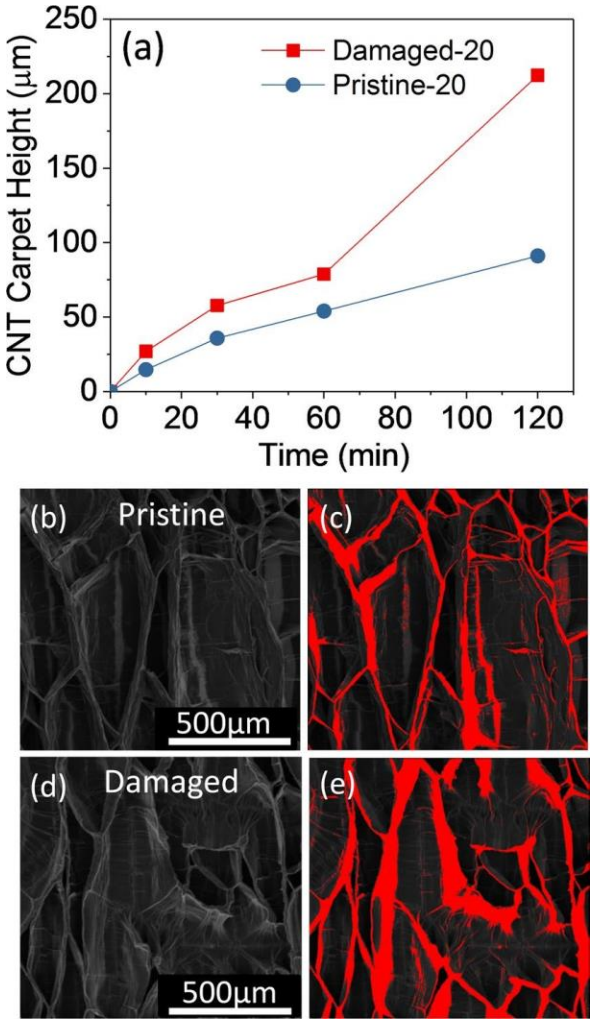

Figure 2.4. Growth properties of CNT carpets on pristine and ion beam-damaged SS. Plots of CNT carpet height as a function of growth time for Pristine-20 and Damaged-20 (a). SEM image of densified CNT carpets grown for 120 min from Fe catalyst supported on Pristine-20 (b) and its corresponding false-color image showing the densified region (c). SEM image of densified CNT carpets grown for 120 min from Fe catalyst supported on Damaged-20 (d) and its corresponding false-color image showing the densified region (e).

To determine the density of as-grown CNT carpets on Pristine-20 and Damaged-20 catalysts, we employed a solvent-induced densification method. The process involves soaking CNT carpets in ethanol, followed by drying in air. Thereafter, the CNT carpets were densified via capillary forces [42]. SEM images of the top view of CNTs grown on Pristine-20 and Damaged-20 catalyst are compared in Figure 2.4b and d, respectively; their respective red false-

color images showing the densified CNT carpets are presented on the right side (Figure 2.4c and e). Areal coverage of CNTs grown on Pristine-20 and Damaged-20 using ImageJ [43] for analysis are 18.05% and 27.10%, respectively. The results show that density of CNTs grown from catalysts on Damaged-20 is higher than CNTs obtained on Pristine-20. These results are consistent with data presented in Figure 2.3, whereby coverage of CNTs and amount of carbon deposited on SS can be evaluated. In agreement with SEM data, we observed from the pictures that for the same thickness of Al_xO_y barrier layer, ion beam-damaged substrate showed higher carbon coverage on the surface than the pristine substrate. In fact, quantification of the number of CNTs on Pristine-5 and Damaged-5 using their respective SEM images revealed an average density of 5 CNTs/μm^2 and 109 CNTs/ μm^2, respectively. Clearly, ion beam bombardment improves CNT density. Also, TEM images of CNTs obtained from catalysts supported on Pristine-20 and Damaged-20 (Figure 2.5) confirm that the structures are primarily CNTs and not nanofibers due to absence of a stacked cone or bamboo-like morphology along the inner cavity of the tube. Representative high-magnification TEM images of the wall structure of CNTs (inserts in Figure 2.5a) reveal that ion beam bombardment of SS prior to Al_xO_y and Fe depositions yield CNTs with higher structural quality. The insert in Figure 2.5a shows the presence of substantial defects on the wall of a CNT grown on Pristine-20 whereas the wall structure has less defects for the CNT grown on Damaged-20 (Figure 2.5b). The nature of the underlying layer still affects the growth properties of CNTs even for catalyst substrates with relatively thicker barrier layer.

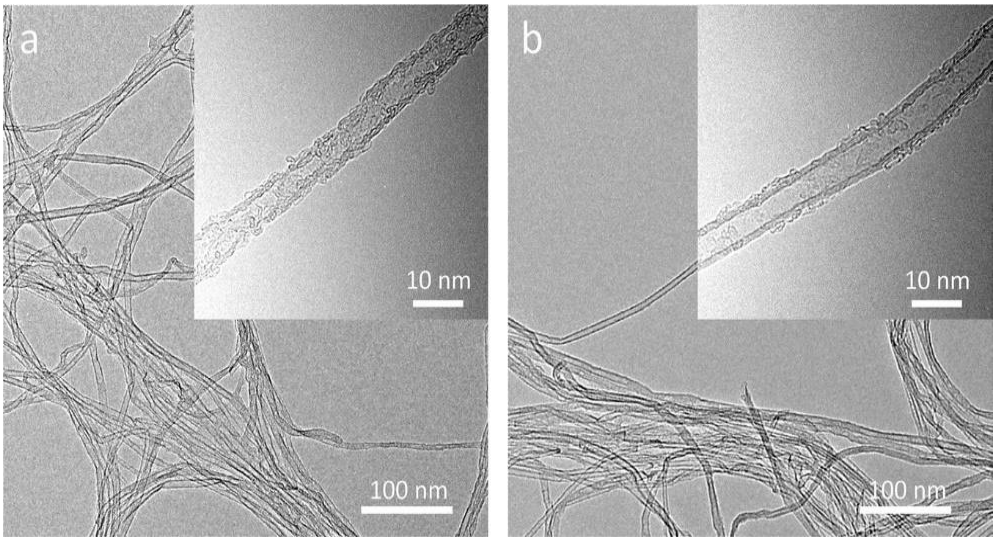

Figure 2.5. TEM images of CNTs after 120 min of growth. (a) CNT arrays grown from Fe catalyst supported on Pristine-20; the insert shows the defective wall of a CNT. (b) CNT arrays grown from Fe catalyst supported on Damaged-20; the insert shows a wall structure that has less defects.

2.3.4 Effects of ion beam bombardment

To isolate the role of ion beam bombardment in CNT growth, we investigated the evolution of catalysts on pristine and ion beam-damaged substrates without an alumina layer. Figure 2.6 shows histograms of particle size distributions (PSDs) formed on Pristine-0 and Damaged-0 after the CCVD process. From histograms obtained from analysis of SEM images of SS surfaces using ImageJ [43], it is apparent that PSDs of catalyst supported on Prisine-0 and Damaged-0 follow a bimodal distribution. The first model peak of particles on Pristine-0 and Damaged-0 is centered ~30.58 nm and ~28.80 nm, respectively. Particles in the first mode are believed to be formed during the annealing step (H_2, 750 °C, 10 min) and may have experienced ripening during the growth step (C_2H_4, H_2, Ar, 750 °C, 10 min). The position of the second modal peak of Pristine-0 and Damaged-0 indicates the presence of large particles with average diameters (or lateral distances) of ~216.76 nm and ~163.00 nm, respectively. Particles in the

second mode appear to be mostly composed of Fe film still wetted to the substrate surface, and are unsuitable for CNT growth.

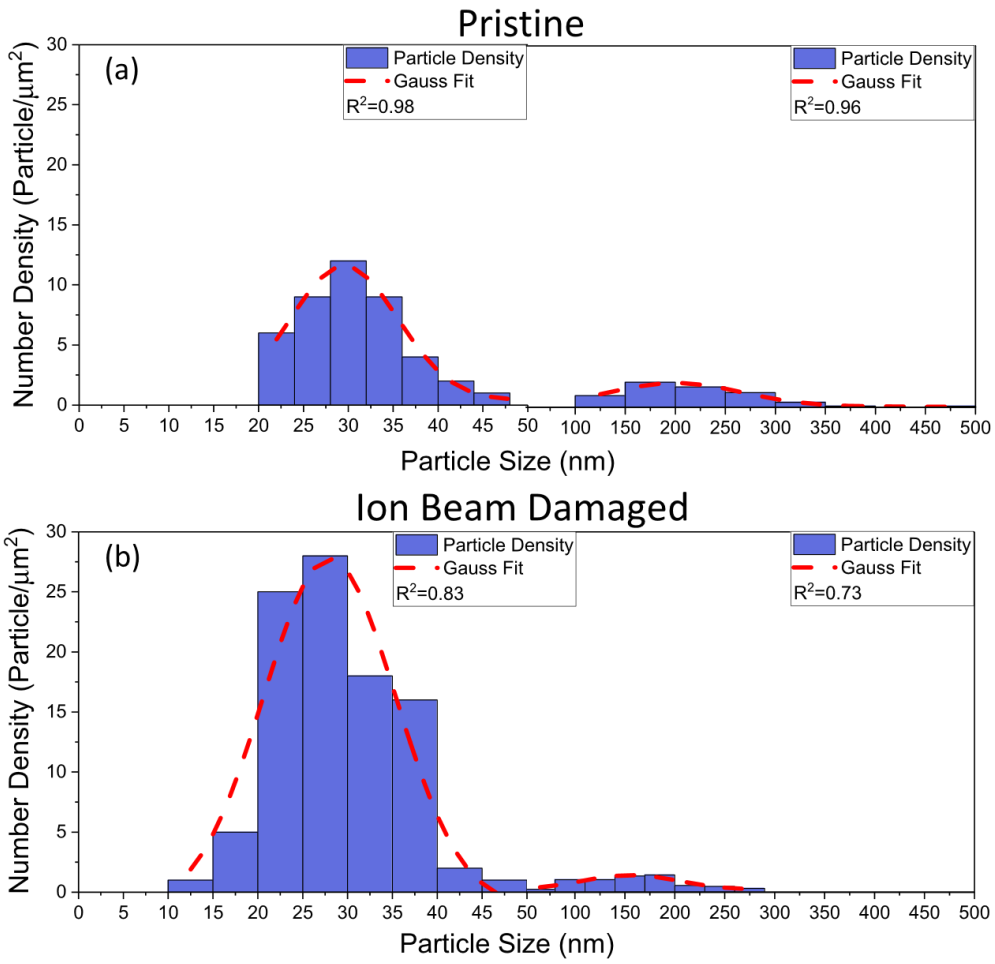

Figure 2.6. Catalyst evolution on Pristine-0 and Damaged-0. Particle size distributions (PSDs) of catalyst particles formed after CVD growth on Pristine-0 (a) and Damaged-0 (b).

Although the number density of catalyst particles on Pristine-0 and Damaged-0 for the second mode is somewhat the same, there is a stark difference in the particle number density formed on Pristine-0 and Damaged-0 for the first mode. The number density of catalysts on Pristine-0 is 43 particle/μm^2 while that on Damaged-0 is 96 particle/μm^2. Some of the catalyst nanoparticles imaged in Figure 2.2a (pristine SS) are wetted to the surface and not spherical in shape, indicating the Fe film was not fully de-wetted during the annealing process, while Figure

2.2e (damaged SS) shows particles that are spherical in shape. Like alumina, ion beam bombardment plays an important role in enhancing particle formation in the size range suitable for CNT growth during annealing of the deposited Fe film. However, the presence of a thin Al_xO_y barrier layer is still required for CNT growth. Ion beam damage of SS increases the number density of particles less than 50 nm by a factor of 2. The decrease in the average particle size formed on damaged SS demonstrates that ion beam bombardment plays a significant role in not only catalyst dewetting, but also catalyst stability. Based on our previous study,[30] we attribute the improved properties of ion beam-damaged SS to the increased porosity on the surface of SS prior to Al_xO_y deposition. We conclude from our results that ion beam bombardment of SS favors formation and stability of catalyst particles during CCVD, which contributes to CNT growth efficiency.

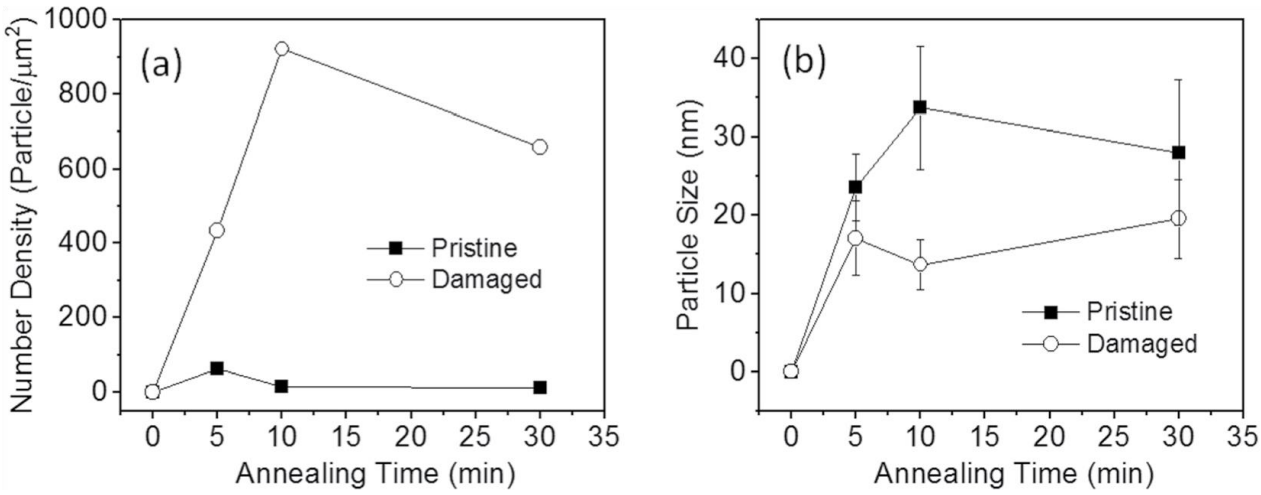

Figure 2.7. Catalyst evolution on Pristine-5 and Damaged-5 during annealing. (a) Plots of number density of particles as a function of annealing time. (b) Plots of catalyst particle size as a function of annealing time. The data were adapted from SEM images presented in Appendix A.

2.3.5 Catalyst evolution on pristine and ion beam-damaged SS with an Al_xO_y barrier layer

The combined effect of ion beam bombardment of SS and an Al_xO_y barrier layer on the evolution of deposited Fe catalyst film was studied. To isolate the Ostwald ripening event, an annealing study was carried out on Pristine-5- and Damaged-5-supported catalysts in the absence of the feedstock (250 sccm Ar/250 sccm H_2). Figure 2.7 shows plots of the density of particles and average catalyst size as functions of annealing time. The data were derived from SEM data presented in the Appendix A. Number density of particles on Damaged-5 after annealing for the different times is significantly higher than particles on Pristine-5 (Figure 2.7a). In fact, after annealing for 5, 10, and 30 min, the number density of particles on Pristine-5 was 62, 16, and 13 particle/μm^2, respectively. In contrast, number density of particles on Damaged-5 after annealing for 5, 10, and 30 min was 435, 922, and 659, respectively. Note that while number density of particles on Pristine-5 decreases with annealing time, catalysts supported on Damaged-5 exhibit dramatic increases in number density, with an increase of more than 50% between 5 and 10 min. In addition, the catalyst particles on Damaged-5 have a lower average size in comparison to Pristine-5 (Figure 2.7b). After annealing for 5, 10, and 30 min, average size of particles on Pristine-5 was 23.6, 33.8, and 28.1 nm, while the average size of particles on Damaged-5 was 17.1, 13.7, and 19.6 nm, respectively. Thus, ion beam bombardment of SS in combination with an Al_xO_y barrier layer dramatically improves particle formation (or dewetting), and has the ability to suppress Ostwald ripening or enhance catalyst stability. Therefore, the improved growth behavior of Damaged-5, Damaged-10, and Damaged-20 is due to the synergistic effect of ion beam bombardment and thin Al_xO_y barrier layer. Creation of surface porosity and a defective surface by ion beam bombardment, and a basic surface by Al_xO_y deposition, may enhance the

stability of catalyst particles on the surface and limit their mobility throughout the annealing and growth processes.

2.4 Discussion

We emphasize that since Damaged-0 does not support CNT growth (Figure 2.2), this suggests that modification via ion beam bombardment alone under the conditions used in this study is incapable of transforming SS from an "inactive" to an "active" substrate. In the case of sapphire[28, 30], it was possible to achieve complete transformation after ion beam damage alone, because the process created both surface porosity and increased basicity. Cationic vacancies were created by ion beam damage, which was evidenced by an increased O/Al ratio, accounted for increased basicity. Ion beam bombardment is not expected to change the surface energy of the basic component of SS due to its composition, thus for complete transformation of SS, an alumina layer that provides a basic environment is required in combination with ion beam bombardment. However, the improved CNT growth efficiency on ion beam-damaged SS with the same Al_xO_y thickness, as evidenced by improved CNT areal density, growth rate, and surface coverage of CNTs, demonstrates the critical role of ion beam bombardment in the transformation of "inactive" substrates to "active" substrates.

To rationalize the synergistic effect of thin Al_xO_y barrier layer and ion beam bombardment, we took a closer look at the effect of each factor on CNT catalysis. Fe catalyst has a strong interaction with surface oxygen atoms of Al_xO_y and forms Fe^{2+} and Fe^{3+} interface states on Al_xO_y, which is believed to enhance catalyst stability and inhibit severe sintering of the catalyst. [41] In addition, our previous study revealed a complex interdependence between Ostwald ripening rates, subsurface diffusion rates, and porosity; and that catalytic activity of Fe is maximized on Al_xO_y support because of the high porosity of Al_xO_y, mild subsurface diffusion

of Fe, and presence of surface hydroxyl groups [29, 32, 40, 44]. Al_xO_y-Fe interactions favor increased particle formation and CNT nucleation density as well as CNT growth over a broad range of CCVD conditions. In the case of ion beam bombardment of substrates, prior studies indicate the process induces atomic vacancies and interstitials thereby introducing porosity and surface roughness [28, 34, 35]. These changes in the substrate caused by ion beam bombardment has been reported to improve adhesion between ion beam-damaged substrates and deposited films [34]. We, therefore, explain the CNT growth enhancement after SS modification as follows: The increased surface roughness and porosity caused by ion beam bombardment enhances intermixing between SS and alumina film, resulting in improved coating of the thin barrier layer. Consequently, a higher fraction of Fe catalyst interacts directly with Al_xO_y in Damaged-5, Damaged-10, and Damaged-20, and benefits from the positive role of Al_xO_y discussed above in comparison to their pristine counterparts. As shown in Figure 2.6, even particles that are in direct contact with ion beam-damaged surface in the absence of alumina exhibit higher stability than pristine substrates due to the presence of a porous upper layer. The reduced barrier layer thickness required for CNT growth may be due to the contribution of the upper porous layer created by ion beam damage, which creates a thicker alumina-like layer (in terms of surface diffusion properties) required for favorable catalyst-support interactions.

2.5 Conclusions

In summary, we have demonstrated the impact of surface modification (changes in surface structure and Lewis basicity) of 316 SS, a known inactive metallic substrate for CNT growth, on CNT growth behavior from deposited Fe catalyst. Surface modification of SS via ion beam bombardment decreases the barrier-layer thickness required for unaligned CNT growth to ~5 nm and dense CNT carpet growth to 20 nm. An Fe catalyst supported on damaged SS with an

Al_xO_y barrier layer shows improved activity, and the resulting CNT arrays have higher quality and density in comparison to a pristine substrate (without ion beam damage) with an Al_xO_y barrier layer. While ion beam damage alone improves particle formation (or dewetting) and catalyst stability, the combined effect of ion beam bombardment and an Al_xO_y barrier layer is significantly higher. This new approach can potentially benefit applications that require high electron transport between CNTs and metallic substrates.

2.6 References

[1] W. Wang, P.N. Kumta, Nanostructured hybrid silicon/carbon nanotube heterostructures: reversible high-capacity lithium-ion anodes, *ACS Nano*, 4 (2010) 2233-2241.

[2] C.L. Pint, N.W. Nicholas, S. Xu, Z. Sun, J.M. Tour, H.K. Schmidt, R.G. Gordon, R.H. Hauge, Three dimensional solid-state supercapacitors from aligned single-walled carbon nanotube array templates, *Carbon*, 49 (2011) 4890-4897.

[3] H. Chen, M. Chen, J. Di, G. Xu, H. Li, Q. Li, Architecting three-dimensional networks in carbon nanotube buckypapers for thermal interface materials, *The Journal of Physical Chemistry C*, 116 (2012) 3903-3909.

[4] B.A. Cola, J. Xu, C. Cheng, X. Xu, T.S. Fisher, H. Hu, Photoacoustic characterization of carbon nanotube array thermal interfaces, *Journal of Applied Physics*, 101 (2007) 054313.

[5] E. Llobet, Gas sensors using carbon nanomaterials: A review, *Sensors and Actuators B: Chemical*, 179 (2013) 32-45.

[6] K. Saetia, J.M. Schnorr, M.M. Mannarino, S.Y. Kim, G.C. Rutledge, T.M. Swager, P.T. Hammond, Spray‐Layer‐by‐Layer Carbon Nanotube/Electrospun Fiber Electrodes for Flexible Chemiresistive Sensor Applications, *Advanced Functional Materials*, 24 (2014) 492-502.

[7] Y. Wang, Z. Luo, B. Li, P.S. Ho, Z. Yao, L. Shi, E.N. Bryan, R.J. Nemanich, Comparison study of catalyst nanoparticle formation and carbon nanotube growth: support effect, *Journal of Applied Physics*, 101 (2007) 124310.

[8] J. Dijon, A. Fournier, P.D. Szkutnik, H. Okuno, C. Jayet, M. Fayolle, Carbon nanotubes for interconnects in future integrated circuits: The challenge of the density, *Diamond and Related Materials*, 19 (2010) 382-388.

[9] C. Zhang, F. Yan, C. Allen, B. Bayer, S. Hofmann, B. Hickey, D. Cott, G. Zhong, J. Robertson, Growth of vertically-aligned carbon nanotube forests on conductive cobalt disilicide support, *Journal of Applied Physics*, 108 (2010) 024311.

[10] S. Esconjauregui, B. Bayer, M. Fouquet, C. Wirth, F. Yan, R. Xie, C. Ducati, C. Baehtz, C. Castellarin-Cudia, S. Bhardwaj, Use of plasma treatment to grow carbon nanotube forests on TiN substrate, *Journal of Applied Physics*, 109 (2011) 114312.

[11] C.-M. Seah, S.-P. Chai, A.R. Mohamed, Synthesis of aligned carbon nanotubes, *Carbon*, 49 (2011) 4613-4635.

[12] J.J. Nguyen, S. Turano, W.J. Ready, The synthesis of carbon nanotubes grown on metal substrates: A review, *Nanoscience and Nanotechnology Letters*, 4 (2012) 1123-1131.

[13] R. Kavian, A. Vicenzo, M. Bestetti, Growth of carbon nanotubes on aluminium foil for supercapacitors electrodes, *Journal of Materials Science*, 46 (2011) 1487-1493.

[14] I. Lahiri, S.-W. Oh, J.Y. Hwang, S. Cho, Y.-K. Sun, R. Banerjee, W. Choi, High capacity and excellent stability of lithium ion battery anode using interface-controlled binder-free multiwall carbon nanotubes grown on copper, *ACS Nano*, 4 (2010) 3440-3446.

[15] L. Gao, A. Peng, Z.Y. Wang, H. Zhang, Z. Shi, Z. Gu, G. Cao, B. Ding, Growth of aligned carbon nanotube arrays on metallic substrate and its application to supercapacitors, *Solid State Communications*, 146 (2008) 380-383.

[16] C.E. Baddour, F. Fadlallah, D. Nasuhoglu, R. Mitra, L. Vandsburger, J.-L. Meunier, A simple thermal CVD method for carbon nanotube synthesis on stainless steel 304 without the addition of an external catalyst, *Carbon*, 47 (2009) 313-318.

[17] T. Hiraoka, T. Yamada, K. Hata, D.N. Futaba, H. Kurachi, S. Uemura, M. Yumura, S. Iijima, Synthesis of single-and double-walled carbon nanotube forests on conducting metal foils,

Journal of the American Chemical Society, 128 (2006) 13338-13339.

[18] M. Hashempour, A. Vicenzo, F. Zhao, M. Bestetti, Direct growth of MWCNTs on 316 stainless steel by chemical vapor deposition: Effect of surface nano-features on CNT growth and structure, *Carbon*, 63 (2013) 330-347.

[19] C. Masarapu, B. Wei, Direct growth of aligned multiwalled carbon nanotubes on treated stainless steel substrates, *Langmuir*, 23 (2007) 9046-9049.

[20] E.-C. Shin, G.-H. Jeong, Highly efficient carbon nanotube growth on plasma pretreated stainless steel substrates, *Thin Solid Films*, 521 (2012) 102-106.

[21] X. Lepro, M.D. Lima, R.H. Baughman, Spinnable carbon nanotube forests grown on thin, flexible metallic substrates, *Carbon*, 48 (2010) 3621-3627.

[22] R.L. Vander Wal, L.J. Hall, Carbon nanotube synthesis upon stainless steel meshes, *Carbon*, 41 (2003) 659-672.

[23] S.W. Pattinson, B. Viswanath, D.N. Zakharov, J. Li, E.A. Stach, A.J. Hart, Mechanism and enhanced yield of carbon nanotube growth on stainless steel by oxygen-induced surface reconstruction, *Chemistry of Materials*, 27 (2015) 932-937.

[24] C. Zhuo, X. Wang, W. Nowak, Y.A. Levendis, Oxidative heat treatment of 316L stainless steel for effective catalytic growth of carbon nanotubes, *Applied Surface Science*, 313 (2014) 227-236.

[25] N.S. Nejad, M. Larijani, M. Ghoranneviss, P. Balashabadi, A. Shokouhy, Direct growth of carbon nanotubes on Ar ion bombarded AISI 304 stainless steel substrates, *Surface and Coatings Technology*, 203 (2009) 2510-2513.

[26] D.Q. Duy, H.S. Kim, D.M. Yoon, K.J. Lee, J.W. Ha, Y.G. Hwang, C.H. Lee, B.T. Cong, Growth of carbon nanotubes on stainless steel substrates by DC-PECVD, *Applied Surface*

Science, 256 (2009) 1065-1068.

[27] L. Camilli, M. Scarselli, S. Del Gobbo, P. Castrucci, F. Nanni, E. Gautron, S. Lefrant, M. De Crescenzi, The synthesis and characterization of carbon nanotubes grown by chemical vapor deposition using a stainless steel catalyst, *Carbon*, 49 (2011) 3307-3315.

[28] P.B. Amama, A.E. Islam, S.M. Saber, D.R. Huffman, B. Maruyama, Understanding properties of engineered catalyst supports using contact angle measurements and X-Ray reflectivity, *Nanoscale*, 8 (2016) 2927-2936.

[29] P.B. Amama, C.L. Pint, S.M. Kim, L. McJilton, K.G. Eyink, E.A. Stach, R.H. Hauge, B. Maruyama, Influence of alumina type on the evolution and activity of alumina-supported Fe catalysts in single-walled carbon nanotube carpet growth, *ACS Nano*, 4 (2010) 895-904.

[30] A. Islam, P. Nikolaev, P. Amama, S. Saber, D. Zakharov, D. Huffman, M. Erford, G. Sargent, S. Semiatin, E. Stach, Engineering the activity and lifetime of heterogeneous catalysts for carbon nanotube growth via substrate ion beam bombardment, *Nano Letters*, 14 (2014) 4997-5003.

[31] A. Magrez, R. Smajda, J.W. Seo, E. Horvath, P.R. Ribič, J.C. Andresen, D. Acquaviva, A. Olariu, G. Laurenczy, L.s. Forró, Striking influence of the catalyst support and its acid–base properties: new Insight into the growth mechanism of carbon nanotubes, *ACS Nano*, 5 (2011) 3428-3437.

[32] P.B. Amama, S.A. Putnam, A.R. Barron, B. Maruyama, Wetting behavior and activity of catalyst supports in carbon nanotube carpet growth, *Nanoscale*, 5 (2013) 2642-2646.

[33] G. Zhong, J. Yang, H. Sugime, R. Rao, J. Zhao, D. Liu, A. Harutyunyan, J. Robertson, Growth of high quality, high density single-walled carbon nanotube forests on copper foils, *Carbon*, 98 (2016) 624-632.

[34] D. Manova, J.W. Gerlach, S. Mändl, Thin film deposition using energetic ions, *Materials*, 3 (2010) 4109-4141.

[35] Z.W. Kowalski, J. Wilk, J. Martan, Surface morphology of steel and titanium induced by ion beam bombardment–Comprehensive analysis, *Vacuum*, 83 (2009) S208-S213.

[36] R. Droppa Jr, H. Pinto, J. Garcia, E. Ochoa, M. Morales, S. Cucatti, F. Alvarez, Influence of ion-beam bombardment on the physical properties of 100Cr6 steel, *Materials Chemistry and Physics*, 147 (2014) 105-112.

[37] S. Cucatti, E. Ochoa, M. Morales, R. Droppa Jr, J. Garcia, H. Pinto, L. Zagonel, D. Wisnivesky, C. Figueroa, F. Alvarez, Effect of bombarding steel with Xe+ ions on the surface nanostructure and on pulsed plasma nitriding process, *Materials Chemistry and Physics*, 149 (2015) 261-269.

[38] R.J. Nemanich, S. Solin, First-and second-order Raman scattering from finite-size crystals of graphite, *Physical Review B*, 20 (1979) 392.

[39] W. Li, H. Zhang, C. Wang, Y. Zhang, L. Xu, K. Zhu, S. Xie, Raman characterization of aligned carbon nanotubes produced by thermal decomposition of hydrocarbon vapor, *Applied Physics Letters*, 70 (1997) 2684-2686.

[40] P.B. Amama, C.L. Pint, L. McJilton, S.M. Kim, E.A. Stach, P.T. Murray, R.H. Hauge, B. Maruyama, Role of water in super growth of single-walled carbon nanotube carpets, *Nano Letters*, 9 (2008) 44-49.

[41] C. Mattevi, C.T. Wirth, S. Hofmann, R. Blume, M. Cantoro, C. Ducati, C. Cepek, A. Knop-Gericke, S. Milne, C. Castellarin-Cudia, In-situ X-ray photoelectron spectroscopy study of catalyst− support interactions and growth of carbon nanotube forests, *The Journal of Physical Chemistry C*, 112 (2008) 12207-12213.

[42] R. Rao, N. Pierce, A.R. Harutyunyan, Enhancement of Vertically Aligned Carbon Nanotube Growth Kinetics and Doubling of the Height by Graphene Interface, *The Journal of Physical Chemistry C*, 118 (2014) 22243-22248.

[43] R.W. ImageJ, US National Institute of Health, Bethesda, Maryland.

[44] P.B. Amama, C.L. Pint, F. Mirri, M. Pasquali, R.H. Hauge, B. Maruyama, Catalyst–support interactions and their influence in water-assisted carbon nanotube carpet growth, *Carbon*, 50 (2012) 2396-2406.

Chapter 3 - Carbon Nanotube Carpet Growth from Catalyst Supported on Nontraditional Substrates

3.1 Introduction

There is increasing interest in achieving efficient growth of vertically aligned high-quality carbon nanotube (CNT) arrays (or CNT carpets) due to their suitability in a wide range of applications such as energy storage [1, 2], thermally conductive materials [3, 4], catalysis [5, 6], and sensing devices [7, 8]. The preferred method for CNT synthesis is chemical vapor deposition (CVD) due to its simplicity and potential of achieving mass production of CNTs with tailored properties [9, 10]. Typically, catalytic CVD process involves CNT carpet growth from transition metal (Fe, Co or Ni) catalyst particles supported on an alumina or silica thin film [11-13]. However, some of the aforementioned applications usually require CNT arrays to be grown directly on conductive, temperature-sensitive or easily removable substrates. Studies [12, 14, 15] have shown that using the same catalyst with different substrates result in different CNT growth behaviors. It is unsurprising that CNT growth behavior is highly sensitive to the properties of the catalyst substrate given that wetting of the catalyst film (during deposition) and dewetting (during annealing and prior to CNT growth) are largely controlled by surface energies of substrates. It is therefore expected that different physicochemical properties of substrates will induce different metal-support interactions and possibly form different catalyst morphologies or expose different facets of catalyst that may impact CNT properties.

Properties of substrates that profoundly impact CNT growth include chemical composition, crystal phase, porosity, surface energy, and surface basicity [12, 14-19]. High substrate porosity [12, 20], favorable metal-support interactions [16, 17] and high Lewis basicity of the substrate [19, 21] result in improved CNT growth efficiency. Usually, high surface energy

of the substrate will hamper the transformation of the catalyst film to nanoparticles during the annealing process [14, 22]. On the other hand, dewetted nanoparticles on substrates with low surface energies are prone to Ostwald ripening and sintering. Catalyst design strategies for efficient CNT carpet growth should lead to optimum conditions that ensure dewetting of the deposited film to form nanoparticles and subsequent stability of the nanoparticles over long durations at high temperatures. It has been reported that sapphire substrates with different crystallographic phases have different CNT growth rate [23]. Moreover, Ishigami et al. [24] also reported that different Al_2O_3 crystallographic phases influence the diameter and chirality of the grown single-walled CNTs (SWCNTs). In general, CNT growth from catalyst nanoparticles supported on a variety of substrates such as MgO [25, 26], TiO_2 [27, 28], ZrO_2 [29], SiO_2 [30, 31] and zeolite [32] have largely failed to mimic the high growth efficiency observed on amorphous alumina films. To broaden the substrates that support growth of CNT arrays, a variety of strategies were implemented including water-assisted CNT growth [33], acid etching [34, 35], and plasma etching [36]. Recently, ion beam bombardment was used for substrate modification prior to catalyst deposition, enabling the transformation of "inactive" substrates such as c-cut sapphire and stainless steel to "active" substrates for CNT growth [37, 38]. The transformation is attributed to the creation of surface porosity and Lewis basicity after modification.

In this study, we focus on a family of substrates that have shown promising results as a support for Fe catalyst in hydrocarbon reactions. The substrates also provide a framework for testing our hypothesis: CNT carpet properties can be controlled by adjusting substrate properties (composition, phase, basicity, and surface properties) and type of feedstock. MgO is of interest as a substrate because of its anti-sintering and strong catalyst-substrate interactions in Fe-based

[39, 40] and Co-based [41, 42] catalysts. Fe is able to dissolve in MgO during wet chemistry synthesis and at higher temperatures precipitate from MgO yielding small particles in a hydrogen environment [43]. A new refractory material that has attracted significant interest in a variety of applications is $MgAl_2O_4$ due to its interesting properties such as high melting point, low dielectric constant, high thermal resistance, high chemical inertness, good mechanical properties, and outstanding optical properties [44, 45]. Its use as a support in catalysis is quite recent and has been inspired by excellent results in steam reforming [46], dehydrogenation reactions [45], and partial oxidation of methane [47]. $MgAl_2O_4$ spinel supports high dispersion of nanosized metal nanoparticles and has the tendency to inhibit formation of carbon impurities and enhance favorable interactions with the metallic phase that inhibits sintering [45-47]. MgO and $MgAl_2O_4$ consist of large number of edges and corners, step edges and step corners that create basic sites with different strength depending on the functional group (surface hydroxyl groups, low coordinate O^{2-} sites) [48]. The surface structure of complex oxides plays an important role in film growth such as CNT growth [49]. $MgAl_2O_4$ with different crystalline phases is of great interest in CNT synthesis because of current understanding on the high sensitivity of catalytic activity and CNT growth behavior to crystalline phase of supporting layers. The selected substrates, MgO and $MgAl_2O_4$ family, provide a model system to probe the effect of physicochemical properties of substrates on CNT carpet growth from Fe catalyst.

In this study, CNT growth behavior is systematically investigated on the following pristine and ion beam-bombarded substrates: $MgAl_2O_4$ (100), $MgAl_2O_4$ (110), $MgAl_2O_4$ (111), and MgO (100). Interrelationships between physicochemical properties of different catalyst supports (before and after ion beam bombardment) and CNT growth behavior were established for the first time. The study also investigates the complex interplay between substrate properties

and type of feedstock used for growth, focusing on two feedstocks: ethylene (the conventional feedstock) and our newly developed feedstock, Fischer-Tropsch synthesis gaseous products (FTS-GP).

3.2 Experimental

3.2.1 Catalyst Preparation

Four pristine and modified substrates were used as catalyst supports for CNT growth via CVD: $MgAl_2O_4$ (100), $MgAl_2O_4$ (110), $MgAl_2O_4$ (111), and MgO (100). The substrates were modified by ion beam bombardment using an ion beam sputter deposition and etching system (IBS/e) from South Bay Technology Inc. Substrates were placed directly opposite the Ar ion source (spot size ~3 mm) with adjustments made to ensure the beam line is perpendicular to the substrate. Ion beam damage of the substrate was conducted for 10 min at an acceleration voltage of 6 kV and a beam current of 3.5 mA. The total ion dose was calculated to be 1.46×10^{20} cm^{-2}. In calculating the ion dose, the ion dose rate was determined by assuming the number of ions injected per unit area per second (N) and the duration of ion exposure (t) were equally received by the substrate. N was calculated using the following equation:

$$N = \frac{I}{q \cdot A}\ cm^{-2}s^{-1},$$

where I is the beam current in amperes, A is the ion beam spot area in square centimeters, and q is the charge of an electron (1.6×10^{-19} Coulomb). Thereafter, a Fe catalyst film with a nominal thickness of 2 nm was deposited on the pristine and ion beam-damaged substrates in the IBS/e without exposure to air. This catalyst thickness was expected to produce small-diameter multi-walled CNT carpets.

3.2.2 CNT Growth

Growth of CNT carpets was carried out at atmospheric pressure using an EasyTube 101 CVD system (CVD Equipment Corporation) equipped with a LabView-based process control software, a static mixer for optimum gas mixing, and a precise temperature control system. CVD growth was conducted using either ethylene or FTS-GP (Fischer-Tropsch synthesis gaseous product) as a carbon source under conditions optimized for each feedstock. In a typical growth run, the catalyst sample was heated to 750 °C at a rate of 50 °C/min in flowing 1000 standard cubic centimeters per minute (sccm) Ar. For growth with ethylene as a feedstock, catalyst prereduction at growth temperature (750°C) was carried out for 10 min with copious amount of H_2 (250 sccm H_2 and 500 sccm Ar). Thereafter, CNT growth was initiated by switching to a gas mixture of 100 sccm C_2H_4, 250 sccm H_2, and 500 sccm Ar. At the end of the growth, the samples were rapidly cooled in H_2, followed by slow cooling to room temperature in 700 sccm Ar. For growth using FTS-GP as a feedstock, the catalyst prereduction was conducted by flowing 250 sccm H_2 and 250 sccm Ar for various time. Thereafter, CNT growth was initiated by switching to the growth gas mixture containing 100 sccm FTS-GP and 1000 sccm Ar. At the end of growth, the samples were cooled using similar conditions described above for growth with ethylene.

3.2.3 Characterization

The morphology of the growth products and growth behavior of the different catalyst substrates were characterized with a Hitachi S5200 field-emission scanning electron microscope (SEM) operated at 5 kV. A Nikon Eclipse LV100 optical microscope was also used to measure the heights of tall CNT carpets. Raman spectra of growth products were collected at multiple

spots from the samples using a Renishaw inVia Raman microscope equipped with a 532-nm laser as the excitation source. The surface properties of pristine and ion beam-damaged substrates were characterized using X-Ray reflectivity (XRR). XRR measurements were conducted on a Rigaku-Smartlab X-ray diffractometer equipped with a Cu Kα (λ = 0.154 nm) radiation source using a slit collimation in air.

3.3 Results

Figure 3.1 shows CVD growth behavior of Fe catalyst supported on pristine and ion beam-bombarded substrates [MgO (100), $MgAl_2O_4$ (100), $MgAl_2O_4$ (110), $MgAl_2O_4$ (111)] with a conventional precursor (C_2H_4) and FTS-GP. The morphologies of the resulting products formed on the substrates were obtained after exposure to CVD conditions optimized for each feedstock. Figures 3.1a and b show SEM images of CNTs formed on pristine substrates after 10 min using C_2H_4 and FTS-GP as feedstock, respectively. For CNTs grown with C_2H_4, only MgO (100) substrate supports carpet (or vertically aligned) growth while growth with FTS-GP yielded carpets on $MgAl_2O_4$ (111) and MgO (100) substrates. It is apparent from the results that catalysts supported on pristine MgO (100) exhibits the highest growth efficiency with high CNT nucleation density that support dense growth of CNTs with both C_2H_4 and FTS-GP feedstocks. For the same growth duration of 10 min using MgO-supported catalyst, the carpet heights were ~400 µm and ~300 µm using FTS-GP and C_2H_4 respectively. We hypothesize, based on this preliminary evidence, that initial growth rate with FTS-GP is higher than C_2H_4 .

Figures 3.1c and d show SEM images of CNT carpets formed on ion beam-bombarded substrates after CVD growth with C_2H_4 and FTS-GP, respectively. Thick CNT carpet coverage was observed on all ion beam-damaged substrates, with the substrates exposed to FTS-GP

forming CNT carpets that are generally taller than those formed with C_2H_4. The positive impact of ion beam bombardment is apparent in all the different phases of $MgAl_2O_4$ spinel after C_2H_4 CVD and in $MgAl_2O_4$ (100) and $MgAl_2O_4$ (110) after FTS-GP CVD. The dramatic improvement in CNT growth efficiency of catalysts on substrates with poor activity after ion beam bombardment further confirms the efficacy of this modification process in effectively transforming a poor catalyst supporting layer to an active layer that induces higher CNT nucleation density and growth efficiency. However, from the SEM images in Figure 3.1, ion beam bombardment of MgO (100) substrate does not seem to have a significant effect on the CNT carpet height, as the final carpet heights attained after 10 min with C_2H_4 and FTS-GP remained roughly the same after substrate modification. Fe catalyst supported on MgO (100) substrates (pristine or ion beam-damaged) show the highest growth efficiency when C_2H_4 or FTS-GP is used as a feedstock. According to prior studies, the high surface basicity of MgO (100) and favorable Fe-MgO interactions contribute to the improved CNT growth observed on MgO [19, 50, 51]. A related study by Xiong et al. [52] revealed a strong dependence of carpet height on the orientation of MgO, with MgO (110)-supported Fe catalyst producing CNTs with the longest length while CNTs formed on MgO (100) and MgO (111) were 20% and 55% shorter, possibly due to the different interaction energies of Fe with the different planes that result in different nucleation behaviors. Our results demonstrate the use of FTS-GP as a feedstock result in decent CNT carpet growth on MgO (100) indicating that FTS-GP seems to decrease the sensitivity of catalysts to the crystalline phase of the support. The growth on MgO (100) via FTS-GP CVD equals or outperforms prior works [52, 53].

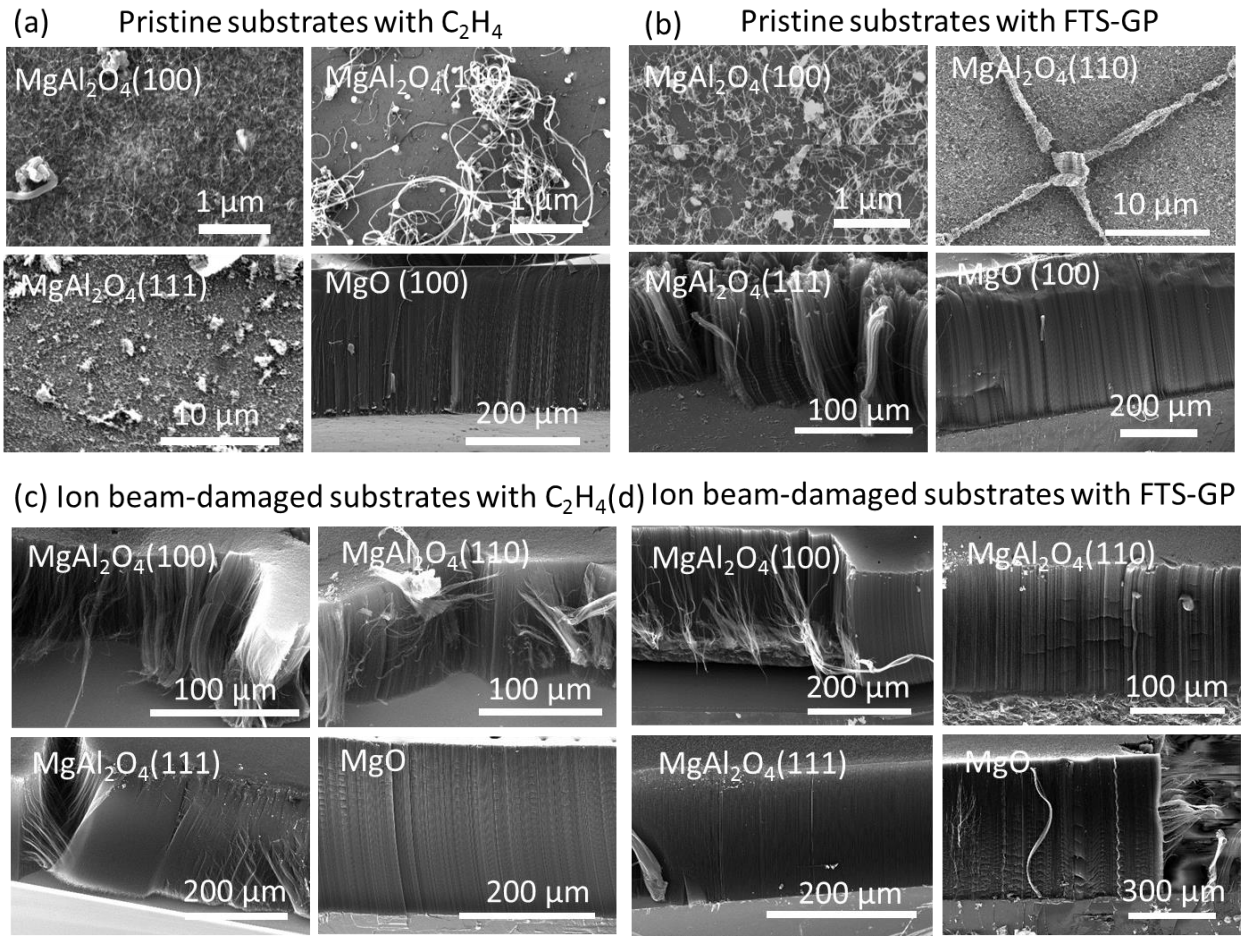

Figure 3.1 SEM characterization of CNTs grown from Fe catalyst supported on $MgAl_2O_4$ (100), $MgAl_2O_4$ (110), $MgAl_2O_4$ (111) and MgO (100) supporting substrates after 10 min. Images of CNTs formed on pristine substrates using C_2H_4 as a feedstock (a) and FTS-GP as a feedstock (b). Images of CNTs formed on ion beam-bombarded substrates using C_2H_4 as a feedstock (c) and FTS-GP as a feedstock (d).

The quality of CNTs formed on the different substrates with either C_2H_4 or FTS-GP CVD as a feedstock was probed by Raman spectroscopy. The Raman spectra of products formed on the surfaces of pristine and ion beam-damaged substrates are shown in Figure 3.2. The characteristic modes of CNTs are apparent in the spectra: tangential stretch mode (G-band) at ~1593 cm^{-1} that represents the highly oriented lattice structure of graphitic carbon, and disorder-induced mode (D-band) around 1345 cm^{-1} that is indicative of the presence of defects or

amorphous carbon. The ratio of G-band to D-band intensities (I_G/I_D) has been used as an index to evaluate the quality of the CNTs, and the I_G/I_D value for each sample is shown above the spectrum in Figure 3.2. In combination with SEM data (Figure 3.1), the following observations can be gleaned from the Raman spectra of CNTs grown from catalyst on pristine substrates with C_2H_4 and FTS-GP shown in Figures 3.2a and b, respectively. CNTs grown on $MgAl_2O_4$ (100) substrate using C_2H_4 exhibited the highest I_G/I_D ratio, albeit with poor nucleation density and overall growth as revealed by SEM image in Figure 3.1a. However, using FTS-GP as a feedstock, products formed on $MgAl_2O_4$ (100) substrate not only shows a very high I_G/I_D ratio, but also yield denser CNT carpets than those obtained with C_2H_4, indicating $MgAl_2O_4$ (100) supports high-quality CNT growth. Raman spectra of products formed on ion-beam bombarded substrates are shown in Figure 3.2c and d. Ion beam bombardment appears to have a negative effect on the quality of CNTs formed on $MgAl_2O_4$ (100) substrate, evidenced by the decrease in I_G/I_D ratio of CNTs formed on the substrate after ion beam damage for growth especially with FTS-GP. In contrast, the I_G/I_D ratios of CNTs formed on the other damaged substrates does not appear to change significantly except for MgO (100) where CNT carpet quality improves after FTS-GP CVD, but decreases after C_2H_4 CVD. In general, the CNTs grown using FTS-GP had higher I_G/I_D ratios for all supported catalyst samples except for pristine MgO (100) and ion beam-damaged $MgAl_2O_4$ substrates. The different behavior of three different $MgAl_2O_4$ substrates could be due to the surface atom stoichiometric change caused by ion beam bombardment that affects the catalyst structure during nanoparticle formation (annealing) and catalyst stability during growth.

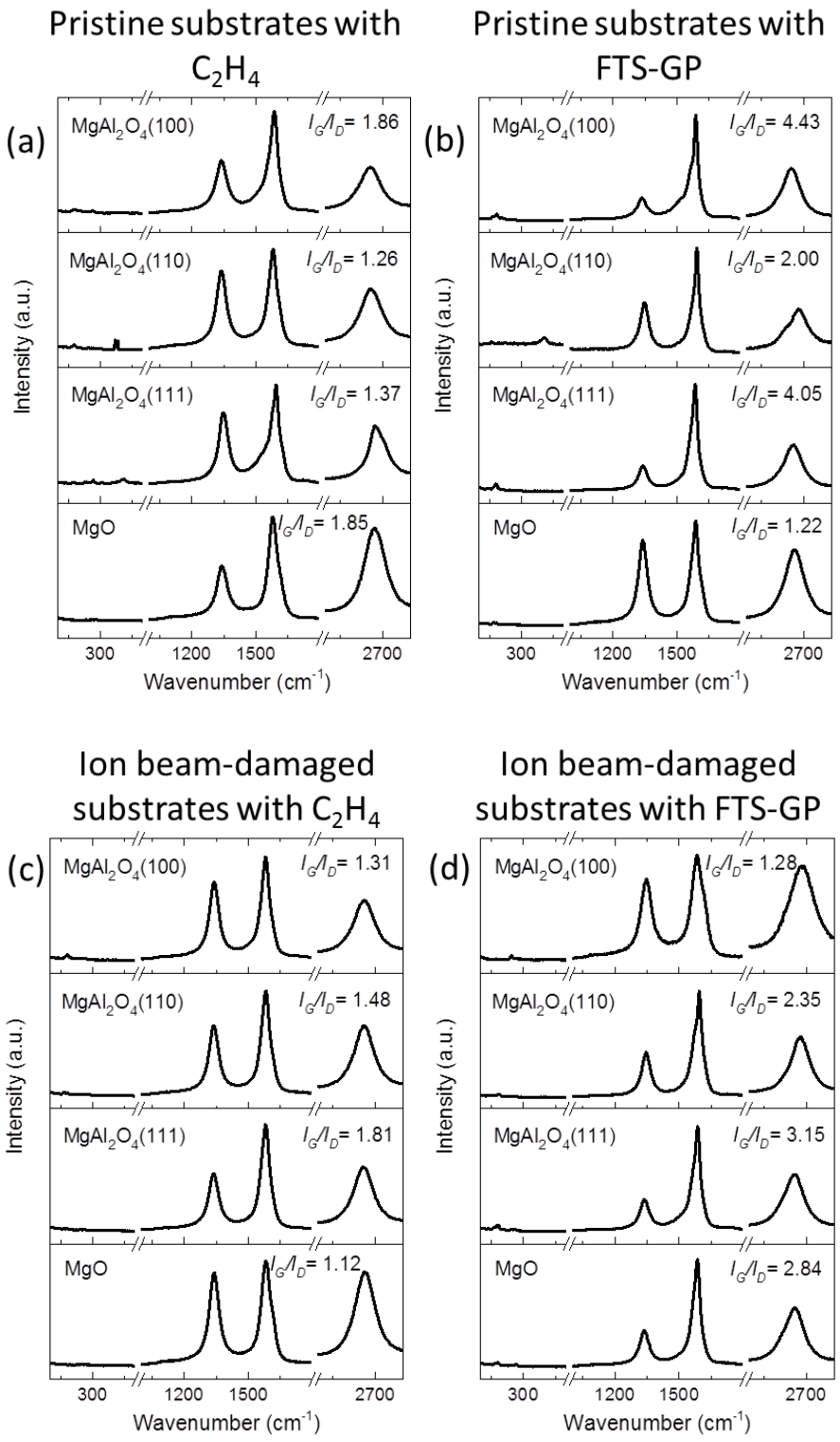

Figure 3.2 Raman spectroscopic characterization of CNTs grown from Fe catalyst supported on $MgAl_2O_4$ (100), $MgAl_2O_4$ (110), $MgAl_2O_4$ (111) and MgO (100) substrates after 10 min. Raman spectra of CNTs formed on pristine substrate using C_2H_4 precursor (a) and FTS-GP precursor (b). Raman spectra of CNTs formed on ion beam-damaged substrate using C_2H_4 precursor (c) and FTS-GP precursor (d).

Having established an understanding of the growth behavior of Fe catalyst supported on the different pristine and ion beam-damaged supporting substrates using C_2H_4 and FTS-GP as feedstock, our next focus is to investigate CNT growth efficiency for substrates that support carpet growth. CNT growth efficiency is defined in terms of activity and lifetime of the supported catalyst. The catalytic activity refers to the increase in the CNT carpet height with time while the catalyst lifetime is defined as the duration until growth termination occurs. Figure 3.3 shows plots of CNT carpet height versus growth time for catalyst supported on the different supporting layers with C_2H_4 or FTS-GP as a feedstock. The shaded region in each plot shows the 95% confidence interval on the fitted values. In general, the growth profiles exhibit characteristic features of CNT carpet growth kinetics with an initial acceleration, an inflection point, followed by gradual deactivation and eventually growth termination [54-56]. In comparison to C_2H_4, CNT carpet growth using FTS-GP exhibits a higher growth rate and longer catalyst lifetime. In Figure 3.3a, growth with FTS-GP feedstock for three different crystalline phases of $MgAl_2O_4$ (100, 110, and 111) exhibits somewhat similar growth profiles: high growth efficiency and resistance to deactivation as the catalysts appear active after 180 min. On the other hand, growth with C_2H_4 (Figure 3.3b) exhibits significantly lower efficiency with gradual deactivation occurring after 30 min followed by deactivation before 100 min; the maximum carpet heights attained after 120 min are all in the sub-micrometer range. Unlike FTS-GP, another unique feature of growth using C_2H_4 is the high sensitivity of its growth behavior to the crystallographic phase of $MgAl_2O_4$ spinel. It can be concluded that growth efficiency decreased in the following order: $MgAl_2O_4$ (111) > $MgAl_2O_4$ (110) > $MgAl_2O_4$ (100).

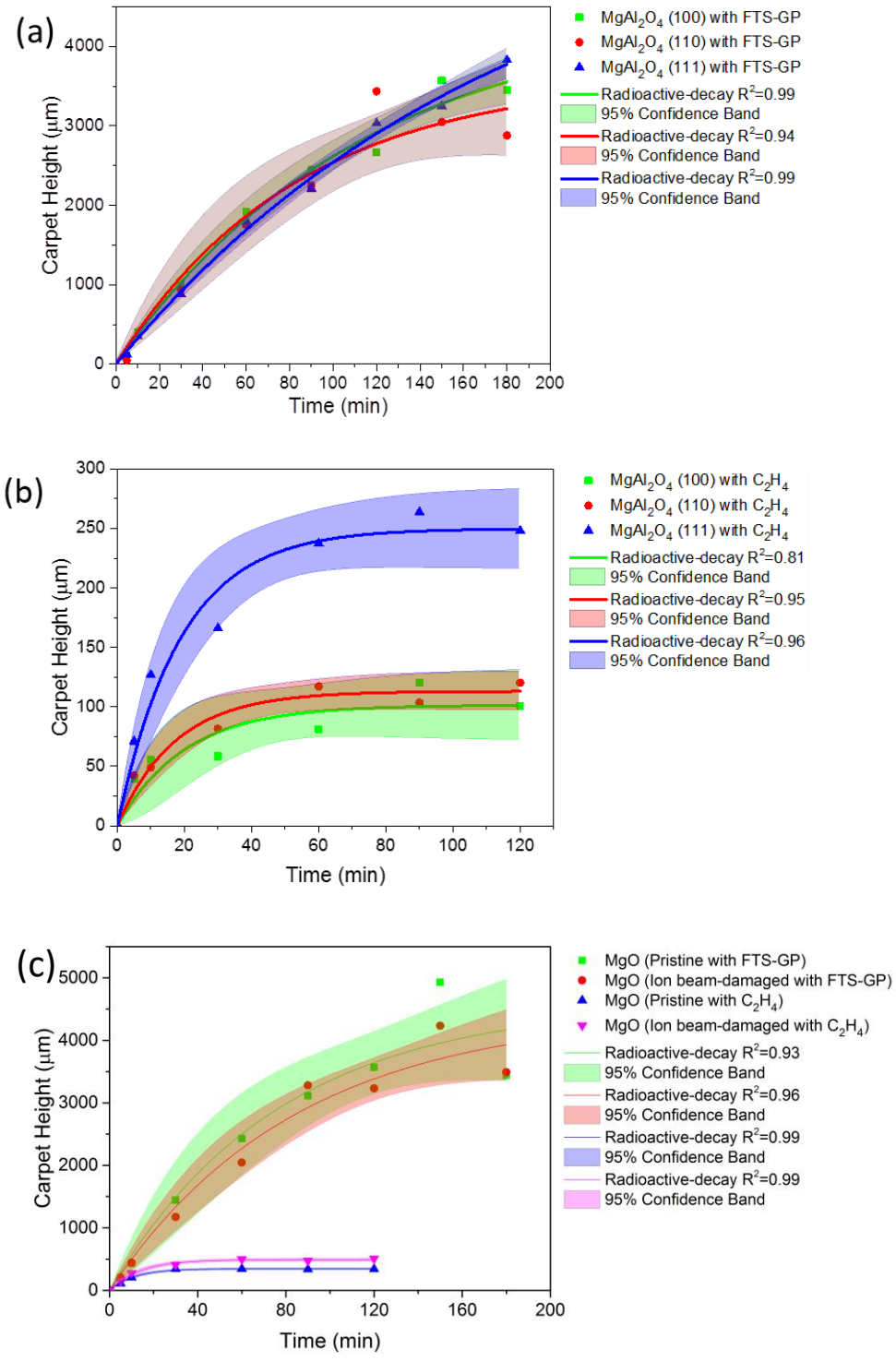

Figure 3.3 Plots of CNT carpet heights as functions of growth time for ion beam-damaged $MgAl_2O_4(100)$, $MgAl_2O_4(110)$, $MgAl_2O_4(111)$ substrates using FTS-GP (a), CNT carpet heights as functions of growth time for ion beam-damaged $MgAl_2O_4(100)$, $MgAl_2O_4(110)$, $MgAl_2O_4(111)$ substrates using C_2H_4 (b), CNT carpet heights as functions of growth time for pristine and ion beam-damaged MgO(100) substrates (c). The respective shades around the plot shows the 95% confidence interval on the fitted data.

To compare the growth behaviors, the growth data are further analyzed to extract kinetic information. As demonstrated by Futaba et al. [55], the time evolution of CNT carpet growth can be modeled using the radioactive-decay equation represented by the following differential equation:

$$\frac{\partial H}{\partial t} \propto e^{-\frac{t}{\tau 0}} \qquad (1)$$

where H is the carpet height, t is the growth time, τ_0 is a fitting parameter. Integration of Equation 1 yields the growth equation:

$$H(t) = \beta\tau_0\,(1 - e^{-\frac{t}{\tau_0}}) \qquad (2)$$

where H is the carpet height, t is the growth time, β is the initial growth rate and τ_0 is the characteristic catalyst lifetime.

By fitting the radioactive-decay model to our growth data, we are able to determine β and τ_0, which are fitting parameters that characterize the growth behavior of catalyst supported on each supporting layer. These fitting parameters have been used to estimate the growth efficiency of CNT carpets. From the fitting, the model equations for $MgAl_2O_4$ (100), $MgAl_2O_4$ (110) and $MgAl_2O_4$ (111) substrates grown with FTS-GP are $H(t) = 4466.85\,(1 - e^{-\frac{t}{113.38}})$, $H(t) = 3635.03(1 - e^{-\frac{t}{83.18}})$ and $H(t) = 5987.15\,(1 - e^{-\frac{t}{180.78}})$, respectively. Extracted β parameters are 39.2 μm/min [$MgAl_2O_4$ (100)], 43.7 μm/min [$MgAl_2O_4$ (110)] and 33.3 μm/min [$MgAl_2O_4$ (111)] while extracted τ_0 parameters are 113 min [$MgAl_2O_4$ (100)], 83 min [$MgAl_2O_4$ (110)] and 181 min [$MgAl_2O_4$ (111)]. From the results, $MgAl_2O_4$ (110) shows the highest initial growth rate. The characteristic catalyst lifetime of $MgAl_2O_4$ (111) is higher than that of $MgAl_2O_4$ (110) by a factor of two. According to the growth parameter, the product of β and τ_0 is the theoretical carpet height (H_{max}). As shown in Figure 3.4, CNT carpets grown on $MgAl_2O_4$ (111) show H_{max}

of 5987 µm, which is the highest among all $MgAl_2O_4$ substrates. This trend is also consistent with τ_0 that indicates that longer lifetimes are achieved with FTS-GP as a precursor.

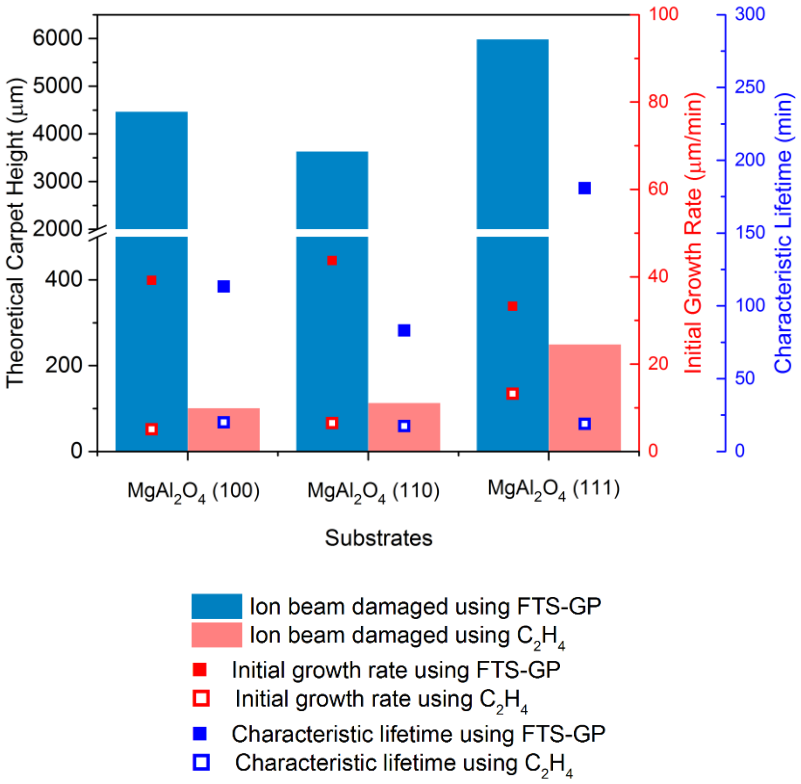

Figure 3.4 Plots of the characteristic lifetime (blue dots), initial growth rate (red dots), and theoretical carpet height (histogram) as a function of different $MgAl_2O_4$ spinel structure.

The fitted model equation for $MgAl_2O_4$ (100), $MgAl_2O_4$ (110) and $MgAl_2O_4$ (111) substrates in Figure 3.3b are $H(t) = 101.15\ (1 - e^{-\frac{t}{20.03}})$, $H(t) = 113.04(1 - e^{-\frac{t}{17.38}})$ and $H(t) = 249.85\ (1 - e^{-\frac{t}{18.92}})$, respectively. Extracted β parameters are 5.1 µm/min [$MgAl_2O_4$ (100)], 6.5 µm/min [$MgAl_2O_4$ (110)] and 13.2 µm/min [$MgAl_2O_4$ (111)] while extracted τ_0 parameters are 20 min [$MgAl_2O_4$ (100)], 17 min [$MgAl_2O_4$ (110)] and 19 min [$MgAl_2O_4$ (111)]. A comparison of the two carbon sources used in this study (Figure 3.3a and 3c) reveals a stark difference in the growth efficiencies, with FTS-GP outperforming C_2H_4 in terms of initial growth

rate and catalyst lifetime of Fe on $MgAl_2O_4$ substrate. It is therefore unsurprising that growth of CNT carpets with FTS-GP is able to achieve millimeter-tall heights while growth using C_2H_4 only yields sub-millimeter-tall CNT carpets. Among all three substrates, $MgAl_2O_4$ (111) shows the highest initial growth rate which indicates this type of spinel structure is most suitable for CNT growth. In Figure 3.4, $MgAl_2O_4$ (111) shows highest H_{max} in both FTS-GP and C_2H_4 growth experiments. This indicates the spinel structure affects CNT growth. However, the $MgAl_2O_4$ (111) sample did not show the highest τ_0 when C_2H_4 was used, which is inconsistent with the growth behavior observed with FTS-GP precursor. We conclude that the precursor type plays a more important role in extending catalyst lifetime.

Figure 3.3c exhibits the growth profiles for pristine and ion beam-damaged MgO (100) substrates grow with FTS-GP and C_2H_4. The model equations of CNT carpet grow from FTS-GP are $H(t) = 4608.91\ (1 - e^{-\frac{t}{76.77}})$ and $H(t) = 4459.19\ (1 - e^{-\frac{t}{84.42}})$ for pristine and ion beam-damaged MgO (100) substrate, respectively. The β and τ_0 are 60.0 μm/min, 77 min for pristine MgO (100) and 52.8 μm/min, 84 min for ion beam-damaged MgO (100). The CNT grown on pristine and ion beam-damaged MgO (100) substrates using C_2H_4 precursor shows a model of $H(t) = 345.59(1 - e^{-\frac{t}{11.23}})$ and $H(t) = 490.93(1 - e^{-\frac{t}{13.59}})$ where the β and τ_0 are 30.8 μm/min, 11 min and 36.1 μm/min, 13.6 min, respectively. The observed growth behavior with FTS-GP and C_2H_4 is consistent with our previous conclusion that use of FTS-GP as a feedstock enhances catalyst lifetime; in fact for MgO (100), the characteristic lifetime increases by a factor of almost 6 and the H_{max} increased by a factor of 9.

Figure 3.5 shows a summary of the theoretical and experimental CNT carpet height results. In Figure 3.5a, growth using FTS-GP shows the carpet heights from experiment are shorter than the theoretical carpet heights, indicating catalysts are yet to reach their maximum

lifetime. However, CNT growth using C_2H_4 shows experimentally obtained carpet heights are similar to the theoretical heights, which indicates catalysts have reached their final lifetime. In Figure 3.5b, all samples appear to have reached their catalyst lifetimes because their experimental CNT lengths are very close to H_{max}. Therefore, all $MgAl_2O_4$ substrates show longer lifetimes than MgO (100) substrate. Based on our results presented so far, we conclude that FTS-GP precursor is able to enhance catalyst lifetime and CNT growth rate. We attribute the excellent performance of FTS-GP to the unique composition and possible in situ generation of water via a reaction between H_2 and CO as previously proposed [57].

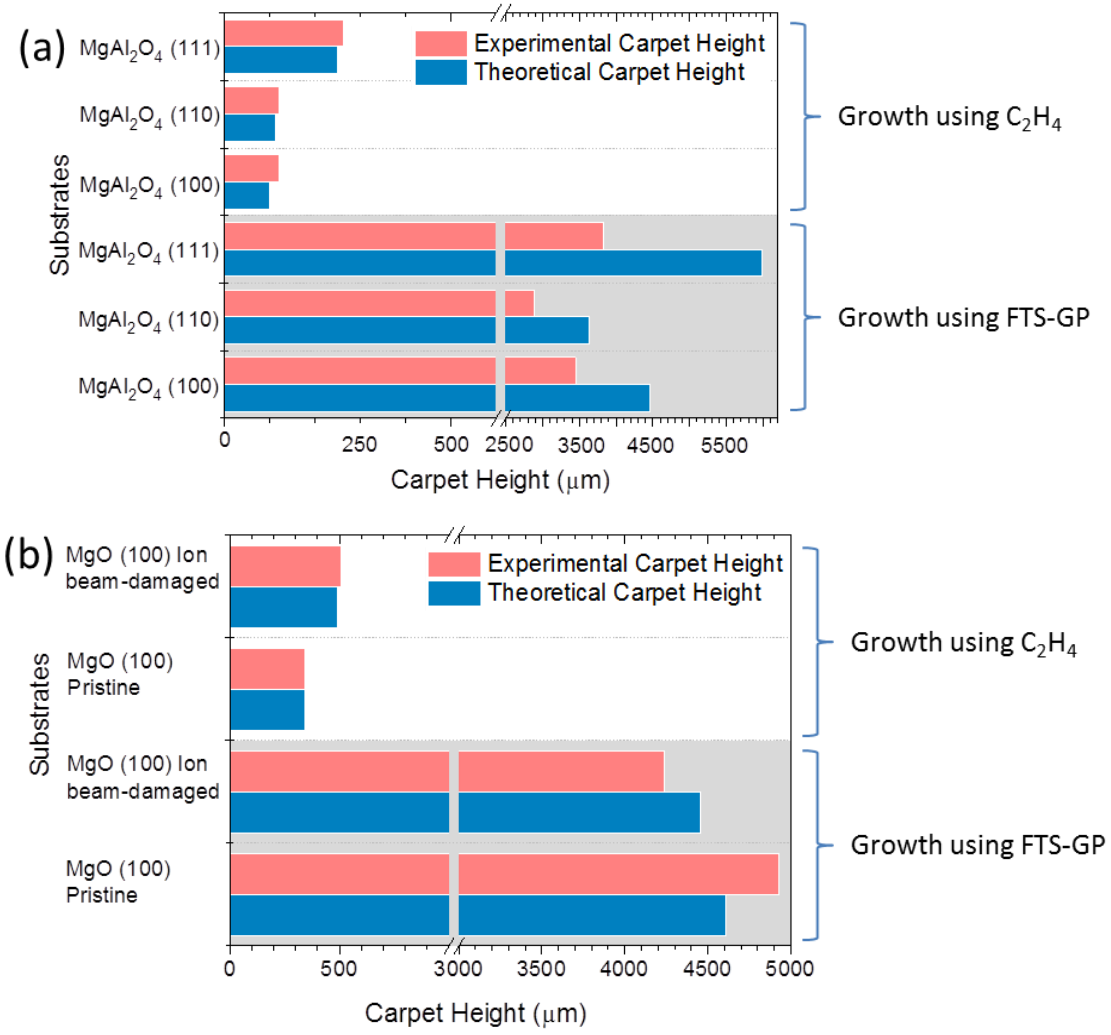

Figure 3.5 Comparison between theoretical and experimental CNT carpet heights for different $MgAl_2O_4$ spinel substrates (a), MgO (100) substrate (b).

The XRR measurements were carried out to investigate the surface properties of substrates. Figure 3.6a and b show XRR interference pattern acquired from pristine and ion beam-damaged $MgAl_2O_4$ spinel of different phases and MgO substrates. Fitting the interference fringes with the theoretically generated XRR patterns reveals the formation of an upper amorphous layer (Layer 1) and a lower nanocrystalline layer (Layer 2) on top of the crystalline substrate after ion beam bombardment. Figure 3.7 are plots of the thickness and roughness of substrate layers which were extracted from fitting of the XRR interference fringes in Figure 3.6. After ion beam bombardment, the thickness of Layer 1 increased significantly. However, the thickness of Layer 2 remains roughly unchanged after ion beam bombardment. From Figure 3.7, we conclude the overall surface roughness for all substrates is increased after ion beam bombardment. The surface roughness may also play a role in anchoring catalyst particles, impeding sintering and extending catalyst lifetime. Interestingly, our experimental results support this hypothesis as the catalyst life time increased with the increasing surface roughness. The surface roughness decreased in the following order: $MgAl_2O_4$ (111) > $MgAl_2O_4$ (100) > $MgAl_2O_4$ (110) which is consistent with τ_0 when growth is carried out with FTS-GP.

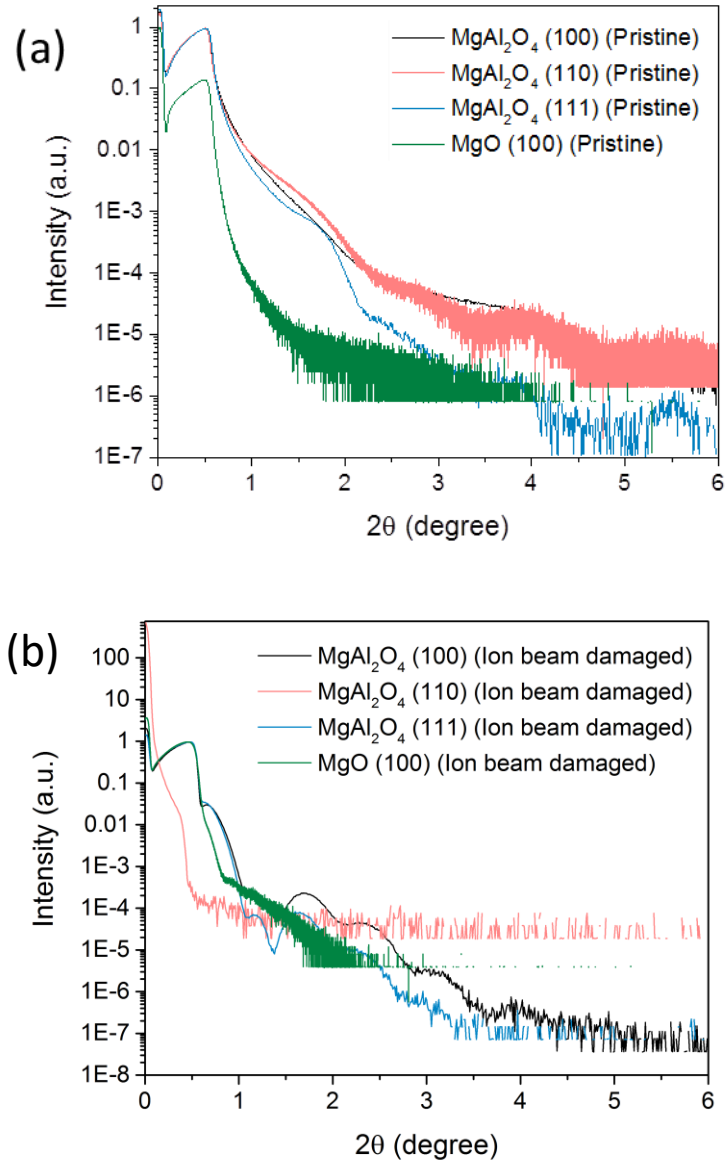

Figure 3.6 XRR profiles of pristine substrates (a) and ion beam-bombarded substrates (b).

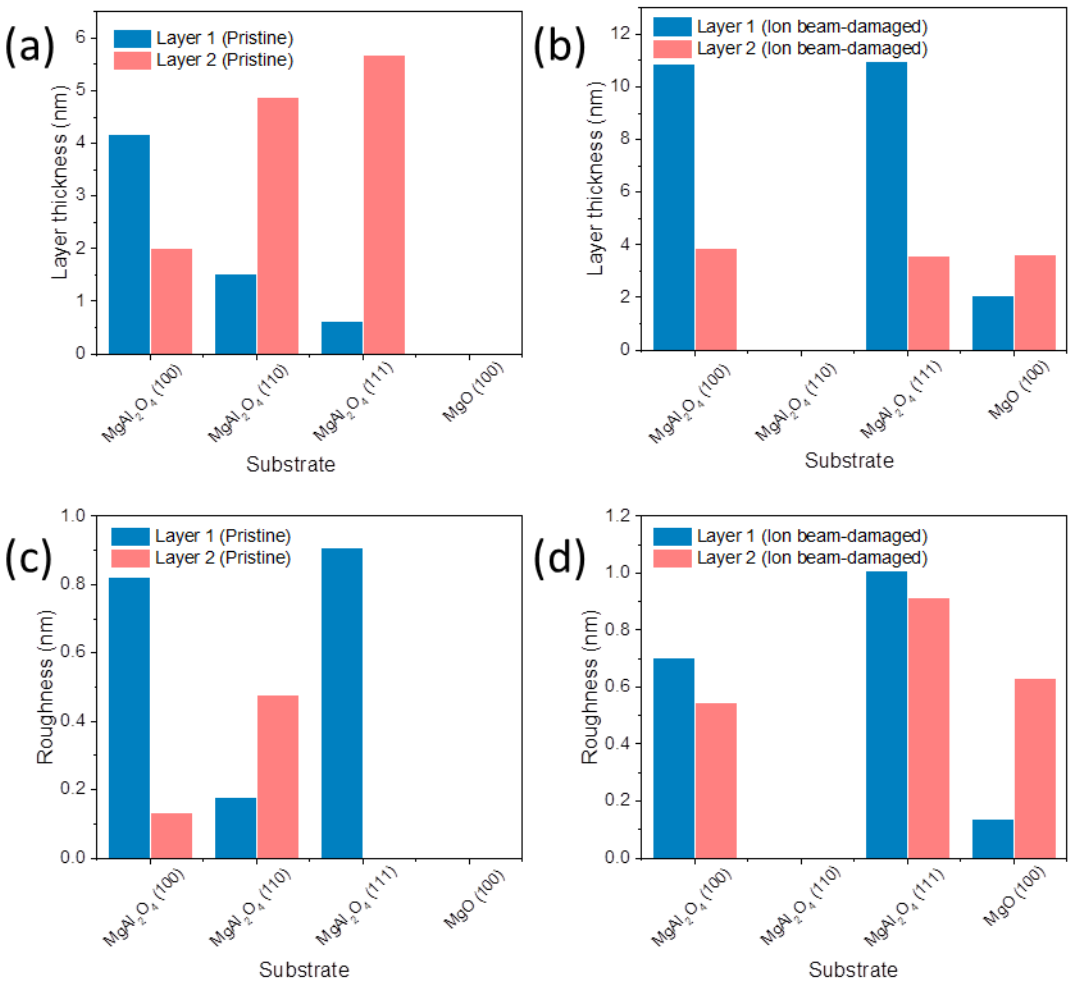

Figure 3.7 XRR results of the thickness of different layers present at the surface of pristine (a) and ion beam-bombarded substrates (b), roughness of different layers present at the surface of pristine (c) and ion beam-bombarded substrates (d).

3.4 Discussion

From the SEM images in Figure 3.1, pristine $MgAl_2O_4$ supporting substrates are less active than MgO (100). However, the use of ion beam bombardment to modify the $MgAl_2O_4$ substrate improved the activity of supported Fe catalyst on the substrate, which is consistent with previous studies [38, 58]. As shown in previous studies [37, 38, 59], the role of ion beam bombardment is to create porosity and increase roughness on the substrates surface. These studies have shown that ion beam bombardment is capable of transforming a highly crystalline

surface into an amorphous-like surface. The total effective depth of the amorphous layer is around 10 nm, which allows for mild subsurface reaction of the catalyst, an important criterion for efficient CNT carpet growth [12]. It is known that material with high surface basicity favors the CNT growth [19]. In this work, the high activity of catalyst supported on MgO may be attributed in part to the high surface basicity.

The Raman results indicate that CNTs grown from FTS-GP precursor have superior quality, which is also consistent with our previous study [60]. FTS-GP consist of H_2 (40%), CH_4 (30%), C_2H_6 (8%), C_2H_4 (6%), CO (5%), C_3H_8 (5%), N_2 (4%), and C_3H_6 (2%). Under CNT growth conditions, it is hypothesized a reaction between H_2 and CO would generate small amount of H_2O at the catalyst site, which can act as an oxidant to etch amorphous carbon deposited on the catalyst, extending the catalyst lifetime. The high carbon flux from the carbon-rich components of FTS-GP to the catalysts contribute to the high growth rate.

To rationalize the observed differences in growth behavior for catalysts supported on three spinel structures of $MgAl_2O_4$, we consider the atomic stacking sequence of the different surface orientations of $MgAl_2O_4$ spinel as shown in Figure 3.6. Unlike the mixed aluminum/oxygen atomic arrangement on the surface of $MgAl_2O_4$ (100) and $MgAl_2O_4$ (110), the top surface of $MgAl_2O_4$ (111) is fully covered with oxygen atoms [49, 61, 62], which is evidence of a higher surface basicity than the other two substrates. As mentioned above, a highly basic surface is good for CNT growth. Secondly, the surface energy of different $MgAl_2O_4$ spinel structures are also different. It has been reported the surface energies of the $MgAl_2O_4$ phases decrease in the following order: $MgAl_2O_4$ (111) > $MgAl_2O_4$ (110) > $MgAl_2O_4$ (100) [49, 61]. It has been shown that a relatively high surface energy can prevent planar Ostwald ripening and subsurface diffusion [37]. Therefore, the above synergistic effect in $MgAl_2O_4$ (111) substrate

makes it a preferred substrate for CNT growth especially when conventional precursors are used. An illustration of the effects of the composition, surface terminating species of the spinel structures and the catalyst preparation steps on CNT carpet growth is presented in Figure 3.8. CNT growth behavior is affected by the different atomic surface arrangement that forms a catalyst-substrate interaction that is unique.

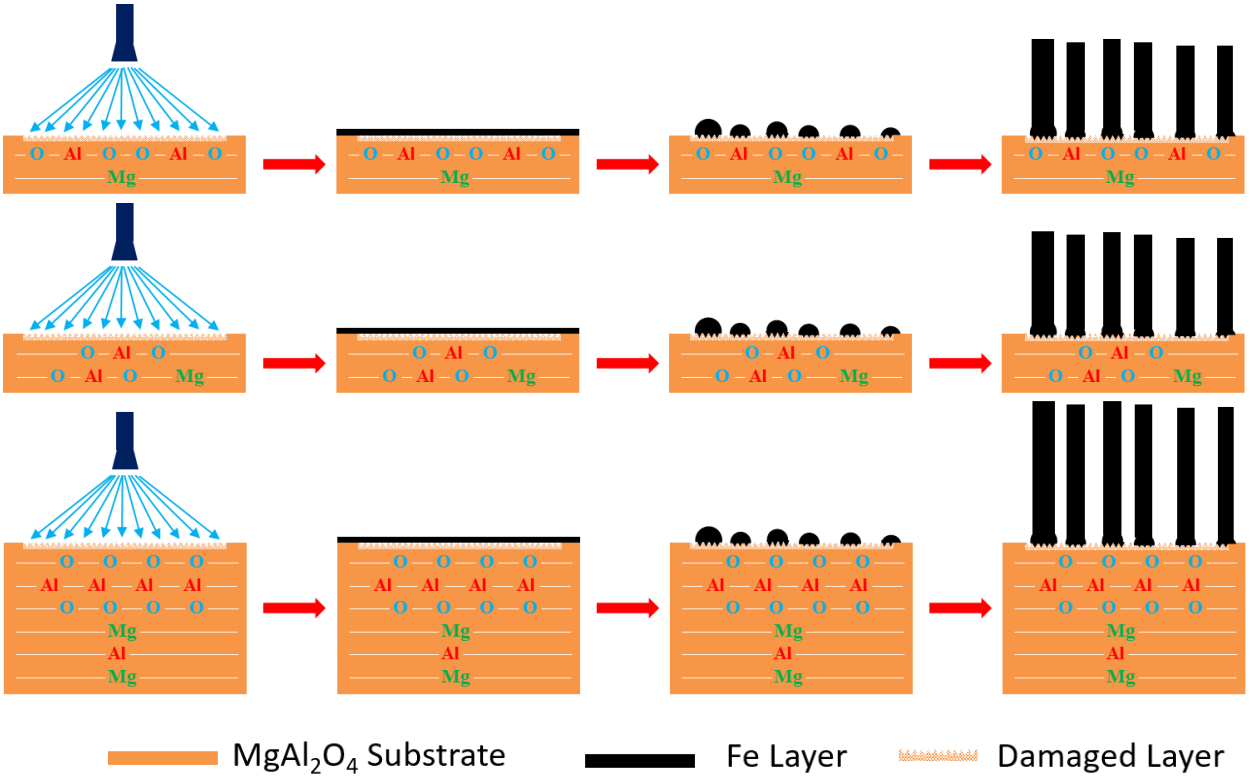

Figure 3.8 A schematic illustration of CNT arrays grown on different phases of $MgAl_2O_4$ spinel substrates.

3.5 Conclusions

In conclusion, we have investigated the growth behavior of pristine and ion beam-damaged $MgAl_2O_4$ (100), $MgAl_2O_4$ (110), $MgAl_2O_4$ (111) and MgO (100) using a conventional feedstock (C_2H_4) and an industrial waste gaseous mixture (FTS-GP) as a feedstock. The role of ion beam bombardment is transforming a highly crystallized surface into an amorphous surface

to enhance the CNT growth process. The surface basicity is an important property for substrate to have as it promotes good CNT carpet growth. Although different phases of $MgAl_2O_4$ substrates have the same chemical composition, they still show different CNT growth behavior due to their different surface chemistries and surface energies. $MgAl_2O_4$ (111) is the best supporting layer among all $MgAl_2O_4$ substrates due to its high surface basicity and relatively high surface energy. FTS-GP outperforms C_2H_4 (conventional precursor) as a feedstock for CNT carpet growth. Our novel gaseous waste mixture is capable of enhancing CNT growth rate and extending catalyst lifetime.

3.6 References

[1] W. Wang, P.N. Kumta, Nanostructured hybrid silicon/carbon nanotube heterostructures: reversible high-capacity lithium-ion anodes, *ACS Nano*, 4 (2010) 2233-2241.

[2] C.L. Pint, N.W. Nicholas, S. Xu, Z. Sun, J.M. Tour, H.K. Schmidt, R.G. Gordon, R.H. Hauge, Three dimensional solid-state supercapacitors from aligned single-walled carbon nanotube array templates, *Carbon*, 49 (2011) 4890-4897.

[3] H. Chen, M. Chen, J. Di, G. Xu, H. Li, Q. Li, Architecting three-dimensional networks in carbon nanotube buckypapers for thermal interface materials, *The Journal of Physical Chemistry C*, 116 (2012) 3903-3909.

[4] B.A. Cola, J. Xu, C. Cheng, X. Xu, T.S. Fisher, H. Hu, Photoacoustic characterization of carbon nanotube array thermal interfaces, *Journal of Applied Physics*, 101 (2007) 054313.

[5] W. Li, C. Liang, W. Zhou, J. Qiu, Z. Zhou, G. Sun, Q. Xin, Preparation and characterization of multiwalled carbon nanotube-supported platinum for cathode catalysts of direct methanol fuel cells, *The Journal of Physical Chemistry B*, 107 (2003) 6292-6299.

[6] K. Gong, F. Du, Z. Xia, M. Durstock, L. Dai, Nitrogen-doped carbon nanotube arrays with high electrocatalytic activity for oxygen reduction, *Science*, 323 (2009) 760-764.

[7] K. Saetia, J.M. Schnorr, M.M. Mannarino, S.Y. Kim, G.C. Rutledge, T.M. Swager, P.T. Hammond, Spray‐Layer‐by‐Layer Carbon Nanotube/Electrospun Fiber Electrodes for Flexible Chemiresistive Sensor Applications, *Advanced Functional Materials*, 24 (2014) 492-502.

[8] E. Llobet, Gas sensors using carbon nanomaterials: A review, *Sensors and Actuators B: Chemical*, 179 (2013) 32-45.

[9] R. Baker, Catalytic growth of carbon filaments, *Carbon*, 27 (1989) 315-323.

[10] K.A. Shah, B.A. Tali, Synthesis of carbon nanotubes by catalytic chemical vapour deposition: A review on carbon sources, catalysts and substrates, *Materials Science in Semiconductor Processing*, 41 (2016) 67-82.

[11] C. Mattevi, C.T. Wirth, S. Hofmann, R. Blume, M. Cantoro, C. Ducati, C. Cepek, A. Knop-Gericke, S. Milne, C. Castellarin-Cudia, In-situ X-ray photoelectron spectroscopy study of catalyst− support interactions and growth of carbon nanotube forests, *The Journal of Physical Chemistry C*, 112 (2008) 12207-12213.

[12] P.B. Amama, C.L. Pint, S.M. Kim, L. McJilton, K.G. Eyink, E.A. Stach, R.H. Hauge, B. Maruyama, Influence of alumina type on the evolution and activity of alumina-supported Fe catalysts in single-walled carbon nanotube carpet growth, *ACS Nano*, 4 (2010) 895-904.

[13] A. Magrez, R. Smajda, J.W. Seo, E. Horvath, P.R. Ribič, J.C. Andresen, D. Acquaviva, A. Olariu, G. Laurenczy, L.s. Forró, Striking influence of the catalyst support and its acid–base properties: new Insight into the growth mechanism of carbon nanotubes, *ACS Nano*, 5 (2011) 3428-3437.

[14] Y. Wang, Z. Luo, B. Li, P.S. Ho, Z. Yao, L. Shi, E.N. Bryan, R.J. Nemanich, Comparison study of catalyst nanoparticle formation and carbon nanotube growth: support effect, *Journal of Applied Physics*, 101 (2007) 124310.

[15] J. Ward, B. Wei, P. Ajayan, Substrate effects on the growth of carbon nanotubes by thermal decomposition of methane, *Chemical Physics Letters*, 376 (2003) 717-725.

[16] R.L. Vander Wal, T.M. Ticich, V.E. Curtis, Substrate–support interactions in metal-catalyzed carbon nanofiber growth, *Carbon*, 39 (2001) 2277-2289.

[17] N. Nagaraju, A. Fonseca, Z. Konya, J.B. Nagy, Alumina and silica supported metal catalysts for the production of carbon nanotubes, *Journal of Molecular Catalysis A: Chemical*, 181 (2002)

57-62.

[18] C. Zhang, F. Yan, C. Allen, B. Bayer, S. Hofmann, B. Hickey, D. Cott, G. Zhong, J. Robertson, Growth of vertically-aligned carbon nanotube forests on conductive cobalt disilicide support, *Journal of Applied Physics*, 108 (2010) 024311.

[19] P.B. Amama, S.A. Putnam, A.R. Barron, B. Maruyama, Wetting behavior and activity of catalyst supports in carbon nanotube carpet growth, *Nanoscale*, 5 (2013) 2642-2646.

[20] J.W. Ward, B.Q. Wei, P.M. Ajayan, Substrate effects on the growth of carbon nanotubes by thermal decomposition of methane, *Chemical Physics Letters*, 376 (2003) 717-725.

[21] A. Magrez, R. Smajda, J.W. Seo, E. Horváth, P.R. Ribič, J.C. Andresen, D. Acquaviva, A. Olariu, G. Laurenczy, L. Forró, Striking Influence of the Catalyst Support and Its Acid–Base Properties: New Insight into the Growth Mechanism of Carbon Nanotubes, *ACS Nano*, 5 (2011) 3428-3437.

[22] C. Zhang, F. Yan, C.S. Allen, B.C. Bayer, S. Hofmann, B.J. Hickey, D. Cott, G. Zhong, J. Robertson, Growth of vertically-aligned carbon nanotube forests on conductive cobalt disilicide support, *Journal of Applied Physics*, 108 (2010) 024311.

[23] H. Hongo, M. Yudasaka, T. Ichihashi, F. Nihey, S. Iijima, Chemical vapor deposition of single-wall carbon nanotubes on iron-film-coated sapphire substrates, *Chemical Physics Letters*, 361 (2002) 349-354.

[24] N. Ishigami, H. Ago, K. Imamoto, M. Tsuji, K. Iakoubovskii, N. Minami, Crystal plane dependent growth of aligned single-walled carbon nanotubes on sapphire, *Journal of the American Chemical Society*, 130 (2008) 9918-9924.

[25] L. Qingwen, Y. Hao, C. Yan, Z. Jin, L. Zhongfan, A scalable CVD synthesis of high-purity single-walled carbon nanotubes with porous MgO as support material, *Journal of Materials*

Chemistry, 12 (2002) 1179-1183.

[26] H. Ago, K. Nakamura, S. Imamura, M. Tsuji, Growth of double-wall carbon nanotubes with diameter-controlled iron oxide nanoparticles supported on MgO, *Chemical Physics Letters*, 391 (2004) 308-313.

[27] T. de los Arcos, M.G. Garnier, P. Oelhafen, D. Mathys, J.W. Seo, C. Domingo, J.V. Garcıa-Ramos, S. Sanchez-Cortes, Strong influence of buffer layer type on carbon nanotube characteristics, *Carbon*, 42 (2004) 187-190.

[28] B. Wang, Y. Yang, L.-J. Li, Y. Chen, Effect of different catalyst supports on the (n, m) selective growth of single-walled carbon nanotube from Co–Mo catalyst, *Journal of Materials Science*, 44 (2009) 3285-3295.

[29] A. Kudo, S.A. Steiner III, B.C. Bayer, P.R. Kidambi, S. Hofmann, M.S. Strano, B.L. Wardle, CVD growth of carbon nanostructures from zirconia: mechanisms and a method for enhancing yield, *Journal of the American Chemical Society*, 136 (2014) 17808-17817.

[30] C. Mattevi, C.T. Wirth, S. Hofmann, R. Blume, M. Cantoro, C. Ducati, C. Cepek, A. Knop-Gericke, S. Milne, C. Castellarin-Cudia, In-situ X-ray photoelectron spectroscopy study of catalyst− support interactions and growth of carbon nanotube forests, *Journal of Physical Chemistry C*, 112 (2008) 12207-12213.

[31] N. Suguru, H. Kei, S. Hisashi, K. Kazunori, Z. Zhengyi, M. Shigeo, Y. Yukio, Millimeter-Thick Single-Walled Carbon Nanotube Forests: Hidden Role of Catalyst Support, *Japanese Journal of Applied Physics*, 46 (2007) L399.

[32] I. Willems, Z. Kónya, J.F. Colomer, G. Van Tendeloo, N. Nagaraju, A. Fonseca, J.B. Nagy, Control of the outer diameter of thin carbon nanotubes synthesized by catalytic decomposition of hydrocarbons, *Chemical Physics Letters*, 317 (2000) 71-76.

[33] N. Yoshihara, H. Ago, M. Tsuji, Chemistry of Water-Assisted Carbon Nanotube Growth over Fe−Mo/MgO Catalyst, *The Journal of Physical Chemistry C*, 111 (2007) 11577-11582.

[34] C. Masarapu, B. Wei, Direct Growth of Aligned Multiwalled Carbon Nanotubes on Treated Stainless Steel Substrates, *Langmuir*, 23 (2007) 9046-9049.

[35] C.E. Baddour, F. Fadlallah, D. Nasuhoglu, R. Mitra, L. Vandsburger, J.-L. Meunier, A simple thermal CVD method for carbon nanotube synthesis on stainless steel 304 without the addition of an external catalyst, *Carbon*, 47 (2009) 313-318.

[36] D. Yu, Q. Zhang, L. Dai, Highly Efficient Metal-Free Growth of Nitrogen-Doped Single-Walled Carbon Nanotubes on Plasma-Etched Substrates for Oxygen Reduction, *Journal of the American Chemical Society*, 132 (2010) 15127-15129.

[37] P.B. Amama, A.E. Islam, S.M. Saber, D.R. Huffman, B. Maruyama, Understanding properties of engineered catalyst supports using contact angle measurements and X-Ray reflectivity, *Nanoscale*, 8 (2016) 2927-2936.

[38] X. Li, M. Baker-Fales, H. Almkhelfe, N.R. Gaede, T.S. Harris, P.B. Amama, Rational Modification of a Metallic Substrate for CVD Growth of Carbon Nanotubes, *Scientific Reports*, 8 (2018) 4349.

[39] Y. Gao, Y.J. Kim, S. Thevuthasan, S.A. Chambers, P. Lubitz, Growth, structure, and magnetic properties of γ-Fe2O3 epitaxial films on MgO, *Journal of Applied Physics*, 81 (1997) 3253-3256.

[40] H. Ago, K. Nakamura, N. Uehara, M. Tsuji, Roles of Metal−Support Interaction in Growth of Single- and Double-Walled Carbon Nanotubes Studied with Diameter-Controlled Iron Particles Supported on MgO, *The Journal of Physical Chemistry B*, 108 (2004) 18908-18915.

[41] H.Y. Wang, E. Ruckenstein, CO2 reforming of CH4 over Co/MgO solid solution catalysts

— effect of calcination temperature and Co loading, *Applied Catalysis A: General*, 209 (2001) 207-215.

[42] J. Li, J. Li, Q. Zhu, Carbon deposition and catalytic deactivation during CO2 reforming of CH4 over Co/MgO catalyst, *Chinese Journal of Chemical Engineering*, 26 (2018) 2344-2350.

[43] Q. Zhang, M. Zhao, J. Huang, W. Qian, F. Wei, Selective Synthesis of Single/Double/Multi-walled Carbon Nanotubes on MgO-Supported Fe Catalyst, *Chinese Journal of Catalysis*, 29 (2008) 1138-1144.

[44] I. Ganesh, S. Bhattacharjee, B.P. Saha, R. Johnson, K. Rajeshwari, R. Sengupta, M.V. Ramana Rao, Y.R. Mahajan, An efficient MgAl2O4 spinel additive for improved slag erosion and penetration resistance of high-Al2O3 and MgO–C refractories, *Ceramics International*, 28 (2002) 245-253.

[45] S.A. Bocanegra, A.D. Ballarini, O.A. Scelza, S.R. de Miguel, The influence of the synthesis routes of MgAl2O4 on its properties and behavior as support of dehydrogenation catalysts, *Materials Chemistry and Physics*, 111 (2008) 534-541.

[46] J. Sehested, A. Carlsson, T.V.W. Janssens, P.L. Hansen, A.K. Datye, Sintering of Nickel Steam-Reforming Catalysts on MgAl2O4 Spinel Supports, *Journal of Catalysis*, 197 (2001) 200-209.

[47] F. Wang, W.-Z. Li, J.-D. Lin, Z.-Q. Chen, Y. Wang, Crucial support effect on the durability of Pt/MgAl2O4 for partial oxidation of methane to syngas, *Applied Catalysis B: Environmental*, 231 (2018) 292-298.

[48] W. Bing, M. Wei, Recent advances for solid basic catalysts: Structure design and catalytic performance, *Journal of Solid State Chemistry*, 269 (2019) 184-194.

[49] M.M. Hasan, P.P. Dholabhai, R.H. Castro, B.P. Uberuaga, Stabilization of $MgAl_2O_4$ spinel

surfaces via doping, *Surface Science*, 649 (2016) 138-145.

[50] Y. Fu, L. Zhang, B. Yue, X. Chen, H. He, Simultaneous Characterization of Solid Acidity and Basicity of Metal Oxide Catalysts via the Solid-State NMR Technique, *The Journal of Physical Chemistry C*, 122 (2018) 24094-24102.

[51] P.F. Rossi, G. Busca, V. Lorenzelli, M. Waqif, O. Saur, J.C. Lavalley, Surface basicity of mixed oxides: magnesium and zinc aluminates, *Langmuir*, 7 (1991) 2677-2681.

[52] G.-Y. Xiong, D. Wang, Z. Ren, Aligned millimeter-long carbon nanotube arrays grown on single crystal magnesia, *Carbon*, 44 (2006) 969-973.

[53] M. Maret, K. Hostache, M.-C. Schouler, B. Marcus, F. Roussel-Dherbey, M. Albrecht, P. Gadelle, Oriented growth of single-walled carbon nanotubes on a MgO (001) surface, *Carbon*, 45 (2007) 180-187.

[54] M. Bedewy, E.R. Meshot, M.J. Reinker, A.J. Hart, Population Growth Dynamics of Carbon Nanotubes, *ACS Nano*, 5 (2011) 8974-8989.

[55] D.N. Futaba, K. Hata, T. Yamada, K. Mizuno, M. Yumura, S. Iijima, Kinetics of Water-Assisted Single-Walled Carbon Nanotube Synthesis Revealed by a Time-Evolution Analysis, *Physical Review Letters*, 95 (2005) 056104.

[56] S.M. Kim, C.L. Pint, P.B. Amama, D.N. Zakharov, R.H. Hauge, B. Maruyama, E.A. Stach, Evolution in Catalyst Morphology Leads to Carbon Nanotube Growth Termination, *The Journal of Physical Chemistry Letters*, 1 (2010) 918-922.

[57] H. Almkhelfe, J. Carpena-Nunez, T.C. Back, P.B. Amama, Gaseous product mixture from Fischer-Tropsch synthesis as an efficient carbon feedstock for low temperature CVD growth of carbon nanotube carpets, *Nanoscale*, 8 (2016) 13476-13487.

[58] A. Islam, P. Nikolaev, P. Amama, S. Saber, D. Zakharov, D. Huffman, M. Erford, G.

Sargent, S. Semiatin, E. Stach, Engineering the activity and lifetime of heterogeneous catalysts for carbon nanotube growth via substrate ion beam bombardment, *Nano Letters*, 14 (2014) 4997-5003.

[59] A.E. Islam, P. Nikolaev, P.B. Amama, S. Saber, D. Zakharov, D. Huffman, M. Erford, G. Sargent, S.L. Semiatin, E.A. Stach, B. Maruyama, Engineering the Activity and Lifetime of Heterogeneous Catalysts for Carbon Nanotube Growth via Substrate Ion Beam Bombardment, *Nano Lettters*, 14 (2014) 4997-5003.

[60] H. Almkhelfe, X. Li, R. Rao, P.B. Amama, Catalytic CVD growth of millimeter-tall single-wall carbon nanotube carpets using industrial gaseous waste as a feedstock, *Carbon*, 116 (2017) 181-190.

[61] C.M. Fang, S.C. Parker, G. de With, Atomistic simulation of the surface energy of spinel $MgAl_2O_4$, *Journal of the American Ceramic Society*, 83 (2000) 2082-2084.

[62] F.R. Massaro, M. Bruno, F. Nestola, Configurational and energy study of the (100) and (110) surfaces of the $MgAl_2O_4$ spinel by means of quantum mechanical and empirical techniques, *CrystEngComm*, 16 (2014) 9224-9235.

Chapter 4 - Characterization and Catalytic Behavior of Fischer-Tropsch Catalysts Derived from Different Cobalt Precursors

4.1 Introduction

Concerns about dwindling crude-oil reserves and their negative impact of carbon-based fuels on the environment are forcing researchers to seek new routes that yield clean fuels and chemicals [1, 2]. Fischer-Tropsch synthesis (FTS) provides a pathway for the transformation of biomass, coal or natural gas into fuels and chemicals using a transition metal, such as Fe, Co, or Ru, as a catalyst [3, 4]. Among these catalysts, Ru-based types exhibit the highest activity and C5+ selectivity [5]. However, due to the high cost of Ru, its widespread use in FTS is limited [6]. Although Fe is an earth-abundant transition metal, it is plagued by its high water-gas shift (WGS) reaction activity, thus lowering C5+ selectivity [7, 8]. Conversely, Co-based catalysts exhibit relatively higher activity and selectivity to long-chain paraffins, high resistance to deactivation, and a low WGS reaction activity [9, 10]. Therefore, well-dispersed Co-based catalysts supported on silica or alumina are generally preferred in FTS.

A number of studies have demonstrated high dependence of catalytic performance on the type of catalyst precursor [11-13] and synthesis method used [14-16]. Iglesia's group has shown the turnover frequency (TOF) of Co catalysts is dependent on the concentration of active sites and is independent of the nature of the support and dispersion of Co catalysts [17-19]. While Co-based FT catalysts have been synthesized with different precursors, the most commonly used precursor is $Co(NO_3)_2$ [3]. Unlike Co catalysts derived from $Co(NO_3)_2$, those derived from

$Co(C_2H_3O_2)_2$, as reported by Girardon et al. [20], exhibit low reducibility; the study also reveals that catalysts derived from $Co(C_2H_3O_2)_2$ easily form a hard-to-reduce compound during calcination thereby limiting FTS activity. On the contrary, work by Zhang and coworkers [21] revealed that γ-Al_2O_3-supported catalysts prepared from $Co(C_2H_3O_2)_2$ tend to form CoO after thermal treatment in N_2, which shows higher activity than Co_3O_4 prepared from $Co(NO_3)_2$. SiO_2-supported Co catalysts derived from $CoCl_2$, as reported by Bae et al. [12], show low FTS activity and C5+ selectivity because the residual chloride ions (Cl^-) poison the catalyst during FTS reaction. Panpranot et al. [22] attribute the low FTS performance of Co catalysts prepared from $CoCl_2$ to the blockage of catalytic sites by residual Cl^-. A series of Co carbonyl clusters were also used as Co precursors in preparation of FTS catalysts [23]; the dispersion of Co catalysts prepared from Co carbonyl clusters exhibits better catalytic activity than those prepared from $Co(NO_3)_2$. Unlike FT catalysts derived from traditional precursors, cobalt carbonyl clusters are able to provide metallic particles in their zero valent state and, therefore, do not require aggressive reduction treatment. However, synthesis of Co carbonyl clusters results in catalysts with different surface acidities that affect CO conversion and C5+ selectivity [23].

In our previous investigation, we showed that cobalt hydroxide is a promising precursor for synthesis of well-dispersed Co catalysts on carbon nanotubes (CNTs) via a modified photo-Fenton process [15]. The resulting CNT-supported Co catalyst does not require a calcination step and is free of possible catalyst inhibitors usually present in conventional catalyst precursors such as nitrates, chlorides, acetates, and carbonyls; FTS reaction with this catalyst shows high CO conversion (~80%) and outstanding C5+ selectivity (~70%). In all, a number of Co precursors have been used for synthesis of Co catalysts on SiO_2 support [12, 20, 24-26]; however, some fundamental questions related to how precursor type affects catalyst reducibility, hydrocarbon

product distribution, and catalyst lifetime remain unanswered. The behavior of catalysts derived from a green precursor [$Co(OH)_2$] and supported on a conventional substrate such as SiO_2 or Al_2O_3 is, however, noteworthy.

Motivated by the lack of understanding of the effect of precursor type (including a novel "green" precursor) on FTS catalysis, this study investigates the properties and catalytic performance of SiO_2-supported Co catalysts derived from $Co(OH)_2$, $Co(NO_3)_2$, $Co(C_2H_3O_2)_2$, and $CoCl_2$ via incipient wetness impregnation. The synthesized catalysts are characterized using a wide range of techniques including transmission electron microscopy and spectroscopy (TEM), X-ray diffraction (XRD), temperature-programmed reduction (TPR), X-ray photoelectron spectroscopy (XPS), and X-ray absorption spectroscopy (XAS). In addition, the catalytic performance (CO conversion, C5+ selectivity, and C5+ product distribution) and stability of the synthesized catalysts during FTS are evaluated and compared. Further, post-mortem characterization of the catalysts are conducted using TEM, XAS, and XRD to elucidate structural and chemical changes.

4.2 Experimental

4.2.1 Catalyst preparation

Co/SiO_2 catalysts were synthesized via conventional incipient wetness impregnation from different Co precursors: $Co(NO_3)_2 \cdot 6H_2O$ (Aldrich, ⩾98% purity), $Co(C_2H_3O_2)_2 \cdot 4H_2O$ (Aldrich, ⩾98% purity), $CoCl_2 \cdot 6H_2O$ (Aldrich, ⩾98% purity), and $Co(OH)_2$ (Strem, ⩾97% purity). Catalyst solutions were prepared by dissolving each precursor in water except for $Co(OH)_2$, which was dissolved in hydrogen peroxide (30%), a good solvent for $Co(OH)_2$ that is free of possible catalyst inhibitors. Based on prior studies [27, 28], the possibility of $Co(OH)_2$ and H_2O_2

reacting to form CoO(OH), under our synthesis conditions, is unlikely because the mixture was maintained at room temperature in the absence of NaOH. Silica gel (Aldrich, pore size 60Å, 100 mesh) was used as a catalyst support. Impregnation of the prepared catalyst solutions in SiO_2 resulted in a catalyst loading of ca. 20wt%. Thereafter, all freshly synthesized SiO_2-supported Co catalysts were dried at 120°C, followed by calcination at 550°C for all catalysts except those synthesized from $Co(OH)_2$. SiO_2-supported Co catalysts prepared using $Co(NO_3)_2$, $Co(C_2H_3O_2)_2$, $CoCl_2$, and $Co(OH)_2$ are designated as Co-Nit, Co-Ace, Co-Chl, and Co-Hyd, respectively. Calcined Co-Nit, Co-Ace, and Co-Chl catalysts, as well as uncalcined Co-Hyd, were used for catalytic testing, and are hereafter referred to as fresh catalysts.

4.2.2 Catalyst characterization

Textural properties of the catalysts were determined by N_2 physisorption at -196°C using an Autosorb-1 series system. Prior to physisorption measurements, all the fresh catalysts were outgassed at 250°C for 10h. The Brunauer-Emmet-Teller (BET) [29] method was applied to the adsorption isotherm in the linear range of relative pressure from 0.02 to 0.35 to determine the specific surface area of each catalyst. Pore size distribution was determined from the desorption branch at a relative pressure of 0.95 of the isotherm using the Barrett-Joyner-Halenda (BJH) [30] model.

XRD analyses were conducted to identify atomic and molecular structures of fresh catalysts. XRD patterns were recorded on a Rigaku Miniflex II desktop X-ray diffractometer using Cu Kα radiation (λ =1.54056 Å) in the range of $10° < 2\theta < 80°$ with a step size of 0.10° and scan speed of 1.00°/min. The average crystallite size of Co_3O_4 in the fresh catalysts was

estimated by the Scherrer equation (Equation 1) [31], where $d_{Co_3O_4}$ is average crystallite size, λ=1.54056Å, β is full width at half maximum (FWHM), and 2θ = 36.9°.

$$d_{Co_3O_4} = \frac{0.94\lambda}{\beta cos\theta} \qquad (1)$$

The actual Co loading ratio of fresh catalysts was verified by inductively coupled plasma atomic emission spectroscopy (ICP-Varian 720-ES).

The reducibility of fresh catalysts was studied by temperature programmed reduction (TPR) in an AMI-200 catalyst characterization system equipped with a thermal conductivity detector. 0.1g of sample was put into a U-shaped quartz tube and pre-treated to remove moisture and impurities under helium flow (30 ml/min) at 140°C for 1h. Thereafter, the sample was cooled to 40°C and heated again to 900°C at a ramping rate of 10°C/min under a flow of 10% H_2 in Ar at 30 ml/min while the hydrogen consumption was measured. The reducibility of the catalyst (R_{Co}) was calculated using Equation 2:

$$R_{Co} = \frac{reduced\ amount\ of\ Co}{total\ amount\ of\ Co} \times 100\% \qquad (2)$$

The steps for calculating the reduced amount of Co from the TPR profile are presented in the Supplementary Information.

To characterize the catalyst morphology, TEM images were obtained using (FEI Tecnai F20 XT) operating at 200 kV. The samples were dropped on a copper microgrid coated with lacey carbon film.

XPS measurements were performed on a Kratos Ultra XPS system with a monochromatic Al Kα source (hν =1486.6 eV). The effect of charging were reduced with a charge neutralizer. High-resolution spectra were acquired at 20 eV pass energy with 0.1 eV steps. Analysis of XPS spectra was performed using CasaXPS software. Components in the high-resolution spectra were fit with a combination of Gaussian and Lorentzian peak shapes. All metallic components also

included an asymmetry parameter. The fitting routine used a Levenburg-Marquardt routine to minimize χ^2.

X-ray absorption near-edge structure (XANES) and edge X-ray absorption fine structure (EXAFS) were performed at the Inner Shell Spectroscopy beamline at the National Synchrotron Light Source-II. Samples were diluted with BN and pressed into pellets for measurements in a transmission geometry. Data were collected from ~200 eV below the Co K-edge (7709 eV) to ~1100 past the Co K-edge. Data processing and subsequent structure modeling were performed with the Athena and Artemis data packages, respectively [32], wherein a S_0^2 value of 0.812 was used in calculations and obtained from modeling the EXAFS from a reference Co foil. Known bulk structures for metallic Co, Co_3O_4, CoO, and β-$Co(OH)_2$ where used in EXAFS modeling when needed while a computed CoOOH structure from the materials project was used for certain scattering paths [33].

4.2.3 Catalytic testing

The activity and product selectivity of catalysts were evaluated using a stainless steel tubular fixed-bed reactor ½-inch in diameter. Typically, 2g of catalyst mixed with 8g of SiC was loaded into the reactor. SiC is an inert diluent material with high thermal conductivity (k = 4W/cm K) used to enhance temperature uniformity across the reaction bed [34]. Prior to FTS reaction, each catalyst was activated at the optimum reduction temperature determined from TPR data. Co-Nit and Co-Hyd catalysts were reduced *in situ* by flowing 100 sccm H_2 and 100 sccm N_2 under atmospheric pressure for 12h at 350°C while Co-Ace and C-Chl were reduced *in situ* at 450°C under similar conditions. After reduction, the reactor was cooled to 120°C under flowing N_2, followed by increasing the pressure to 150 psi by introducing 100 sccm H_2, 50 sccm CO, and

100 sccm N_2. Next, the temperature was slowly increased to 230°C at a heating rate of 1°C/min to prevent instability associated with the highly exothermic FTS reaction. The reaction was allowed to run for 30h. Once steady state was achieved, the reaction was allowed to proceed for 15h. The stream of effluents from the reactor was depressurized to atmospheric pressure through a pressure-relief valve and passed through a heated line maintained at 150°C with a heating tape attached to an online gas chromatograph (GC, SRI-8610C) equipped with a TCD, FID, and methanizer.

CO conversion was calculated according to Equation 3, where $F_{CO,in}$ is inlet CO molar flow rate and $F_{CO,out}$ is outlet CO molar flow rate.

$$CO\ conversion\ (\%) = \frac{F_{CO,in} - F_{CO,out}}{F_{CO,in}} \qquad (3)$$

Product selectivity was calculated based on Equation 4, where n is the carbon number of product (C_n); $F_{Cn,\ out}$ is the outlet molar flow rate of product C_n.

$$Selectivity\ (\%) = \frac{nF_{C_n,out}}{F_{CO,in} - F_{CO,out}} \qquad (4)$$

The chain-growth probability (α) was obtained from the Anderson–Schultz–Flory chain-length statistics equation (Equation 5) [35], where W_n is the mass fraction of the species with carbon number n. From the slope of the plot of ln (W_n/n) against n, the value of α can be obtained.

$$\ln\left(\frac{W_n}{n}\right) = n\ln\alpha + const \qquad (5)$$

The turnover frequency (TOF) based on catalyst reducibility data from TPR was determined from:

$$TOF = \frac{-r_{CO} M_{Co}}{D_{Co} x_{Co}} \qquad (6)$$

where $-r_{CO}$ is the CO reaction rate, M_{Co} is atomic weight of Co, x_{Co} is the weight ratio of Co in the catalyst, and D_{Co} is the Co dispersion.

4.3 Results and discussion

4.3.1 Catalyst characterization

4.3.1.1 Nitrogen adsorption–desorption

A summary of the properties of fresh catalysts is presented in Table 4.1. The BET specific surface area (SA_{BET}) of Co-Nit, Co-Ace, and Co-Chl are 317, 336, and 331 m²/g, respectively. In contrast, Co-Hyd exhibits a higher SA_{BET} of 432 m²/g, which is close to that of pristine SiO_2 support. This result suggests the absence of calcination in preparation of Co-Hyd allows SiO_2 (support material) to preserve its structural properties. Total pore volume and pore diameter of the catalysts increase in the following order: Co-Nit < Co-Ace < Co-Chl < Co-Hyd. The results also show the surface area, total pore volume, and pore diameter decrease after Co impregnation, which is in agreement with previous studies [36, 37]. An increase in catalyst pore diameter has been shown to improve FTS activity [8, 38]. It is noteworthy that catalysts derived from different precursors exhibit different pore structures with Co-Hyd showing the highest pore diameter. Although the standard incipient wetness impregnation method usually yields catalysts with decreased surface area and pore diameter [39], the opposite effect is observed in the case of Co-Hyd, possibly due to the absence of a calcination step that prevents catalyst sintering and unfavorable interactions between catalyst support and active phase prior to FTS.

4.3.1.2 X-ray diffraction

XRD patterns of the freshly prepared catalysts (Co-Nit, Co-Ace, Co-Chl, and Co-Hyd) are shown in Figure 4.1. The wide diffraction peak at 2θ of 22.3°, ascribed to SiO_2 support, is in all diffraction patterns. Co-Nit, Co-Ace, and Co-Chl show diffraction peaks at 2θ of 19.0°, 31.3°, 36.9°, 44.8°, 59.4°, and 65.2° due to the presence of crystalline Co_3O_4 spinel (PDF 42-1467) [8]. For Co-Hyd, diffraction peaks at 2θ of 19.0°, 32.5°, 37.9°, 51.4°, 57.9°, and 61.5° are indicative of the presence of β-$Co(OH)_2$ (PDF 30-0443) [28]. It can be concluded from the XRD data that Co exists in the form of Co_3O_4 in all fresh catalysts except Co-Hyd, where the composition is mainly $Co(OH)_2$. As shown in Table 4.1, the estimated crystallite size obtained from XRD using the Scherrer equation are in the range of 11-35 nm.

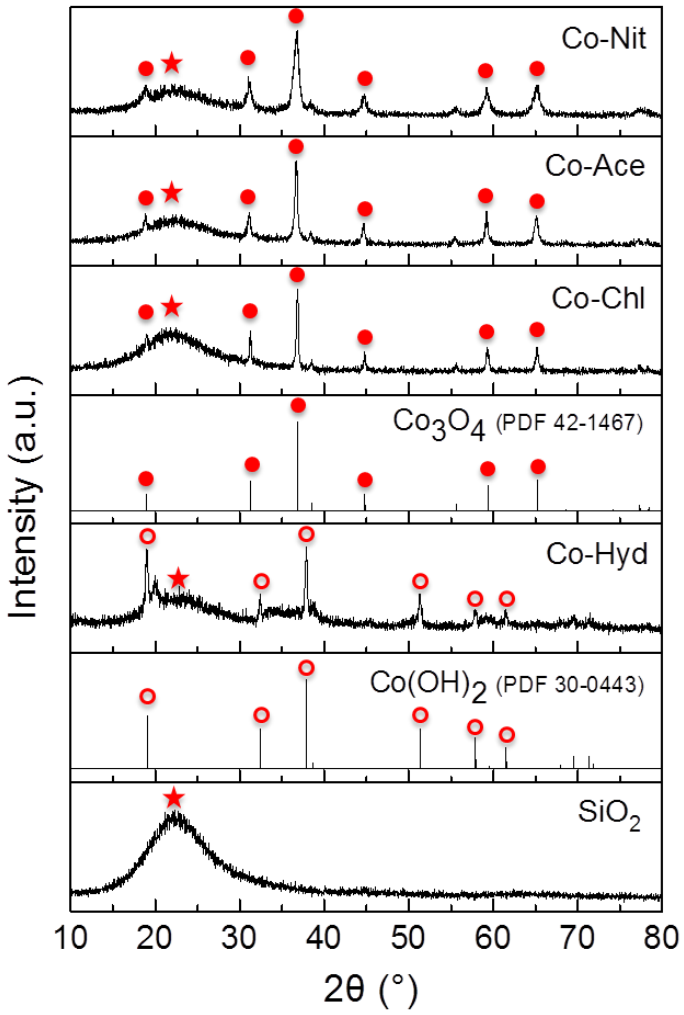

Figure 4.1. XRD patterns of fresh silica-supported cobalt catalysts prepared from different cobalt precursors [$Co(NO_3)_2$, $Co(C_2H_3O_2)_2$, $CoCl_2$, and $Co(OH)_2$].

Table 4.1. Summary of properties of catalyst support and fresh cobalt catalysts derived from different cobalt precursors.

Catalysts	Name	Surface Area (m^2/g)	Total Pore Volume (cm^3/g)	Average pore Size (Å)	$d_{(Co3O4)}$[a] (nm)	$d_{(Co3O4)}$[b] (nm)	Reducibility (%)
$Co(NO_3)_2/SiO_2$	Co-Nit	316.8	0.64	81.53	3.7	11.4	94.77
$Co(C_2H_4O_2)_2/SiO_2$	Co-Ace	336.0	0.70	83.89	3.0	25.9	88.82
$CoCl_2/SiO_2$	Co-Chl	331.3	0.72	87.10	2.8	35.4	64.24
$Co(OH)_2/SiO_2$	Co-Hyd	432.3	0.97	89.88	4.0	25.7	91.06
SiO_2	-	457.0	1.02	90.01	-	-	-

[a]Average catalyst diameter from TEM
[b]Average crystallite size from XRD

4.3.1.3 Transmission electron microscopy

Figure 4.2 shows high-magnification TEM images of freshly prepared Co-Nit, Co-Ace, Co-Chl, and Co-Hyd, and their corresponding histograms of particle size distributions (PSDs) with Gaussian analysis fittings. The high-magnification images reveal small catalyst particles that are well-dispersed on SiO_2 support for all fresh catalysts. As the histograms show, all fresh catalysts have particle sizes and standard deviations that are similar. However, low-magnification images (Figure C4.1) of all fresh catalyst reveal the presence of a small fraction of large particles in the range of 20 – 30 nm that are not apparent in the high-magnification images. The discrepancy in average particle size obtained from XRD and TEM may be due to the limited sensitivity of XRD to the presence of very small crystallite particles of cobalt oxides; in particular, particles ~3nm, the approximate average size of particles from high-magnification TEM, are poorly detected by XRD [40]. In spite of the controversy surrounding the so-called particle-size effect in FTS, it is generally accepted that catalyst size has a profound impact on activity and selectivity [9, 41-43]. Larger Co particles exhibit higher selectivity for higher molecular weight hydrocarbons due to the

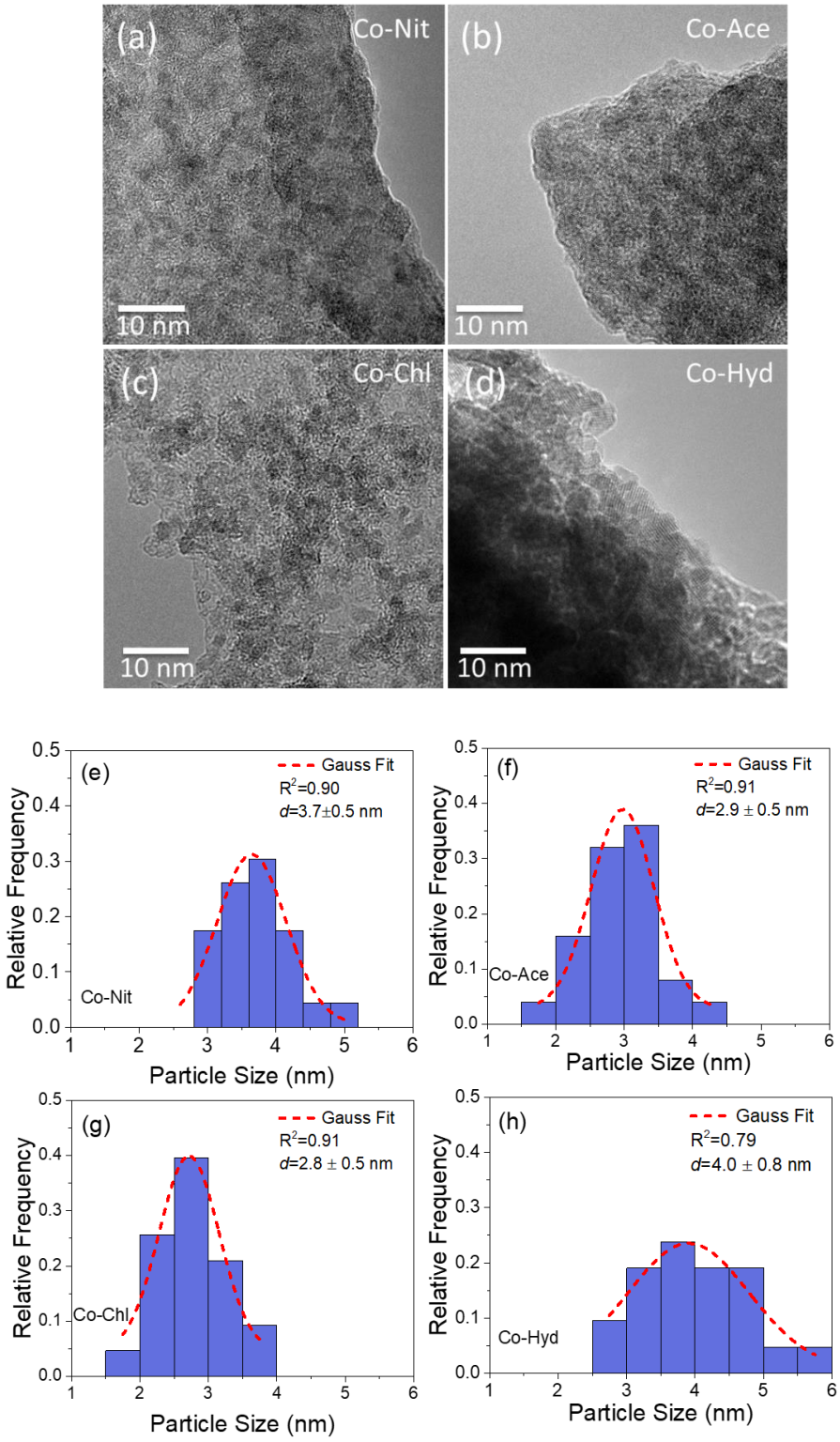

Figure 4.2. High-magnification TEM images and corresponding histograms of PSDs with Gaussian analysis fitting of fresh silica-supported catalysts prepared from different cobalt precursors: $Co(NO_3)_2$ (a and e), $Co(C_2H_3O_2)_2$ (b and f), $CoCl_2$ (c and g), and $Co(OH)_2$ (d and h).

formation of -CH_2- intermediate via dissociative adsorption of CO. As verified by TEM, the average catalyst size for Co-Nit, Co-Ace, Co-Chl, and Co-Hyd are in the narrow range of 3 to 4 nm, which minimizes the influence of particle size during FTS and allows for meaningful comparison and the isolation of the intrinsic role of precursor type and properties.

4.3.1.4 Hydrogen temperature-programmed reduction (H_2-TPR)

H_2-TPR profiles presented in Figure 4.3 show the reduction behavior of the SiO_2-supported cobalt catalysts. Typically, a Co_3O_4 undergoes a two-step reduction process. The first step, which occurs at a relatively lower temperature, involves reduction of Co_3O_4 to CoO while the second step that occurs at a relatively higher temperature involves reduction of CoO to Co^0 [8, 44]. In Figure 4.3a, it is clear the reduction of Co-Nit occurs in two steps, the first at 325°C and the second at 385°C. Figure 4.3b shows a single peak at 460°C and a small bump at 365°C, which may indicate the presence of mixed oxides (CoO and Co_3O_4) for Co-Ace. The small bump at 365°C is attributed to the reduction of Co_3O_4 to CoO. Thus, TPR results suggest CoO is the main cobalt phase in Co-Ace catalyst. In support of our TPR peak assignment, a number of studies [20, 45, 46] have shown the presence of only a small fraction of Co species in the form of Co_3O_4 in Co catalyst prepared from cobalt acetate. In our case, we speculate that the dominant CoO particles in Co-Ace are too small to be detected by XRD; the observed XRD pattern for Co-Ace is mostly from a small fraction of large Co_3O_4 particles observed in the low-magnification TEM images (Figure C4.1). The absence of a high-temperature reduction peak (> 600°C) for Co-Ace indicates relatively weak catalyst-support interactions. Conversely, the small and ill-defined high-temperature reduction peaks in the profiles of Co-Hyd, Co-Nit, and Co-Chl are evidence of strong catalyst-support interaction and possible formation of irreducible compounds. Because calcination, reduction, and FTS reaction were conducted at temperatures below 600°C, the

observed catalyst-support interactions are not expected to contribute to catalyst deactivation. Figure 4.3c shows only one broad peak at 450°C for Co-Chl that is most likely due to the overlap of the two reduction peaks associated with Co_3O_4. The TPR profile of Co-Hyd is shown in Figure 4.3d and the peak at 320°C is the only intense peak with a distinct shoulder at a higher reduction temperature. As confirmed by XRD (Figure 4.1), Co-Hyd contains mainly $Co(OH)_2$. Yang et al. showed that $Co(OH)_2$ decomposes at 130°C to form Co_3O_4 via a dehydrogenation reaction; this indicates that there is the possibility of simultaneous decomposition and reduction during TPR. XRD analysis of samples annealed in either N_2 or H_2 at 300 and 400°C revealed interesting results (Figure C4.2): (1) Co_3O_4 is the main product after annealing $Co(OH)_2$ in N_2 at 300°C, but a small fraction of CoO begins to form at 400°C; (2) annealing in H_2 at 300°C yields mixed Co species (Co_3O_4, CoO and Co metal) while at 400°C, metallic Co is obtained. Therefore, TPR of $Co(OH)_2$ forms Co_3O_4 and CoO that are subsequently reduced to Co metal as reduction progresses. The results also suggest that $Co(OH)_2$ is fully reduced at 400°C in H_2 irrespective of the decomposition products formed during annealing. The possible existence of Co^{3+} and Co^{2+} in Co-Hyd is consistent with the broad TPR peak observed. Moreover, the broad peaks between 600°C and 800°C for Co-Nit, Co-Chl and Co-Hyd correspond to the reduction of Co species with strong interactions with SiO_2 support [38, 43, 47]. Acetate-derived catalysts are known to readily form hard-to-reduce compounds during annealing; the absence of high-temperature peaks in Co-Ace may be due to prior formation of silicates during calcination. We emphasize that among the four catalysts, Co-Hyd exhibits the lowest reduction temperature, and is, therefore, the most easily activated under FTS reaction conditions.

From Figure 4.3, reduction temperatures of Co-Nit and Co-Hyd are below 400°C while those of Co-Ace and Co-Chl are higher. As a result, the two sets of catalysts, those with lower

(Co-Nit and Co-Hyd) and higher reduction temperatures (Co-Ace and Co-Chl), were reduced at 350°C and 450°C prior to FTS, respectively. The reducibility of catalysts increases in the following order: Co-Chl (64.2%) < Co-Ace (88.8%) < Co-Hyd (91.1%) < Co-Nit (94.8%). Basically, this trend is somewhat consistent with the reduction temperatures of the catalysts as evidenced by Co-Hyd and Co-Nit that reduce at low temperatures showing very high reducibility (>90%). Unlike Co-Hyd and Co-Nit, the relatively low reducibility of Co-Chl (64.24%) indicates the presence of a limited amount of active Co species for catalyzing FTS reaction.

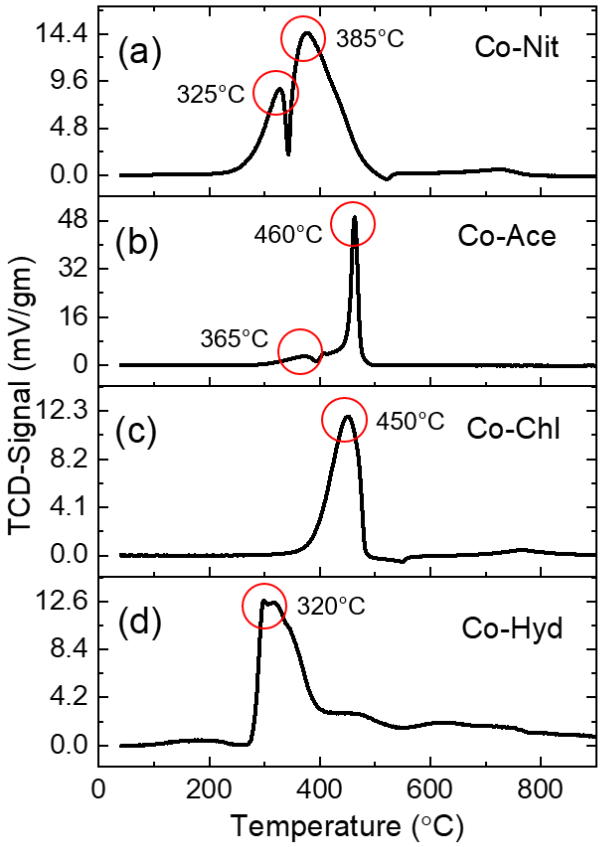

Figure 4.3. H_2-TPR profiles of silica-supported cobalt catalysts prepared from different precursors: (a) $(Co(NO_3)_2$, (b) $Co(C_2H_3O_2)_2$, (c) $CoCl_2$, and (d) $Co(OH)_2$.

4.3.1.5 X-ray photoelectron spectroscopy

The high-resolution Co 2p XPS spectra of the fresh catalysts in Figure 4.4 show the characteristic doublet (Co $2p_{3/2}$ and $2p_{1/2}$) with satellite peaks from spin-orbit splitting. Because both Co $2p_{3/2}$ and $2p_{1/2}$ peaks qualitatively contain the same information, curve fitting has been restricted to the higher-intensity Co $2p_{3/2}$ peak. Here an improved curve-fitting methodology reported by Biesinger et al. [48] is used for interpretation of 2p spectra of Co (details are not provided here to avoid duplication). The Co $2p_{3/2}$ peak and shake-up satellite features for Co-Nit and Co-Chl are centered on 779.3 and 789.0 eV, respectively. Evidently, distinct shake-up satellite features for Co $2p_{3/2}$ and Co $2p_{1/2}$ are present in the spectra from Co-Nit and Co-Chl, and the satellite peak observed ~789.0 eV is used to confirm the presence of Co_3O_4 [3, 49, 50]. The so-called 'shake-up' features are associated with either a coupling between unpaired electrons in the atom or a multiple-electron excitation [28]. Also, an intense Co 2p peak accompanied by a satellite peak of low intensity is associated with formation of Co_3O_4 [51]; the presence of these features in the spectra of Co-Nit and Co-Chl is further evidence of Co existing as Co_3O_4, in agreement with XRD results (Figure 4.1). Co 2p spectrum of Co-Hyd is similar to the standard spectrum for $Co(OH)_2$ reported by Biesinger et al. [48], with shake-up satellite features of Co $2p_{3/2}$ peak components that shift to lower-binding energies at 784.9 eV and 788.3 eV [28, 48]. Therefore, Co-Hyd is mainly composed of $Co(OH)_2$, in agreement with XRD results (Figure 4.1). The composition of Co-Hyd as revealed by XPS is unsurprising, as it does not undergo calcination that could have induced thermal decomposition to its oxide. In the case of Co-Ace, Co $2p_{3/2}$ and corresponding satellite peaks are centered around 780.4 and 786.7 eV, respectively [48, 51], suggesting a Co^{2+} state that is most likely CoO, which is, interestingly, inconsistent

with XRD data (Figure 4.1) as peaks from Co-Ace are indexed as Co_3O_4. All Co $2p_{3/2}$ peak components are summarized in the Supplementary Information (Table C6.1). The discrepancy in the chemical species identified by XPS and XRD for Co-Ace may be due to the limited sensitivity of XRD to small particles. Low and high-magnification TEM analysis reveal the presence of a small fraction of large particles in the range of 20 – 35nm and a large fraction of small particles ~3nm. The consistency observed in the variation of the average particle size obtained from low-magnification TEM and XRD (Table C6.2) is further evidence of the selective detection of mainly large particles by XRD. We, therefore, conclude that Co-Ace is composed of a small fraction of large Co_3O_4 particles that are easily detected by XRD and XPS, and a large fraction of small CoO particles that are only detected by XPS. For all fresh catalysts, the number density of small particles are significantly higher than large particles by at least a factor of 10 (Table C6.2); the significance of this result is twofold: First, the large fraction of small particles are the dominant active sites. Second, the result explains why the XPS spectrum for Co-Ace is consistent with CoO, not Co_3O_4. The observed formation of CoO in Co-Ace is supported by the work of Zhang et al. [21] that revealed the susceptibility of Co catalysts derived from cobalt acetate to form CoO.

To further verify our conclusions, the intensity ratio of the Co $2p_{1/2}$ satellite to its main peak for fresh catalysts is compared; studies [49, 52, 53] have shown this ratio, which is ~0.9 for CoO and ~0.3 for Co_3O_4, can be used to distinguish between the two oxides. The calculated ratio for Co-Ace, Co-Nit, Co-Chl, and Co-Hyd are 0.5, 0.3, 0.2, and 0.3, respectively. All the samples except for Co-Ace have a ratio that is ~0.3, indicating the dominant Co species is present as Co_3O_4. However, the ratio for Co-Ace is 0.5, between the values expected for CoO and Co_3O_4, even though the XPS spectrum is consistent with that of CoO. XRD detects only Co_3O_4 while

XPS detects both CoO and Co_3O_4. We hypothesize the ratio is higher for Co-Ace due to the presence of mixed oxides, with a low fraction of large Co_3O_4 particles and a high fraction of small CoO particles. We conclude from XPS data that the Co phase formed is sensitive to the Co precursor used during synthesis. The results reveal the formation of Co_3O_4 for Co-Nit and Co-Chl while Co-Hyd is composed mainly of $Co(OH)_2$, in agreement with XRD data (Figure 4.1). On the other hand, Co-Ace yields nanoparticles with a mixed Co phase that is consistent with TPR data.

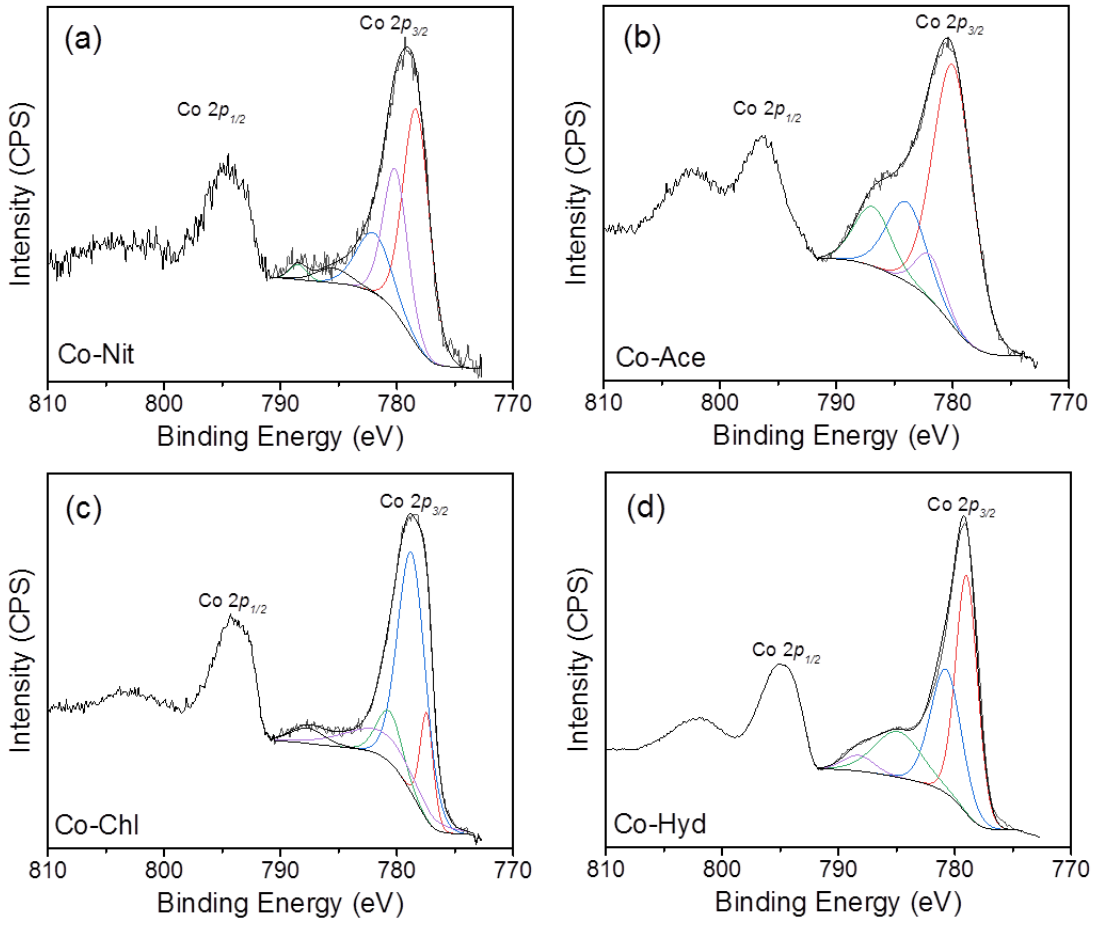

Figure 4.4. XPS spectra of silica-supported cobalt catalysts prepared from different precursors: (a) $Co(NO_3)_2$, (b) $Co(C_2H_3O_2)_2$, (c) $CoCl_2$, and (d) $Co(OH)_2$.

4.3.2 FTS Activity and selectivity

4.3.2.1 Activity of SiO_2-supported cobalt catalyst

The catalytic activity and product selectivity of the different catalysts are summarized in Table 4.2. It is apparent from the results that catalytic activity is strongly affected by the type of Co precursor used during synthesis. CO conversions of Co-Nit and Co-Hyd are 56% and 60% respectively, which are significantly higher than those of Co-Ace (12%) and Co-Chl (7%); these results are consistent with the catalytic behavior predicted by TPR results (Figure 4.3) that show low-reduction temperature and high reducibility for Co-Nit and Co-Hyd (Table 4.1). CO conversions are consistent with TOF for all catalysts (Table 4.1) and activity decreases in the following order: Co-Hyd > Co-Nit > Co-Ace > Co-Chl. The relatively low activity of the Co-Ace catalyst is ascribed to the inappropriate electronic states that limit the dissociative adsorption of the CO molecule as explained by Bae et al. [12]. Also, residual Cl^- present in a Co-Chl catalyst has been shown to act as a catalyst poison that lowers the CO conversion [22]. Our XPS analysis (survey scan and atomic composition in Figure C4.3 and Table C6.3) confirm the presence of Cl^- impurities in the Co-Chl catalyst.

FTS reaction rate and CO conversion increase in the following order: Co-Chl < Co-Ace < Co-Nit < Co-Hyd. A strong correlation exists between catalytic activity and reducibility obtained from TPR. The higher activity of Co-Nit and Co-Hyd in comparison to Co-Ace and Co-Chl is directly related to the reducibility of the catalysts. Plots of CO conversion as a function of time on stream (TOS) in Figure 4.5 show that the catalysts exhibit different stability patterns during FTS. Co-Nit shows good stability as CO conversion only dropped from 65% to 55% and the total CO conversion decreased by only 15%. Co-Hyd also shows high CO conversion (> 50%), but with a profile that suggests gradual catalyst deactivation with time or requires longer time to

reach steady state. The CO conversion of Co-Ace dropped from 36% to 12% before reaching a steady state; the total loss of activity in terms of CO conversion is as high as 67%, which may be attributed, in part, to the low catalyst stability. Similarly, Co-Chl shows poor CO conversion and stability as it drops from 17% to 6%. In the case of Co-Chl, the low CO conversion could be due to the blockage of the active site by the residual Cl^- ion [22].

Table 4.2. Catalytic activity and product selectivity of fresh silica-supported cobalt catalysts derived from different precursors obtained at steady state after 15h on stream.

Catalysts	Name	CO Conversion (%)	Hydrocarbon selectivity (%)			FTS Reaction Rate (g HC/h*g-cat.)	TOF (10^{-4} s^{-1})	α
			CH_4	C2-C4	C5+			
$Co(NO_3)_2/SiO_2$	Co-Nit	56	27	17	56	0.53	10.4	0.75
$Co(C_2H_4O_2)_2/SiO_2$	Co-Ace	12	46	2	52	0.11	1.9	0.91
$CoCl_2/SiO_2$	Co-Chl	7	52	1	47	0.06	1.5	0.88
$Co(OH)_2/SiO_2$	Co-Hyd	60	38	3	59	0.56	12.7	0.86

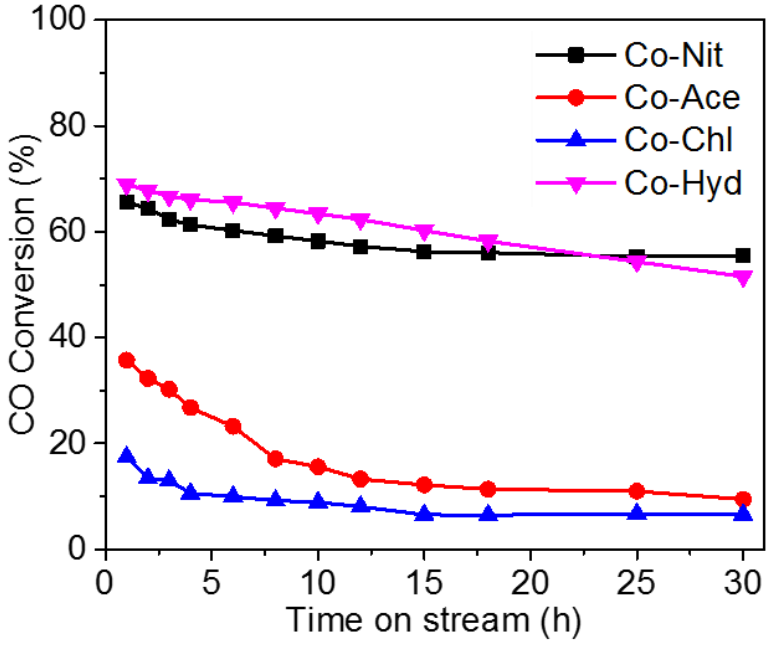

Figure 4.5. CO conversion as a function of time on stream using silica-supported cobalt catalysts prepared from different precursors [($Co(NO_3)_2$, $Co(C_2H_3O_2)_2$, $CoCl_2$, and $Co(OH)_2$].

XRD patterns of used Co-Nit, Co-Ace, Co-Chl, and Co-Hyd catalysts are shown in Figure 4.6. Because of the use of crystalline silicon carbide (SiC) as a diluent, the highly intense peaks from the SiC mask most of the Co_3O_4 peaks in the samples. Nevertheless, diffraction peaks at 2θ of 41.7° and 45.3° reveal the presence of cobalt carbide (Co_2C) in Co-Ace, Co-Chl, and Co-Hyd catalysts [54, 55]. Among the mechanisms proposed to explain catalyst deactivation in FTS reaction, formation of Co_2C is frequently invoked [9, 56-58]. We, therefore, speculate that the deactivation observed in Co-Ace, Co-Chl, and Co-Hyd catalysts may be associated with the formation of Co_2C. However, the absence of Co_2C in the XRD pattern of Co-Nit after reaction demonstrates its good stability.

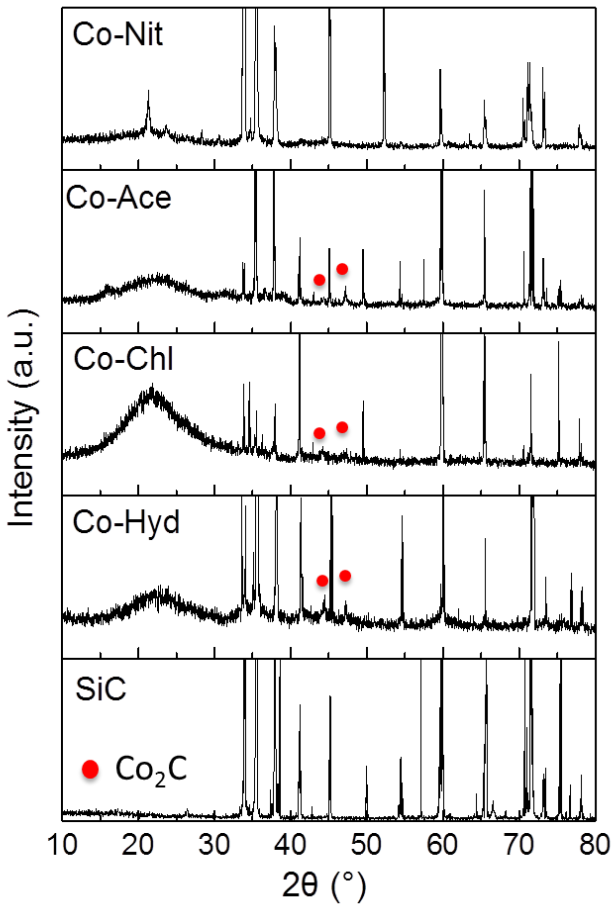

Figure 4.6. XRD patterns of used silica-supported cobalt catalysts prepared from different precursors [($Co(NO_3)_2$, $Co(C_2H_3O_2)_2$, $CoCl_2$, and $Co(OH)_2$].

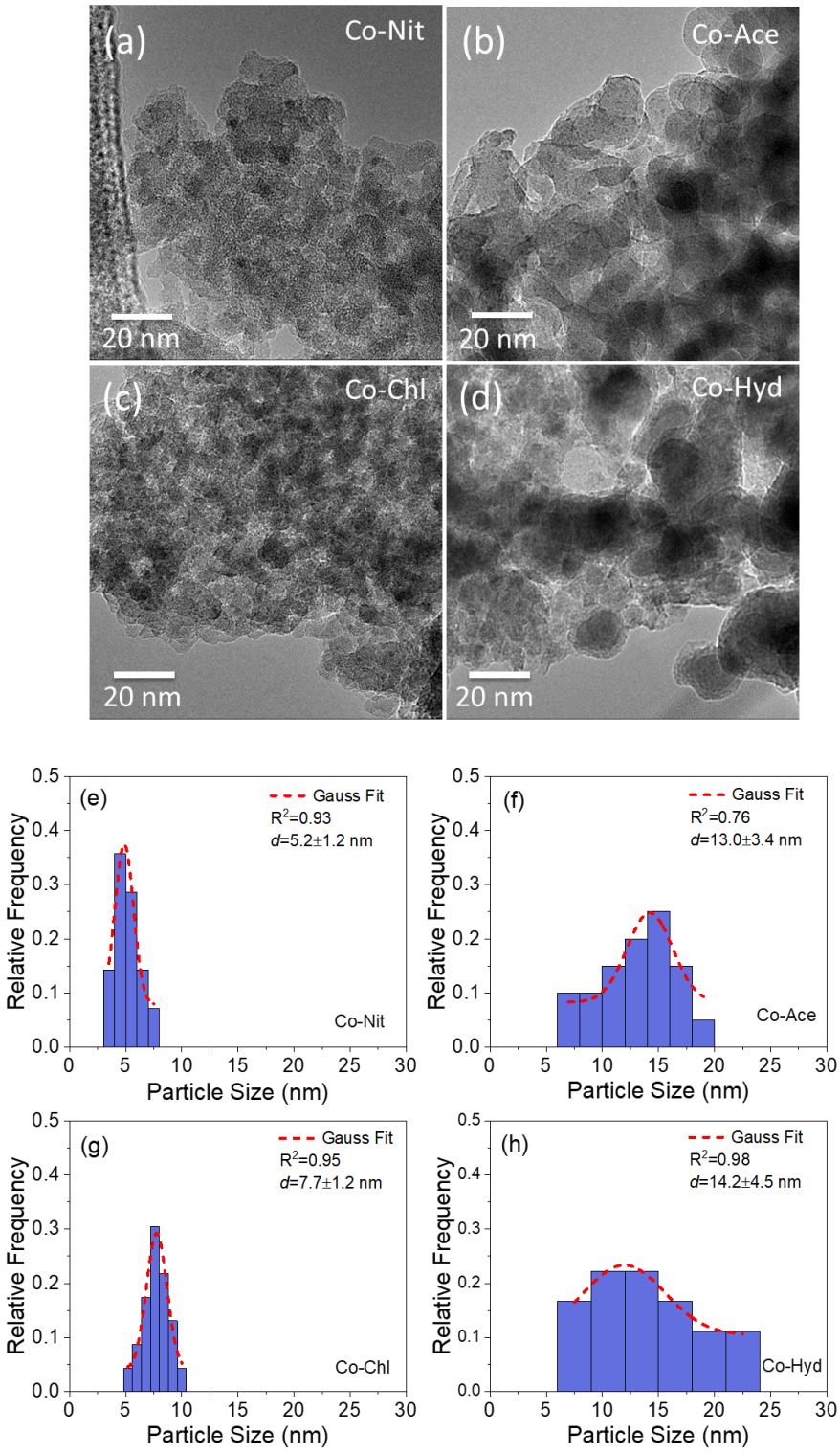

Figure 4.7. High-magnification TEM images and corresponding histograms of PSDs with Gaussian analysis fitting of used silica-supported catalysts prepared from different precursors: $Co(NO_3)_2$ (a and e), $Co(C_2H_3O_2)_2$ (b and f), $CoCl_2$ (c and g), and $Co(OH)_2$ (d and h).

The high-magnification TEM images of the different catalysts after FTS reaction for 30 h are shown in Figure 4.7. By comparing the catalyst features of fresh (Figure 4.2) and used catalysts (Figure 4.7), it is apparent a distinct change occurs in the catalyst morphology, evidenced in the broadening of PSD of catalysts and an increase in average particle size. This could be due to sintering induced by oxidation–reduction cycles on the catalyst surface as reported by Jacob et al. [59]. The average particle sizes of Co-Nit, Co-Ace, Co-Chl, and Co-Hyd (before and after FTS) are (3.7 and 5.2 nm), (3.0 and 13.0 nm), (2.8 and 7.7 nm), and (4.0 and 14.2 nm), respectively. While there is evidence of sintering in the catalysts, it decreases in the following order: Co-Ace > Co-Hyd > Co-Chl > Co-Nit. The stable activity during FTS reaction for Co-Nit is attributed to the low sintering observed. The loss of activity for Co-Ace, Co-Chl, and Co-Hyd may be due to a combined effect of sintering and formation of Co_2C.

4.3.2.2 Selectivity of SiO_2-supported cobalt catalysts

Table 4.2 shows the hydrocarbon product distributions of catalysts prepared from different precursors. An additional summary showing the selectivity of the fresh catalysts for the same CO conversion is presented in Table C6.4. After the reaction reached steady state, the C5+ selectivity increases in the following order: Co-Chl < Co-Ace < Co-Nit < Co-Hyd. Variations of hydrocarbon distribution with TOS (C5+ selectivity) as a function of TOS for the catalysts are shown in Figure 4.8. The catalysts exhibit different stability patterns. In particular, Co-Nit, Co-Hyd, and Co-Chl exhibit relatively lower C5+ selectivity loss of 20%, 23%, and 24% after 30h on stream, respectively; in contrast, Co-Ace shows a decrease of 32%. Detailed C5+ product distributions for reactions on all catalysts are summarized in Figure 4.9. C5+ product distributions for Co-Ace, Co-Chl and Co-Hyd mainly belong to the diesel range (C_{12}-C_{17}). In stark contrast to Co-Nit, product distribution observed for Co-Hyd is centered on C_{15}, indicating

that Co-Hyd-catalyzed FTS reaction is selective for long-chain hydrocarbons. Co-Nit shows a relatively flat distribution, which means more hydrocarbon products are in the gasoline range and the average molecular weight is lower than the other three catalysts. These results are consistent with the chain-growth probability

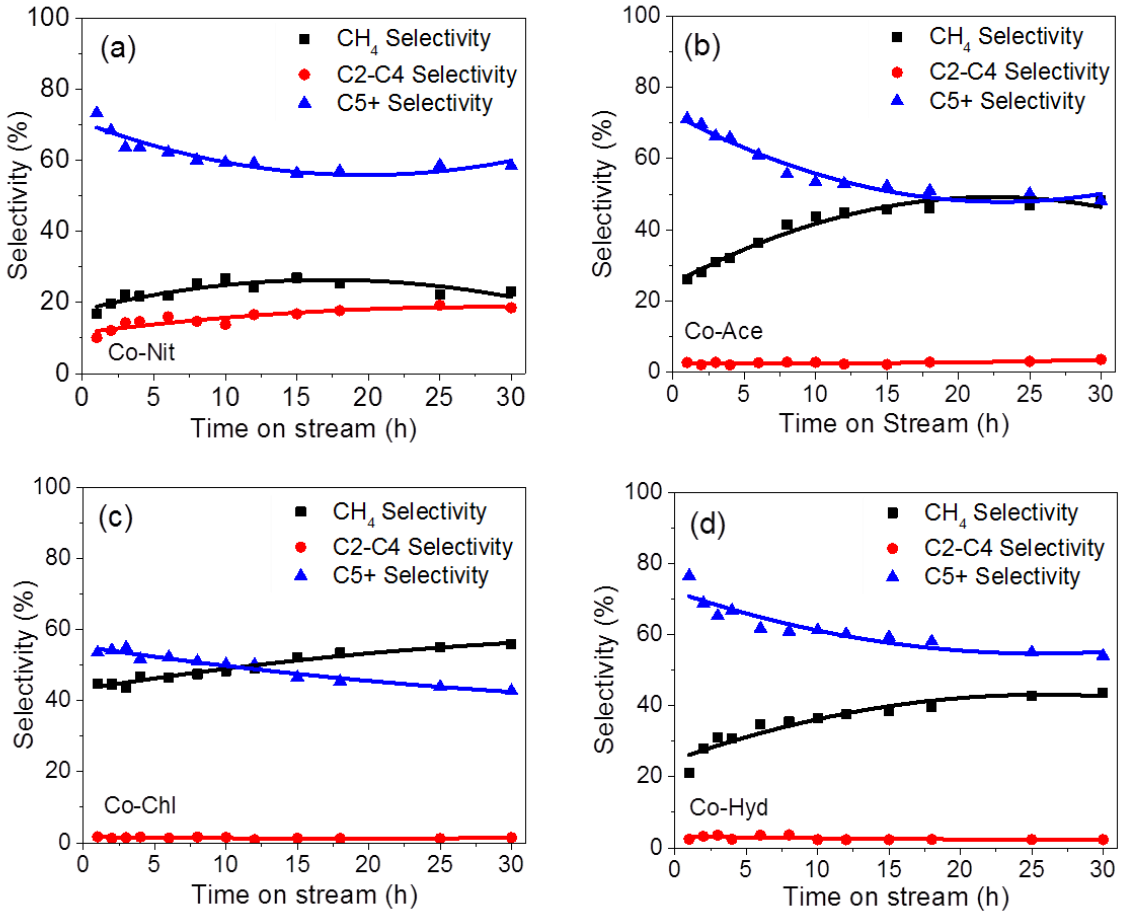

Figure 4.8. Hydrocarbon selectivity of silica-supported cobalt catalysts prepared by different Co precursors: (a) $Co(NO_3)_2$, (b) $Co(C_2H_3O_2)_2$, (c) $CoCl_2$, and (d) $Co(OH)_2$.

(α) value. The α value of Co-Nit is 0.75, which is lower than those of Co-Ace, Co-Chl, and Co-Hyd with α values of 0.91, 0.88, and 0.86, respectively. Usually, the relationship between C5+ selectivity and α follows a positive trend [3]; however, due to the support confinement effect, their correlation with selectivity may vary [38]. In our case, a positive trend exists between α and

C5+ selectivity as catalysts with α > 0.8 exhibit high selectivity for long-chain hydrocarbons in the diesel range. Although both Co-Nit and Co-Hyd exhibit relatively high and stable C5+ selectivity, Co-Nit is selective for a broad distribution of hydrocarbons that include low- and high-cut hydrocarbons while Co-Hyd is mainly selective for a high cut. The hydrocarbon selectivity of Co-Hyd is consistent with the high-chain growth probability and may be due to its high reducibility and relatively larger particles that are formed. Co-Ace that seem to experience similar growth in particles also exhibit high α and selectivity for high-cut hydrocarbons. In addition, hydroxyl groups have been reported to enhance dispersion, reducibility and catalytic activity of Co [40]. We, therefore, hypothesize that the hydroxyl groups in Co-Hyd provide an environment that supports improved FTS performance.

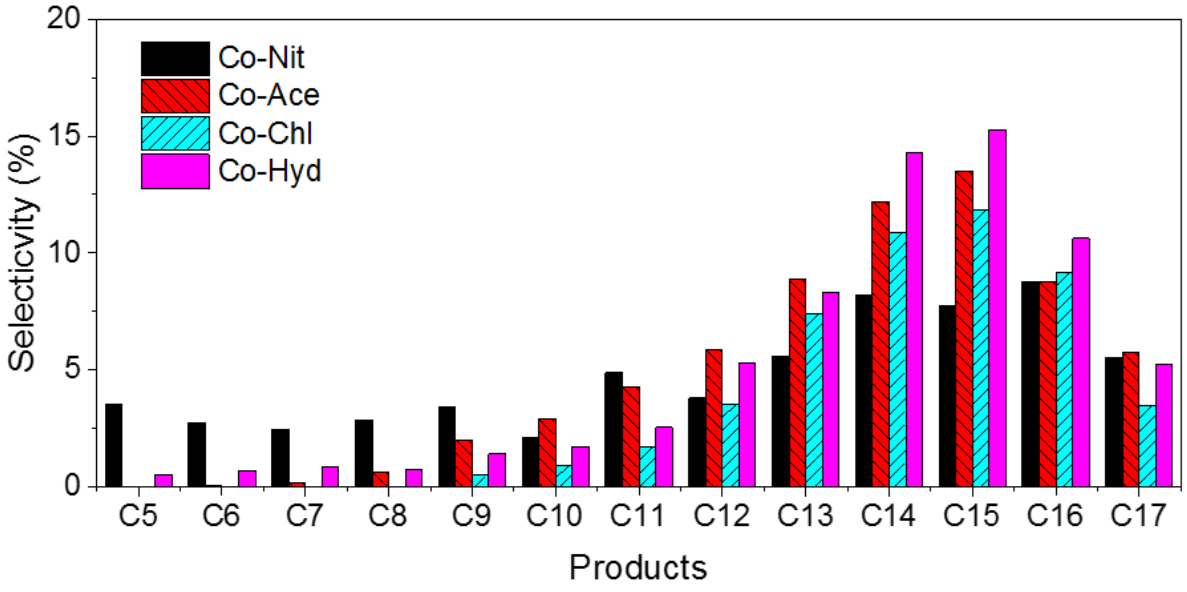

Figure 4.9. C5+ products distributions for silica-supported cobalt catalysts prepared from different cobalt precursors [($Co(NO_3)_2$, $Co(C_2H_3O_2)_2$, $CoCl_2$, and $Co(OH)_2$].

4.3.2.3 X-ray absorption near-edge structure and near-edge X-ray absorption fine structure

Fresh and used Co-Nit and Co-Hyd catalysts were studied using XAS to better understand the influence of precursor and catalytic properties on the local Co structure. Co-Nit and Co-Hyd were primarily examined because they exhibit the highest catalytic activity (Figure 4.5) and C5+ selectivity accompanied by different catalyst stability (Figure 4.8) and C5+ product distribution (Figure 4.9). Co K-edge XANES spectrum has three main regions: pre-edge (A), corresponding to the typically forbidden s→d transition; absorption edge (B); and a post-edge region (C). In the fresh Co-Nit catalyst (Figure 4.10a, black line), the pre-edge feature at 7708 eV and corresponding XANES features are strongly indicative of nanoscale Co_3O_4, consistent with our characterization results from XPS, XRD, and TPR. After FTS reaction, a significant shift in E_0 to lower energy can be observed (Figure 4.10b, red line) along with an overall change in XANES profile. The shift to lower E_0 is indicative of a lower overall oxidation state, strongly suggesting formation of CoO and perhaps zerovalent Co. This is consistent with our observations that the conventional $Co(NO_3)_2$ precursor yields mainly Co_3O_4; the formation of CoO after FTS, as shown in the XANES results, may be due to air oxidation of the reduced sample. The fresh Co-Hyd XANES spectrum (Figure 4.10a, blue line) exhibits an E_0 more similar to Co^{2+} materials and profile that would suggest the formation of both α and β $Co(OH)_2$ [60]. Interestingly, upon undergoing FT reactions for extended periods, the change in local structure is minimal. Near-identical XANES profiles are observed (Figure 4.10a, magenta line), which exhibit only a slight broadening of the pre-edge feature and shift to lower E_0. This likely indicates only some of the Co atoms are zerovalent after the reaction. For reference, the XANES of a Co foil (Figure 4.10a, green line) is also shown, indicating an overall lack of predominate hcp Co in any of the samples.

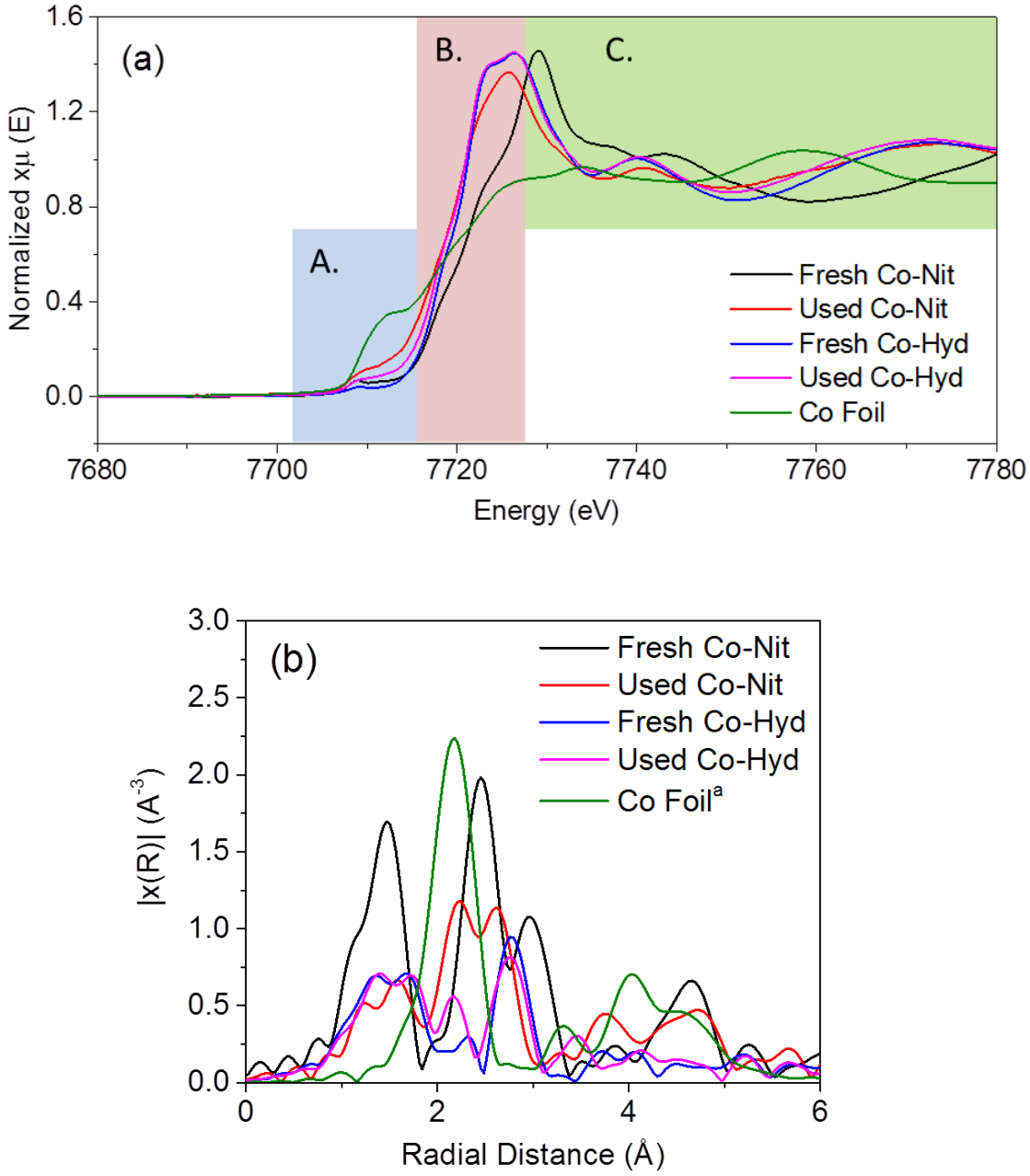

Figure 4.10. XANES profiles of freshly prepared and used catalysts prepared from $Co(NO_3)_2$ and $Co(OH)_2$ precursors (a). EXAFS profiles of freshly prepared and used catalysts prepared from $Co(NO_3)_2$ and $Co(OH)_2$ precursors (b). ([a] intensity of Co foil was reduced by 50%)

The Co K-edge EXAFS are obtained after the data are converted into *k*-space (with k^2-weighting) and Fourier transformed from 2.8 to 13.2 $Å^{-1}$ (Figure 4.10b). Overall, the EXAFS

data re-affirm our observations from XANES corresponding to the structural changes observed before and after FTS reaction. Note that all plotted EXAFS distances have not been phase-corrected as presented (~ 0.4 Å). The fresh Co-Nit EXAFS (Figure 4.10b, black line) exhibits peaks at 1.47, 2.46, and 2.96 Å, corresponding to the first Co-O coordination sphere and subsequent Co-Co coordination spheres. After FTS reaction, the Co-Nit EXAFS changes drastically (Figure 4.10b red), with a highest-magnitude feature aligning with metallic Co at 2.22 Å (Figure 4.10b green). In addition, major EXAFS peaks positioned at 1.58 and 2.61 Å correspond to Co-O and Co-Co coordination spheres, respectively, in CoO. The Co-hyd samples, both before and after FTS reaction (Figure 4.10b, blue and magenta lines, respectively), exhibit similar features in EXAFS that correspond to a hydroxide structure. The major difference is the appearance of an additional peak in the post-reaction sample at 2.22 Å corresponding to metallic Co.

To quantify these results, EXAFS modeling was performed as described in the experimental section. All fitting results can be found in the Supplementary Information, and local Co coordination numbers (CNs) and nearest neighbor distances (NNDs) are summarized in Tables B6.5 and B6.6, respectively. For fresh Co-Nit, three scattering paths were implemented to produce a quality fit using Co-O and Co-Co scattering paths from Co_3O_4 and an additional Co-O path that more closely resembles a theoretical CoOOH structure [33]. Note this inclusion simply matches features found in the EXAFS but is likely a contribution from either nanoscale distortions within the Co_3O_4, substrate interactions, and/or backscattering from nitrate left over from the synthesis. The reduced Co-Co CN of 6.61 ± 0.98 from bulk (12.0) coupled with the modestly high-second Co-O coordination sphere (CN = 4.28 ± 0.67 and NND of 2.87 ± 0.01 Å) suggest local nanoscale distortion within these materials. After undergoing FTS, the Co-Nit

sample was best modelled using Co-O and Co-Co scattering paths from CoO, and Co-Co from hcp metallic Co, which reaffirms our XANES observations. CoO local CNs are again significantly reduced from bulk values as expected, while a Co-Co CN of 2.23 ± 0.29 for hcp Co suggests very small clusters of metallic Co (< 50 atoms) [61]. Co reduction is expected to occur under FTS conditions and our results suggest that re-oxidation after exposure to air is somewhat impeded via stabilization by neighboring hydroxyl groups, thereby preserving the reduced Co clusters. Co synthesized from $Co(OH)_2$ precursor demonstrated markedly different EXAFS modelling results. As synthesized, CNs from the first Co-O and Co-Co coordination spheres are slightly reduced from bulk values (4.99 ± 0.74 and 4.96 ± 0.71 vs 6.0 for each, respectively), which is common in nanoscale materials. A second Co-O is needed for a sufficient quality fit, with a CN of 4.81 ± 0.97 and an NND of 2.83 ± 0.04 Å. After reaction, a small amount of metallic Co can be modeled, with a Co-Co CN of 1.31 ± 0.25 and a NND of 2.50 ± 0.01 Å. Interestingly, the Co-Hyd is maintained with similar values for Co-O, and Co-Co CNs and NNDs. Unlike Co-Nit, hydroxyl groups from the precursor in Co-Hyd prevents oxidation of metal Co to CoO after FTS reaction. Overall, XANES and EXAFS data confirm the superior structural stability of Co-Hyd and possible presence of hydroxyl groups even after reaction. We conclude that the hydroxyl groups create a basic environment in Co-Hyd that support stability of Co.

A schematic representation catalyst evolution during H_2 reduction and FTS reaction processes is depicted in Figure 4.11. The catalysts are all composed of a small fraction of large particles and a large fraction of small particles. The consistent trend in the average particle size of catalyst obtained from low-magnification TEM and XRD is further evidence of the inability of XRD to detect a large fraction of the small particles (Table C6.2). Complete reduction of Co-Nit

occurs during activation and the catalyst shows mild sintering and high stability, which accounts for its high resistance to deactivation. Co-Ace has a small fraction of Co_3O_4 particles and a large fraction of CoO particles; and as shown by Girardon et al. [20], Co-Ace has a high tendency to form partially reduced Co-Si oxide. Moreover, severe sintering is observed after FTS reaction for Co-Ace. The presence of Cl^- in Co-Chl results in blockage of active sites and prevents the interaction of H_2 with catalysts; therefore, only a small fraction of a Co-Chl catalyst can be reduced. Co-Hyd exhibits high reducibility that is comparable to Co-Nit and the highest TOF, although Co-Hyd appears more prone to sintering during FTS than Co-Nit.

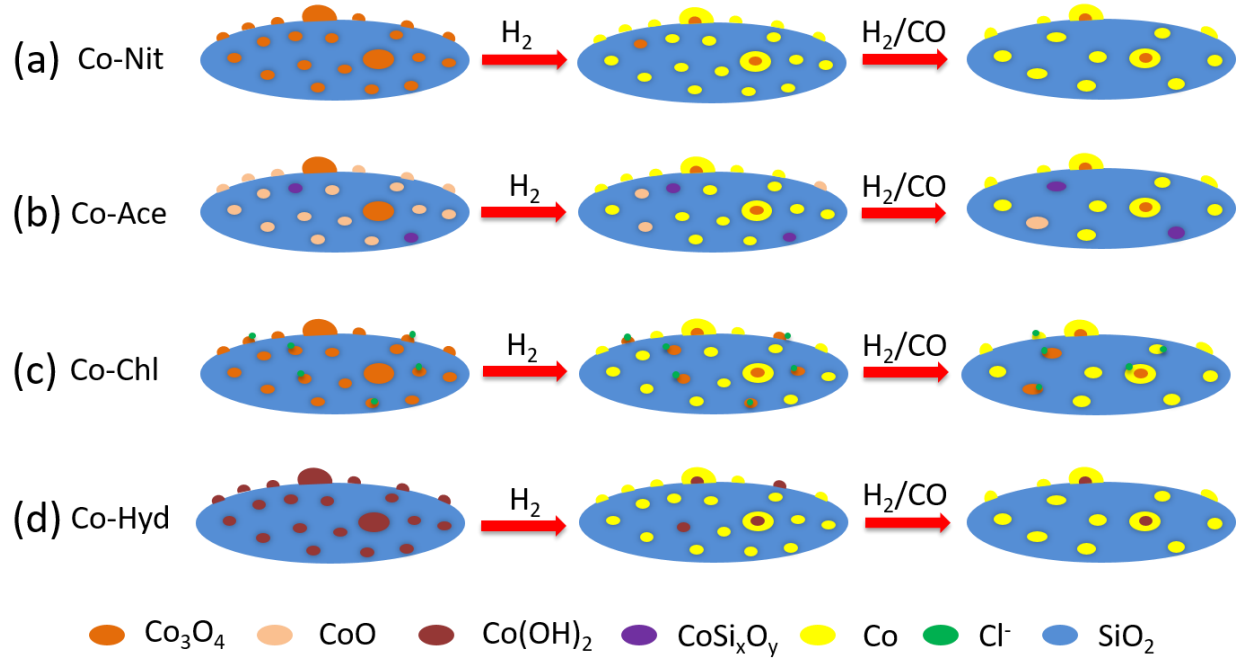

Figure 4.11. Schematic illustration of the evolution of cobalt catalysts derived from different precursors during FTS process (activation and reaction).

4.4 Conclusions

A series of SiO_2-supported Co catalysts derived from different precursors via incipient wetness impregnation has been studied. The resulting catalyst particles have sizes in a narrow

range of 3 – 4 nm and are well-dispersed on SiO_2 support. A catalyst derived from $Co(OH)_2$ (Co-Hyd) shows relatively higher surface area that is ascribed to the unique synthesis method that eliminates the calcination step. The Co phase of the fresh catalyst is sensitive to the Co precursor used during synthesis. A strong correlation between reducibility and catalytic performance is observed; catalysts derived from $Co(NO_3)_2$ and $Co(OH)_2$ show higher reducibility (hydrogen consumption >90%) and catalytic performance (CO conversion ad C5+ selectivity) than those from $Co(C_2H_3O_2)_2$ and $CoCl_2$. Sintering and the presence of Co_2C is observed for Co-Ace, Co-Chl, and Co-Hyd, catalysts that experience different degrees of deactivation. C5+ selectivity increases in the following order: Co-Chl < Co-Ace < Co-Nit < Co-Hyd. C5+ product distributions for Co-Ace, Co-Chl, and Co-Hyd mainly fall in the diesel range (C_{12}-C_{17}), and that for Co-Hyd is centered on C_{15} and is selective for long-chain hydrocarbons; whereas Co-Nit shows a relatively flat distribution, which means more hydrocarbon products are in the gasoline range. XANES and EXAFS data confirm superior structural stability of Co-Hyd and presence of hydroxyl groups even after reaction. Unlike Co-Nit, the hydroxyl groups create a basic environment in Co-Hyd that may support high TOF and C5+ selectivity.

4.5 References

[1] M.E. Dry, The fischer–tropsch process: 1950–2000, *Catalysis Today*, 71 (2002) 227-241.

[2] H. Jahangiri, J. Bennett, P. Mahjoubi, K. Wilson, S. Gu, A review of advanced catalyst development for Fischer–Tropsch synthesis of hydrocarbons from biomass derived syn-gas, *Catalysis Science & Technology*, 4 (2014) 2210-2229.

[3] A.Y. Khodakov, W. Chu, P. Fongarland, Advances in the development of novel cobalt Fischer− Tropsch catalysts for synthesis of long-chain hydrocarbons and clean fuels, *Chemical Reviews*, 107 (2007) 1692-1744.

[4] Q. Zhang, W. Deng, Y. Wang, Recent advances in understanding the key catalyst factors for Fischer-Tropsch synthesis, *Journal of Energy Chemistry*, 22 (2013) 27-38.

[5] J.M. González-Carballo, F.J. Pérez-Alonso, F.J. García-García, M. Ojeda, J.L.G. Fierro, S. Rojas, In-situ study of the promotional effect of chlorine on the Fischer–Tropsch synthesis with Ru/Al_2O_3, *Journal of Catalysis*, 332 (2015) 177-186.

[6] E. de Smit, B.M. Weckhuysen, The renaissance of iron-based Fischer–Tropsch synthesis: on the multifaceted catalyst deactivation behaviour, *Chemical Society Reviews*, 37 (2008) 2758-2781.

[7] A.R. de la Osa, A. de Lucas, L. Sánchez-Silva, J. Díaz-Maroto, J.L. Valverde, P. Sánchez, Performing the best composition of supported Co/SiC catalyst for selective FTS diesel production, *Fuel*, 95 (2012) 587-598.

[8] A.n. Martínez, C. López, F. Márquez, I. Díaz, Fischer–Tropsch synthesis of hydrocarbons over mesoporous Co/SBA-15 catalysts: the influence of metal loading, cobalt precursor, and promoters, *Journal of Catalysis*, 220 (2003) 486-499.

[9] G.L. Bezemer, J.H. Bitter, H.P. Kuipers, H. Oosterbeek, J.E. Holewijn, X. Xu, F. Kapteijn,

A.J. van Dillen, K.P. de Jong, Cobalt particle size effects in the Fischer− Tropsch reaction studied with carbon nanofiber supported catalysts, *Journal of the American Chemical Society*, 128 (2006) 3956-3964.

[10] J.-S. Girardon, E. Quinet, A. Griboval-Constant, P. Chernavskii, L. Gengembre, A. Khodakov, Cobalt dispersion, reducibility, and surface sites in promoted silica-supported Fischer–Tropsch catalysts, *Journal of Catalysis*, 248 (2007) 143-157.

[11] Y. Wang, Z. Tao, B. Wu, J. Xu, C. Huo, K. Li, H. Chen, Y. Yang, Y. Li, Effect of metal precursors on the performance of Pt/ZSM-22 catalysts for n-hexadecane hydroisomerization, *Journal of Catalysis*, 322 (2015) 1-13.

[12] J.W. Bae, S.-M. Kim, S.-H. Kang, K.V. Chary, Y.-J. Lee, H.-J. Kim, K.-W. Jun, Effect of support and cobalt precursors on the activity of $Co/AlPO_4$ catalysts in Fischer–Tropsch synthesis, *Journal of Molecular Catalysis A: Chemical*, 311 (2009) 7-16.

[13] H.M. Torres Galvis, A.C.J. Koeken, J.H. Bitter, T. Davidian, M. Ruitenbeek, A.I. Dugulan, K.P. de Jong, Effect of precursor on the catalytic performance of supported iron catalysts for the Fischer–Tropsch synthesis of lower olefins, *Catalysis Today*, 215 (2013) 95-102.

[14] O. Clause, M. Kermarec, L. Bonneviot, F. Villain, M. Che, Nickel(II) ion-support interactions as a function of preparation method of silica-supported nickel materials, *Journal of the American Chemical Society*, 114 (1992) 4709-4717.

[15] H. Almkhelfe, X. Li, P. Thapa, K.L. Hohn, P.B. Amama, Carbon nanotube-supported catalysts prepared by a modified photo-Fenton process for Fischer–Tropsch synthesis, *Journal of Catalysis*, 361 (2018) 278-289.

[16] L.G.A. van de Water, G.L. Bezemer, J.A. Bergwerff, M. Versluijs-Helder, B.M. Weckhuysen, K.P. de Jong, Spatially resolved UV–vis microspectroscopy on the preparation of

alumina-supported Co Fischer–Tropsch catalysts: Linking activity to Co distribution and speciation, *Journal of Catalysis*, 242 (2006) 287-298.

[17] E. Iglesia, Design, synthesis, and use of cobalt-based Fischer-Tropsch synthesis catalysts, *Applied Catalysis A: General*, 161 (1997) 59-78.

[18] E. Iglesia, S.L. Soled, R.A. Fiato, Fischer-Tropsch synthesis on cobalt and ruthenium. Metal dispersion and support effects on reaction rate and selectivity, *Journal of Catalysis*, 137 (1992) 212-224.

[19] E. Iglesia, S.C. Reyes, R.J. Madon, S.L. Soled, Selectivity Control and Catalyst Design in the Fischer-Tropsch Synthesis: Sites, Pellets, and Reactors, in: D.D. Eley, H. Pines, P.B. Weisz (Eds.) Advances in Catalysis, Academic Press1993, pp. 221-302.

[20] J.-S. Girardon, A.S. Lermontov, L. Gengembre, P.A. Chernavskii, A. Griboval-Constant, A.Y. Khodakov, Effect of cobalt precursor and pretreatment conditions on the structure and catalytic performance of cobalt silica-supported Fischer–Tropsch catalysts, *Journal of Catalysis*, 230 (2005) 339-352.

[21] L. Zhang, L. Dong, W. Yu, L. Liu, Y. Deng, B. Liu, H. Wan, F. Gao, K. Sun, L. Dong, Effect of cobalt precursors on the dispersion, reduction, and CO oxidation of CoOx/γ-Al_2O_3 catalysts calcined in N2, *Journal of Colloid and Interface Science*, 355 (2011) 464-471.

[22] J. Panpranot, S. Kaewkun, P. Praserthdam, J.G. Goodwin, Effect of cobalt precursors on the dispersion of cobalt on MCM-41, *Catalysis Letters*, 91 (2003) 95-102.

[23] X. Li, F. Bai, H. Su, Cobalt-based catalysts derived from cobalt carbonyl clusters for Fischer-Tropsch synthesis, *Chinese Journal of Catalysis*, 35 (2014) 342-350.

[24] S. Sun, N. Tsubaki, K. Fujimoto, The reaction performances and characterization of Fischer–Tropsch synthesis Co/SiO2 catalysts prepared from mixed cobalt salts, *Applied*

Catalysis A: General, 202 (2000) 121-131.

[25] N. Tsubaki, S. Sun, K. Fujimoto, Different Functions of the Noble Metals Added to Cobalt Catalysts for Fischer–Tropsch Synthesis, *Journal of Catalysis*, 199 (2001) 236-246.

[26] J.S. Girardon, E. Quinet, A. Griboval-Constant, P.A. Chernavskii, L. Gengembre, A.Y. Khodakov, Cobalt dispersion, reducibility, and surface sites in promoted silica-supported Fischer–Tropsch catalysts, *Journal of Catalysis*, 248 (2007) 143-157.

[27] Z. Huang, Y. Zhao, Y. Song, Y. Li, G. Wu, H. Tang, J. Zhao, Study on the oxidation process of cobalt hydroxide to cobalt oxides at low temperatures, *RSC Advances*, 6 (2016) 80059-80064.

[28] J. Yang, H. Liu, W.N. Martens, R.L. Frost, Synthesis and characterization of cobalt hydroxide, cobalt oxyhydroxide, and cobalt oxide nanodiscs, *The Journal of Physical Chemistry C*, 114 (2009) 111-119.

[29] S. Brunauer, P.H. Emmett, E. Teller, Adsorption of Gases in Multimolecular Layers, *Journal of the American Chemical Society*, 60 (1938) 309-319.

[30] E.P. Barrett, L.G. Joyner, P.P. Halenda, The Determination of Pore Volume and Area Distributions in Porous Substances. I. Computations from Nitrogen Isotherms, *Journal of the American Chemical Society*, 73 (1951) 373-380.

[31] H.P. Klug, L.E. Alexander, X-ray diffraction procedures, (1954).

[32] B. Ravel, M. Newville, ATHENA, ARTEMIS, HEPHAESTUS: Data Analysis for X-Ray Absorption Spectroscopy Using IFEFFIT, *Journal of Synchrotron Radiation*, 12 (2005) 537-541.

[33] A. Jain, S.P. Ong, G. Hautier, W. Chen, W.D. Richards, S. Dacek, S. Cholia, D. Gunter, D. Skinner, G. Ceder, K.A. Persson, Commentary: The Materials Project: A materials genome approach to accelerating materials innovation, *APL Materials*, 1 (2013) 011002.

[34] R.J. Berger, J. Pérez-Ramírez, F. Kapteijn, J.A. Moulijn, Catalyst performance testing:

Radial and axial dispersion related to dilution in fixed-bed laboratory reactors, *Applied Catalysis A: General*, 227 (2002) 321-333.

[35] R. Friedel, R. Anderson, Composition of synthetic liquid fuels. I. product distribution and analysis of C5—C8 paraffin isomers from cobalt catalyst1, *Journal of the American Chemical Society*, 72 (1950) 1212-1215.

[36] G. Jacobs, T.K. Das, Y. Zhang, J. Li, G. Racoillet, B.H. Davis, Fischer–Tropsch synthesis: support, loading, and promoter effects on the reducibility of cobalt catalysts, *Applied Catalysis A: General*, 233 (2002) 263-281.

[37] Ø. Borg, S. Eri, E.A. Blekkan, S. Storsæter, H. Wigum, E. Rytter, A. Holmen, Fischer–Tropsch synthesis over γ-alumina-supported cobalt catalysts: effect of support variables, *Journal of Catalysis*, 248 (2007) 89-100.

[38] A.Y. Khodakov, A. Griboval-Constant, R. Bechara, V.L. Zholobenko, Pore size effects in Fischer Tropsch synthesis over cobalt-supported mesoporous silicas, *Journal of Catalysis*, 206 (2002) 230-241.

[39] Y. Lu, P. Zhou, J. Han, F. Yu, Fischer–Tropsch synthesis of liquid hydrocarbons over mesoporous SBA-15 supported cobalt catalysts, *RSC Advances*, 5 (2015) 59792-59803.

[40] A.Y. Khodakov, W. Chu, P. Fongarland, Advances in the Development of Novel Cobalt Fischer−Tropsch Catalysts for Synthesis of Long-Chain Hydrocarbons and Clean Fuels, *Chemical Reviews*, 107 (2007) 1692-1744.

[41] Ø. Borg, P.D. Dietzel, A.I. Spjelkavik, E.Z. Tveten, J.C. Walmsley, S. Diplas, S. Eri, A. Holmen, E. Rytter, Fischer–Tropsch synthesis: cobalt particle size and support effects on intrinsic activity and product distribution, *Journal of Catalysis*, 259 (2008) 161-164.

[42] G. Prieto, A. Martínez, P. Concepción, R. Moreno-Tost, Cobalt particle size effects in

Fischer–Tropsch synthesis: structural and in situ spectroscopic characterisation on reverse micelle-synthesised Co/ITQ-2 model catalysts, *Journal of Catalysis*, 266 (2009) 129-144.

[43] E. Lira, C.M. López, F. Oropeza, M. Bartolini, J. Alvarez, M. Goldwasser, F.L. Linares, J.-F. Lamonier, M.J.P. Zurita, HMS mesoporous silica as cobalt support for the Fischer–Tropsch synthesis: pretreatment, cobalt loading and particle size effects, *Journal of Molecular Catalysis A: Chemical*, 281 (2008) 146-153.

[44] P. Concepción, C. López, A. Martínez, V.F. Puntes, Characterization and catalytic properties of cobalt supported on delaminated ITQ-6 and ITQ-2 zeolites for the Fischer–Tropsch synthesis reaction, *Journal of Catalysis*, 228 (2004) 321-332.

[45] P.A. Chernavskii, A.Y. Khodakov, G.V. Pankina, J.S. Girardon, E. Quinet, In situ characterization of the genesis of cobalt metal particles in silica-supported Fischer-Tropsch catalysts using Foner magnetic method, *Applied Catalysis A: General*, 306 (2006) 108-119.

[46] J.S. Girardon, A. Constant-Griboval, L. Gengembre, P.A. Chernavskii, A.Y. Khodakov, Optimization of the pretreatment procedure in the design of cobalt silica supported Fischer–Tropsch catalysts, *Catalysis Today*, 106 (2005) 161-165.

[47] A.Y. Khodakov, J. Lynch, D. Bazin, B. Rebours, N. Zanier, B. Moisson, P. Chaumette, Reducibility of cobalt species in silica-supported Fischer–Tropsch catalysts, *Journal of Catalysis*, 168 (1997) 16-25.

[48] M.C. Biesinger, B.P. Payne, A.P. Grosvenor, L.W.M. Lau, A.R. Gerson, R.S.C. Smart, Resolving surface chemical states in XPS analysis of first row transition metals, oxides and hydroxides: Cr, Mn, Fe, Co and Ni, *Applied Surface Science*, 257 (2011) 2717-2730.

[49] S. Karimi, A. Tavasoli, Y. Mortazavi, A. Karimi, Cobalt supported on Graphene – A promising novel Fischer–Tropsch synthesis catalyst, *Applied Catalysis A: General*, 499 (2015)

188-196.

[50] B.-A.F. Kengne, A.M. Alayat, G. Luo, A.G. McDonald, J. Brown, H. Smotherman, D.N. McIlroy, Preparation, surface characterization and performance of a Fischer-Tropsch catalyst of cobalt supported on silica nanosprings, *Applied Surface Science*, 359 (2015) 508-514.

[51] S.C. Petitto, E.M. Marsh, G.A. Carson, M.A. Langell, Cobalt oxide surface chemistry: The interaction of CoO(100), Co3O4(110) and Co3O4(111) with oxygen and water, *Journal of Molecular Catalysis A: Chemical*, 281 (2008) 49-58.

[52] Y. Yang, L. Jia, B. Hou, D. Li, J. Wang, Y. Sun, The Correlation of Interfacial Interaction and Catalytic Performance of N-Doped Mesoporous Carbon Supported Cobalt Nanoparticles for Fischer–Tropsch Synthesis, *The Journal of Physical Chemistry C*, 118 (2014) 268-277.

[53] M. Davari, S. Karimi, A. Tavasoli, A. Karimi, Enhancement of activity, selectivity and stability of CNTs-supported cobalt catalyst in Fischer–Tropsch via CNTs functionalization, *Applied Catalysis A: General*, 485 (2014) 133-142.

[54] D. Moodley, J. Van de Loosdrecht, A. Saib, M. Overett, A. Datye, J. Niemantsverdriet, Carbon deposition as a deactivation mechanism of cobalt-based Fischer–Tropsch synthesis catalysts under realistic conditions, *Applied Catalysis A: General*, 354 (2009) 102-110.

[55] A. Tavasoli, R.M.M. Abbaslou, A.K. Dalai, Deactivation behavior of ruthenium promoted Co/γ-Al_2O_3 catalysts in Fischer–Tropsch synthesis, *Applied Catalysis A: General*, 346 (2008) 58-64.

[56] J. Xiong, Y. Ding, T. Wang, L. Yan, W. Chen, H. Zhu, Y. Lu, The formation of Co_2C species in activated carbon supported cobalt-based catalysts and its impact on Fischer–Tropsch reaction, *Catalysis Letters*, 102 (2005) 265-269.

[57] O. Ducreux, J. Lynch, B. Rebours, M. Roy, P. Chaumette, In situ characterisation of cobalt

based Fischer-Tropsch catalysts: A new approach to the active phase, *Studies in Surface Science and Catalysis*, (1998) 125-130.

[58] V. GRUVER, Z. XIAODONG, J. ENGMAN, H.J. ROBOTA, S.L. SUIB, M. POLVEREJAN, Deactivation of a Fischer-Tropsch catalyst through the formation of cobalt carbide under laboratory slurry reactor conditions, *Preprints-American Chemical Society. Division of Petroleum Chemistry*, 49 (2004) 192-194.

[59] G. Jacobs, P.M. Patterson, T.K. Das, M. Luo, B.H. Davis, Fischer–Tropsch synthesis: effect of water on Co/Al2O3 catalysts and XAFS characterization of reoxidation phenomena, *Applied Catalysis A: General*, 270 (2004) 65-76.

[60] R. Ma, Z. Liu, K. Takada, K. Fukuda, Y. Ebina, Y. Bando, T. Sasaki, Tetrahedral Co(II) Coordination in α-Type Cobalt Hydroxide: Rietveld Refinement and X-ray Absorption Spectroscopy, *Inorganic Chemistry*, 45 (2006) 3964-3969.

[61] A.I. Frenkel, A. Yevick, C. Cooper, R. Vasic, Modeling the Structure and Composition of Nanoparticles by Extended X-Ray Absorption Fine-Structure Spectroscopy, *Annual Review of Analytical Chemistry*, 4 (2011) 23-39.

Chapter 5 - Conclusions

In this dissertation, two main projects on rational catalyst design have been discussed. The first project involves establishing interrelationships between substrate properties and CNT carpet growth behavior while the second involves the development of efficient FT catalysts. In the first project, several different materials [stainless steel, $MgAl_2O_4$ (100, 110, 111) and MgO] were studied as a catalyst supporting layer for CNT carpet growth. In the second project, FT catalysts prepared from different cobalt precursors were investigated in order to synthesize well-dispersed Co catalyst (free of agglomeration) for efficient FTS process. Based on the results and discussions, the main conclusions are summarized below:

- Ion beam bombardment is able to convert an "inactive" substrate into an "active" substrate for CNT carpet growth. The role of ion beam bombardment is demonstrated as a powerful tool for transforming a crystalline surface into an amorphous surface, creating surface porosity that improves catalytic activity and enhances CNT growth. Using this process, we have converted an "inactive" $MgAl_2O_4$ spinel substrate into an "active" substrate for CNT carpet growth. We also decreased the Al_xO_y layer thickness required for CNTs grown on stainless steel to ~5nm.
- Different phases of $MgAl_2O_4$ substrates show different CNT growth behaviors due to their different surface chemistries and surface energies. $MgAl_2O_4$ (111) is the best supporting layer for Fe catalyst among the $MgAl_2O_4$ spinel substrates due to its high surface basicity and relatively high surface energy. Our newly developed carbon feedstock (FTS-GP) outperforms C_2H_4 (conventional precursor)

for CNT carpet growth. FTS-GP enhances CNT growth rate and extends catalyst lifetime.

- Catalytic performance is sensitive to the catalyst preparation method and type of catalyst precursor. Our study reveals the type of Co precursor used during synthesis has significant effects on catalyst dispersion, size, crystalline phase, reducibility, stability, and FTS performance. In particular, catalysts derived from $Co(NO_3)_2$ and $Co(OH)_2$ show superior CO conversion, turnover frequency and catalyst lifetime than those from $Co(C_2H_3O_2)_2$ and $CoCl_2$, which is consistent with their reducibility. XANES and EXAFS results show the presence of hydroxyl groups on Co-Hyd catalyst and the hydroxyl groups is believed to create a basic environment in Co-Hyd to support high CO conversion, C5+ selectivity, turnover frequency and catalyst lifetime.

This dissertation provides a deeper understanding into the effect of substrate properties on CNT carpet growth. The study provides further proof of the high efficiency of FTS-GP in CNT growth and a pathway for mass production of CNT arrays via CCVD. The investigation on the effect of cobalt precursor on performance of FTS reaction has not only resulted in the development of an FT catalyst derived from a green precursor, but also a deeper understanding of the role of catalyst precursor and pretreatment. This knowledge is expected to provide a new paradigm for designing stable catalysts that will not be subjected to synthesis steps that induce sintering and formation of hard-to-reduce oxides.

Chapter 6 - Future Work

Recommendations for future work are as follow:

- Use different substrates to grow high quality, dense and ultra-long SWCNTs.
- Investigate ways to modify surface basicity or surface energy of substrates to achieve better CNT carpet growth.
- Use different catalysts or promoters (Cu, Ru and Pt) to grow CNTs on novel substrate ($MgAl_2O_4$, ZrO_2, TiO_2 etc.).
- Add promoters to catalysts prepared using $Co(OH)_2$ precursor to investigate its effect on FTS performance.

Appendix A - Supplementary Information for Chapter 2

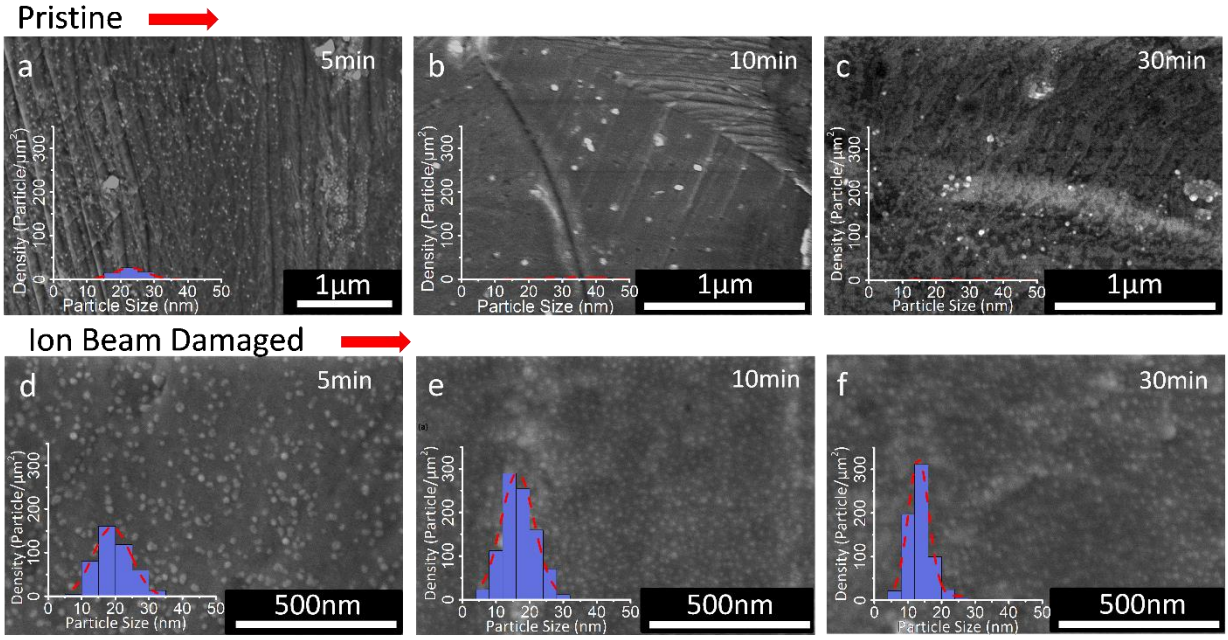

Figure A2. 1 Catalyst evolution on Pristine-5 and Damaged-5 during annealing. Upper panels: SEM images of catalyst particles on Pristine-5 (with inserts of PSDs) after annealing for 5 min (a), 10 min (b), and 30 min (c). Bottom panels: SEM images of catalyst particles on Damaged-5 (with inserts of PSD) after annealing for 5 min (d), 10 min (e), and 30 min (f).

Appendix B - Supplementary Information for Chapter 3

B.1 Introduction

Owing to its outstanding properties such as good mechanical performance, high thermal conductivity, high electrical conductivity and high hydrophobicity [1-8] carbon nanotubes (CNTs) has been used in various applications including energy storage [9, 10], thermally conductive materials [11, 12], catalysis [13, 14], sensing devices [15, 16] and omniphobic surfaces [1, 17, 18]. However, in many applications, CNTs alone cannot fulfil all the requirements. Therefore, the combination of CNTs with another material is required.

For some applications like energy storage, heat dissipation and hydrophobic surface, CNTs have to have very good contact with the neighboring material. The best way to produce CNTs that have good contacts with other materials is to have CNTs grown on them directly on them. Domingues et al. [19, 20] created some unique structures with cavities on Si wafers to increase the hydrophobicity of the surface. It is expected that by growing a thin layer of CNT carpets on these cavities, it can enhance their hydrophobicity even more.

Yttria-stabilized ZrO_2 [denoted as ZrO_2 (Y)] is an important ceramic material. Due to its high thermal stability, large energy band gap and relatively high strength [21-23], it has been used in many applications such as solid oxide fuel cells (SOFC) [24], dental application [25], sensing device [26] and membranes [27]. However, not many studies have used ZrO_2 (Y) to grow CNTs especially SWCNTs.

In this chapter, we focus on implementing growth of CNTs on substrates that are generally difficult to grow on to extend the application of CNTs. First, we used ion beam bombardment to modify the surface as discussed in Chapter 3. Next a thin layer of Al_xO_y is deposited on the substrate as discussed in Chapter 2. These modification steps enable the growth

of a thin layer of CNTs on simple cavity (SC), reentrant cavity (RC), doubly reentrant cavity (DRC) silica substrates. The main goal of this work is to increase the hydrophobicity of the three silica substrates with different cavities while maintaining its original properties by depositing a very thin layer (1-2 μm) of CNTs. Also, an unconventional metal oxide substrate, ZrO_2 (Y) has been used to grow CNTs. Interestingly, we discovered that unlike other conventional substrates, SWCNTs can be grown on this substrate even with a 2 nm-thick Fe catalyst.

B.2 Experimental

B.2.1 SC, RC and DRC Silica Preparation

The three different silica substrates (SC, RC, and DRC) used as catalyst supports were modified by ion beam bombardment in an ion beam sputter deposition and etching system (IBS/e) obtained from South Bay Technology Inc. The substrates were placed directly opposite the Ar ion source (spot size ~3 mm) with adjustments made to ensure the beam line is perpendicular to the substrate. Ion beam damage was conducted for 10 min at an acceleration voltage of 6 kV and a beam current of 3.5 mA. The total ion dose was calculated to be 1.46×10^{20} cm^{-2} [28]. Thereafter, damaged substrates were deposited with different thickness (0, 5 10 nm) of Al_xO_y films. A thin Fe catalyst film with a nominal thickness of 1 nm was then deposited on Al_xO_y layer. The Al_xO_y and Fe films were sequentially deposited on substrates in the IBS/e without exposure to air.

B.2.2 ZrO_2 (Y) Substrate Preparation

ZrO_2 (Y) substrate was ion beam-damaged following the same procedure as SC, RC and DRC silica substrates for 10 min. Then, pristine and ion beam-damaged substrates were both deposited with a 2 nm-thick Fe film using an ion beam sputtering system.

B.2.3 CNT Growth

The growth equipment is described in Chapters 2 and 3. SC, RC and DRC silica substrates with deposited Fe catalysts were heated to 750 °C at a rate of 50 °C/min in flowing Ar 1000 standard cubic centimeters per minute (sccm). Then, the catalyst prereduction was conducted by flowing 250 sccm H_2 and 250 sccm Ar for 10 min. Thereafter, CNT growth was initiated by switching to the growth gas mixture containing 25 sccm FTS-GP and 250 sccm Ar. At the end of growth, the samples were rapidly cooled in H_2, followed by slow cooling to room temperature in 700 sccm Ar.

For ZrO_2 (Y) sample, the catalyst samples were heated to 750 °C at a rate of 50 °C/min in flowing Ar 1000 sccm. Then, the catalyst prereduction was conducted by flowing 250 sccm H_2 and 250 sccm Ar. Thereafter, CNT growth was initiated by switching to the growth gas mixture containing 100 sccm FTS-GP and 1000 sccm Ar. At the end of growth, the samples were rapidly cooled in H_2, followed by slow cooling to room temperature in 700 sccm Ar.

B.2.4 Characterization

The morphology of the growth products and growth behavior of the different catalyst substrates were characterized with a Hitachi S5200 field-emission scanning electron microscope (SEM) operated at 5 kV. Optical microscope was also used to measure CNT carpet height.

Raman spectra of growth products were collected at multiple spots from the samples using a Renishaw inVia Raman microscope with a 532-nm laser as the excitation source. XRR measurements were conducted on a Rigaku-Smartlab X-ray diffractometer equipped with a Cu Kα (λ = 0.154 nm) radiation source using a slit collimation in air.

B.3 Results and Discussion

B.3.1 SC, RC and DRC Silica Substrates

In this work, we have studied three silica-based substrates with different cavities. The cavities were classified based on their profiles as simple cavities (SCs), reentrant cavities (RCs), and doubly reentrant cavities (DRCs). Their structures are shown in Figure B3.1. The diameter of each cavity is 200 μm. The main difference is their cavity edge.

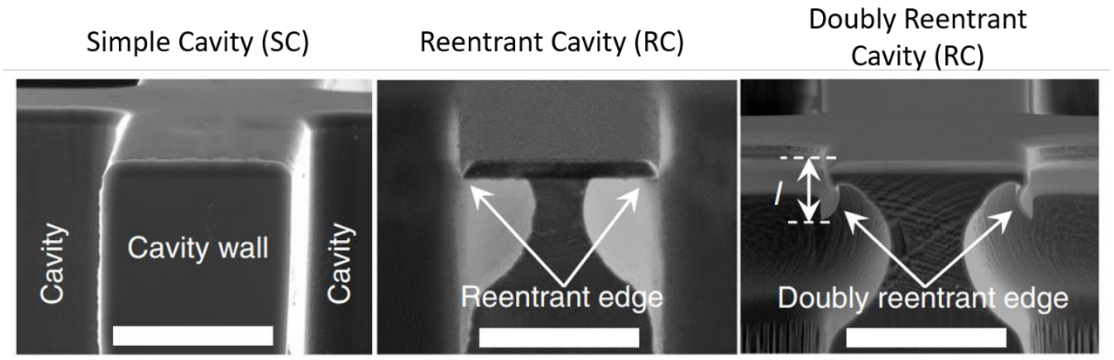

Figure B3. 1 SEM images of cross section of SC, RC and DRC silica substrates.

We have conducted experiments using substrates after ion beam bombardment and with different Al_xO_y layer thicknesses as shown in following:

1) 0 nm Al_xO_y without ion beam bombardment.
2) 5 nm Al_xO_y without ion beam bombardment.

3) 5 nm Al_xO_y with ion beam bombardment.

4) 10 nm Al_xO_y without ion beam bombardment.

Figure B3.2a shows SEM images of CNTs formed after CCVD on ion beam-bombarded sample with 10 nm-thick Al_xO_y . Clearly, we can see a thick CNT carpet grown on each substrate. Such good growth was expected because the surface properties of substrates are dominated by a thick Al_xO_y layer (10 nm) and Al_xO_y is one of the best substrates for CNT growth. Figure B3.2b exhibits SEM images of CNTs formed after CCVD on the sample with 5 nm-thick Al_xO_y without ion beam bombardment. Unlike the samples with a 10 nm-thick Al_xO_y without exposure to ion beam bombardment, these series of substrates have no CNTs grown on them. The reason for lack of CNT growth on substrates is that the pristine SC, RC and DRC silica substrates are not suitable for direct CNT growth and the impact of Al_xO_y on them is too weak to support CNT growth. Therefore, the surface modification of substrates via ion beam bombardment was used as we explained in previous chapter. Figure B3.2c shows SEM images of CNTs formed after CCVD on ion beam-bombarded samples with 5 nm-thick Al_xO_y. It shows CNT carpet was grown on each substrate. Consequently, the combination of ion beam bombardment and deposition of a thin layer of Al_xO_y is able to convert an “inactive” substrate into an “active” substrate, which is consistent with the conclusion in Chapter 2. It is reasonable that the CNT growth rate on a 10 nm-thick Al_xO_y-deposited sample without exposure to ion beam bombardment are very close, since the thick Al_xO_y has essentially masked the properties of the pristine substrate. The growth behavior has been dominated by the properties of Al_xO_y layer. However, the ion beam-bombarded sample with 5 nm-thick Al_xO_y shows a different growth behavior. The growth rate of RC and DRC is more than that of SC samples by a factor of 2. We attribute this difference to the unique structure of the cavity in each substrate.

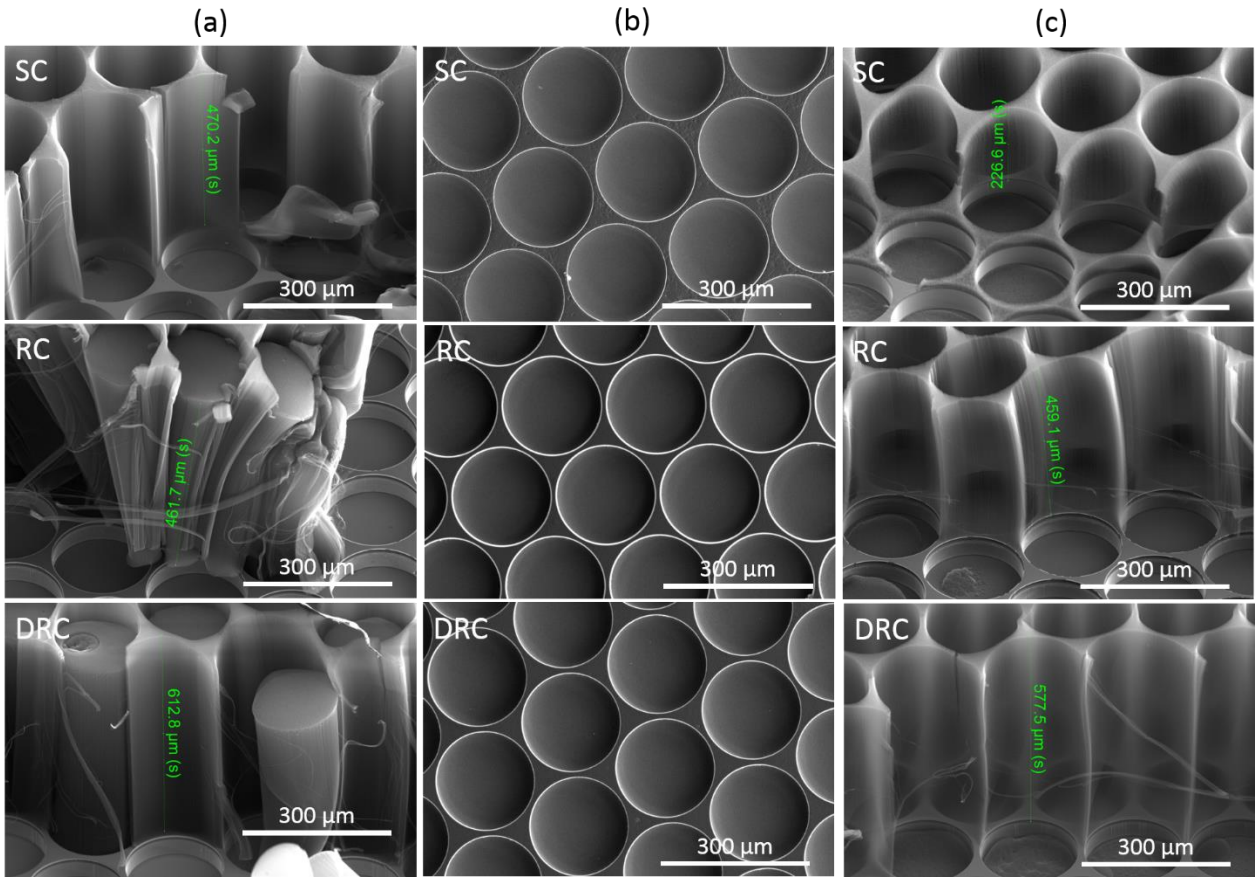

Figure B3. 2 SEM images of CNTs formed after 30 min of CCVD on 10 nm Al_xO_y without ion beam bombardment (a), 5 nm Al_xO_y without ion beam bombardment (b) and 5 nm Al_xO_y with ion beam bombardment (c).

The Raman spectra of CNTs formed on the surface of each substrate with different Al_xO_y barrier layer thicknesses after a CCVD process are shown in Figure B3.3. Although we do not see CNT carpet grown on 5 nm-thick Al_xO_y-deposited sample without ion beam bombardment, we still acquired Raman spectra from them and the presence of CNTs on the substrates was confirmed. Having compared Figures B3.3 a and b, we can see the quality of CNTs formed on 5 nm-thick Al_xO_y–deposited sample without exposure to ion beam bombardment are much lower than a similar sample with a 10 nm-thick Al_xO_y. From Figures B3.3 a and c, we can conclude

that the quality of CNTs grow on 10 nm Al_xO_y-deposited sample without exposure to ion beam bombardment and an ion beam-bombarded sample with 5 nm Al_xO_y are essentially the same.

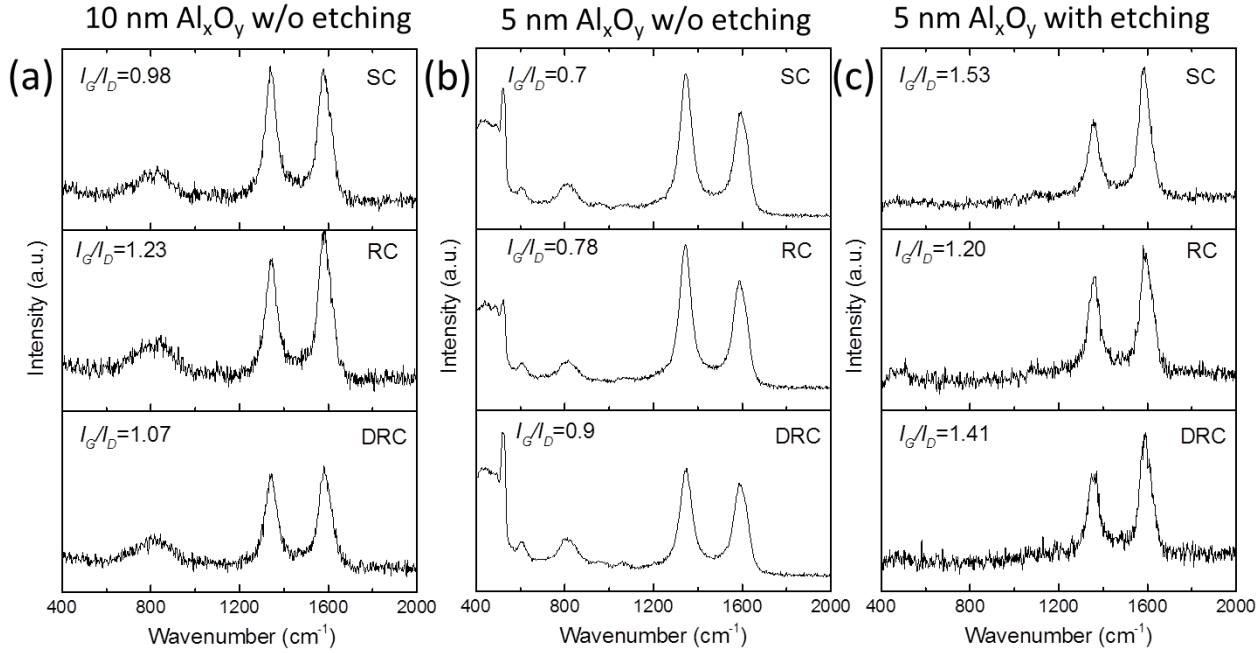

Figure B3. 3 Raman spectra of CNTs formed on 10 nm-thick Al_xO_y without ion beam bombardment (a), 5 nm-thick Al_xO_y without ion beam bombardment (b) and 5 nm-thick Al_xO_y with ion beam bombardment (c).

As the goal of this work is to grow a very thin layer (1-2 μm) of CNTs on SC, RC, and DRC silica substrates while maintaining its original properties, we used ion beam-bombarded substrates with 5 nm-thick Al_xO_y as our standard sample to grow CNTs. We adjusted the growth time to achieve a thin layer of CNTs. After conducting the experiment of growing CNTs for 1 min, we have achieved our main objective. The results are shown in Figure B3.4. The CNT carpet thickness is around the required range.

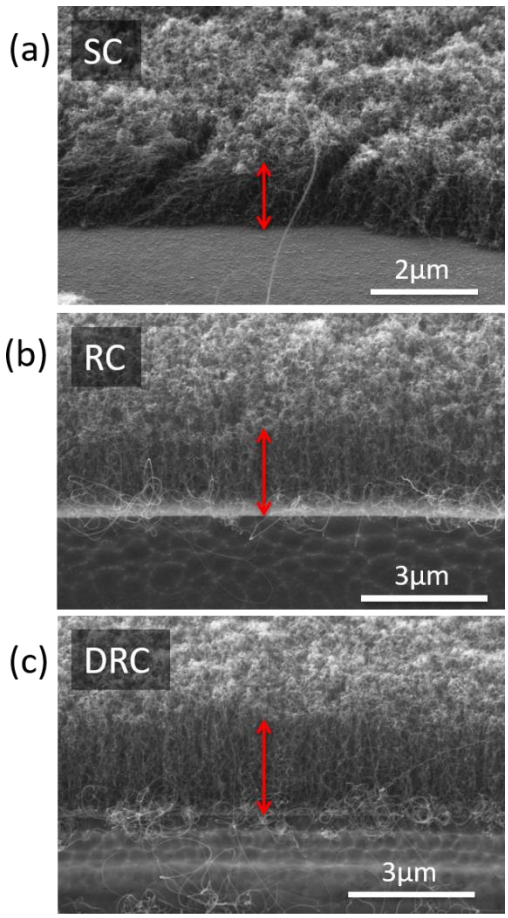

Figure B3. 4 SEM images of CNTs formed during CCVD for 10 min on ion beam-bombarded substrates with 5 nm Al_xO_y.

B.3.2 ZrO_2 (Y) Substrate

Figure B3.5 shows the SEM images of CNTs grown on a ZrO_2 (Y) substrate. We cannot observe thick CNT carpets formed on the substrate surface. Therefore, it may not be a good substrate for mass production of CNTs. However, we do observe denser CNTs formed on ion beam-damaged substrates, which one more time proves that this surface engineering process is able to enhance CNT growth as been discussed in Chapter 3. The Raman spectra of Figure B3.6 indicates CNTs formed on a ZrO_2 (Y) substrate contains SWCNTs. This is counter intuitive in CNT growth as CNT diameter is a function of catalyst diameter and a 2 nm-thick catalyst usually yields MWCNTs [29-31]. However, with a ZrO_2 (Y) substrate, we were still able to produce SWCNTs using a thick catalyst layer. The mechanism behind this phenomenon is worth unravelling. Moreover, ion beam-damaged sample show a decreased CNT quality as opposed to the pristine sample. This may be caused by the faster growth rate that increases the possibility of generating more defects during growth.

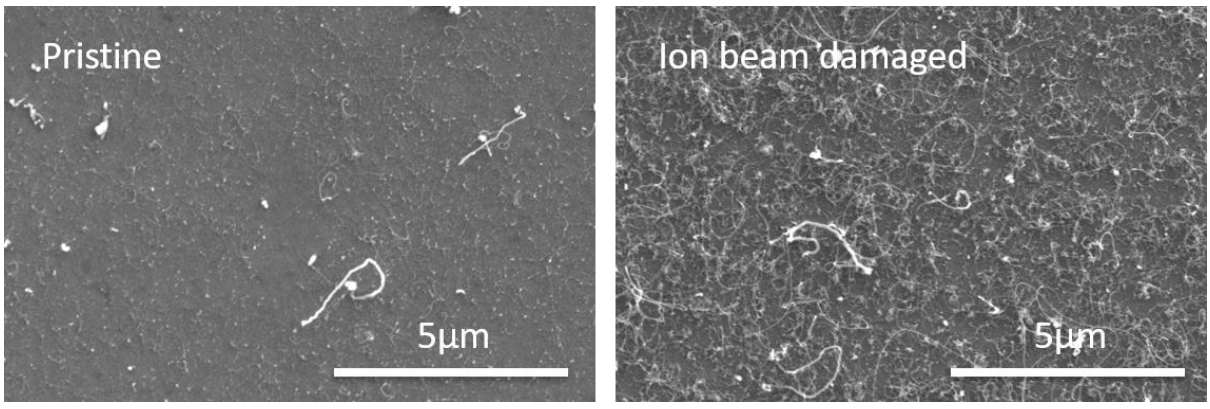

Figure B3. 5 SEM images of CNTs formed after CCVD for 10 min on pristine and ion beam-damaged ZrO_2 (Y) substrates.

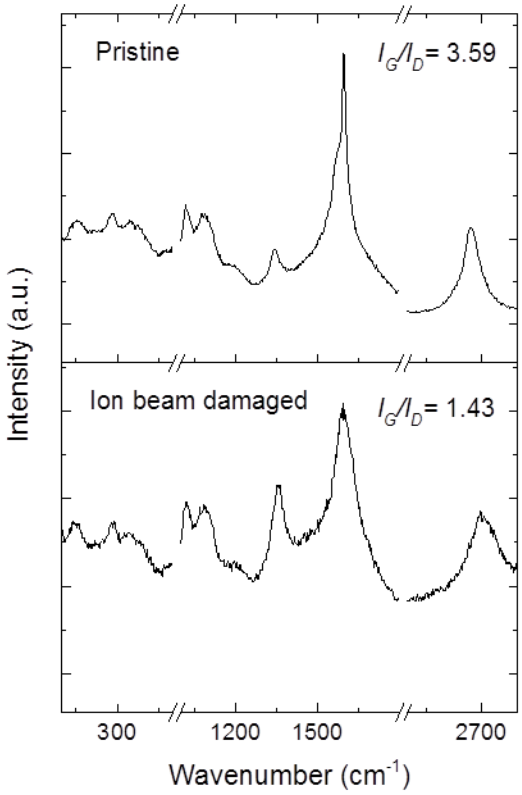

Figure B3. 6 Raman spectra of CNTs formed after 10 min of CCVD on pristine and ion beam-damaged ZrO_2 (Y) substrates.

B.4 Conclusion

From the results discussed above, we can conclude that CNT growth was not observed from catalysts deposited directly on substrates with cavities without deposition of Al_xO_y barrier layer because these substrates are not suitable for CNT growth. The use of ion beam bombardment to modify the surface of SC, RC and DRC silica substrates reduced the Al_xO_y barrier layer thickness required for CNT growth to 5 nm. We have achieved precise control of CNT carpet height by adjusting growth time. ZrO_2 (Y) substrate has been discovered to support SWCNT growth even with a thick catalyst layer.

B.5 References

[1] M. Bottini, S. Bruckner, K. Nika, N. Bottini, S. Bellucci, A. Magrini, A. Bergamaschi, T. Mustelin, Multi-walled carbon nanotubes induce T lymphocyte apoptosis, *Toxicology Letters*, 160 (2006) 121-126.

[2] Y.C. Hong, D.H. Shin, S.C. Cho, H.S. Uhm, Surface transformation of carbon nanotube powder into super-hydrophobic and measurement of wettability, *Chemical Physics Letters*, 427 (2006) 390-393.

[3] V.N. Popov, Carbon nanotubes: properties and application, *Materials Science and Engineering: R: Reports*, 43 (2004) 61-102.

[4] S. Berber, Y.-K. Kwon, D. Tománek, Unusually high thermal conductivity of carbon nanotubes, *Physical Review Letters*, 84 (2000) 4613.

[5] R.H. Baughman, A.A. Zakhidov, W.A. De Heer, Carbon nanotubes--the route toward applications, *Science*, 297 (2002) 787-792.

[6] B.J. Landi, M.J. Ganter, C.D. Cress, R.A. DiLeo, R.P. Raffaelle, Carbon nanotubes for lithium ion batteries, *Energy & Environmental Science*, 2 (2009) 638-654.

[7] E. Pop, D. Mann, Q. Wang, K. Goodson, H. Dai, Thermal conductance of an individual single-wall carbon nanotube above room temperature, *Nano Letters*, 6 (2006) 96-100.

[8] S.J. Tans, M.H. Devoret, H. Dai, A. Thess, R.E. Smalley, L. Geerligs, C. Dekker, Individual single-wall carbon nanotubes as quantum wires, *Nature*, 386 (1997) 474.

[9] W. Wang, P.N. Kumta, Nanostructured hybrid silicon/carbon nanotube heterostructures: reversible high-capacity lithium-ion anodes, *ACS Nano*, 4 (2010) 2233-2241.

[10] C.L. Pint, N.W. Nicholas, S. Xu, Z. Sun, J.M. Tour, H.K. Schmidt, R.G. Gordon, R.H. Hauge, Three dimensional solid-state supercapacitors from aligned single-walled carbon

nanotube array templates, *Carbon*, 49 (2011) 4890-4897.

[11] H. Chen, M. Chen, J. Di, G. Xu, H. Li, Q. Li, Architecting three-dimensional networks in carbon nanotube buckypapers for thermal interface materials, *The Journal of Physical Chemistry C*, 116 (2012) 3903-3909.

[12] B.A. Cola, J. Xu, C. Cheng, X. Xu, T.S. Fisher, H. Hu, Photoacoustic characterization of carbon nanotube array thermal interfaces, *Journal of Applied Physics*, 101 (2007) 054313.

[13] W. Li, C. Liang, W. Zhou, J. Qiu, Z. Zhou, G. Sun, Q. Xin, Preparation and characterization of multiwalled carbon nanotube-supported platinum for cathode catalysts of direct methanol fuel cells, *The Journal of Physical Chemistry B*, 107 (2003) 6292-6299.

[14] K. Gong, F. Du, Z. Xia, M. Durstock, L. Dai, Nitrogen-doped carbon nanotube arrays with high electrocatalytic activity for oxygen reduction, *Science*, 323 (2009) 760-764.

[15] K. Saetia, J.M. Schnorr, M.M. Mannarino, S.Y. Kim, G.C. Rutledge, T.M. Swager, P.T. Hammond, Spray‐Layer‐by‐Layer Carbon Nanotube/Electrospun Fiber Electrodes for Flexible Chemiresistive Sensor Applications, *Advanced Functional Materials*, 24 (2014) 492-502.

[16] E. Llobet, Gas sensors using carbon nanomaterials: A review, *Sensors and Actuators B: Chemical*, 179 (2013) 32-45.

[17] B. Corry, Designing carbon nanotube membranes for efficient water desalination, *The Journal of Physical Chemistry B*, 112 (2008) 1427-1434.

[18] L. Dumée, V. Germain, K. Sears, J. Schütz, N. Finn, M. Duke, S. Cerneaux, D. Cornu, S. Gray, Enhanced durability and hydrophobicity of carbon nanotube bucky paper membranes in membrane distillation, *Journal of Membrane Science*, 376 (2011) 241-246.

[19] E.M. Domingues, S. Arunachalam, H. Mishra, Doubly reentrant cavities prevent

catastrophic wetting transitions on intrinsically wetting surfaces, *ACS applied Materials & Interfaces*, 9 (2017) 21532-21538.

[20] E.M. Domingues, S. Arunachalam, J. Nauruzbayeva, H. Mishra, Biomimetic coating-free surfaces for long-term entrapment of air under wetting liquids, *Nature Communications*, 9 (2018) 3606.

[21] M. Mazaheri, D. Mari, R. Schaller, G. Bonnefont, G. Fantozzi, Processing of yttria stabilized zirconia reinforced with multi-walled carbon nanotubes with attractive mechanical properties, *Journal of the European Ceramic Society*, 31 (2011) 2691-2698.

[22] A. Datye, K.-H. Wu, G. Gomes, V. Monroy, H.-T. Lin, J. Vleugels, K. Vanmeensel, Synthesis, microstructure and mechanical properties of Yttria Stabilized Zirconia (3YTZP) – Multi-Walled Nanotube (MWNTs) nanocomposite by direct in-situ growth of MWNTs on Zirconia particles, *Composites Science and Technology*, 70 (2010) 2086-2092.

[23] R.C. Garvie, R.H. Hannink, R.T. Pascoe, Ceramic steel?, *Nature*, 258 (1975) 703-704.

[24] A. Tsoga, A. Gupta, A. Naoumidis, P. Nikolopoulos, Gadolinia-doped ceria and yttria stabilized zirconia interfaces: regarding their application for SOFC technology, *Acta Materialia*, 48 (2000) 4709-4714.

[25] I. Denry, J.R. Kelly, State of the art of zirconia for dental applications, *Dental Materials*, 24 (2008) 299-307.

[26] S. Yu, Q. Wu, M. Tabib-Azar, C.-C. Liu, Development of a silicon-based yttria-stabilized-zirconia (YSZ), amperometric oxygen sensor, *Sensors and Actuators B: Chemical*, 85 (2002) 212-218.

[27] J. Kim, Y.S. Lin, Sol-gel synthesis and characterization of yttria stabilized zirconia membranes, *Journal of Membrane Science*, 139 (1998) 75-83.

[28] P.B. Amama, A.E. Islam, S.M. Saber, D.R. Huffman, B. Maruyama, Understanding properties of engineered catalyst supports using contact angle measurements and X-Ray reflectivity, *Nanoscale*, 8 (2016) 2927-2936.

[29] E.F. Kukovitsky, S.G. L'Vov, N.A. Sainov, V.A. Shustov, L.A. Chernozatonskii, Correlation between metal catalyst particle size and carbon nanotube growth, *Chemical Physics Letters*, 355 (2002) 497-503.

[30] H. Dai, A.G. Rinzler, P. Nikolaev, A. Thess, D.T. Colbert, R.E. Smalley, Single-wall nanotubes produced by metal-catalyzed disproportionation of carbon monoxide, *Chemical Physics Letters*, 260 (1996) 471-475.

[31] A.G. Nasibulin, P.V. Pikhitsa, H. Jiang, E.I. Kauppinen, Correlation between catalyst particle and single-walled carbon nanotube diameters, *Carbon*, 43 (2005) 2251-2257.

Appendix C - Supplementary Information for Chapter 4

Table C4. 1 Deconvolution of XPS Co $2p_{3/2}$ peak for different cobalt catalysts.

Sample	Peak 1 (eV)	Peak 2 (eV)	Peak 3 (eV)	Peak 4 (eV)	Peak 5 (eV)
Co-Nit	778.32	780.13	781.91	785.45	788.49
Co-Ace	778.98	780.84	Not observed	785.10	788.34
Co-Chl	777.27	779.01	780.57	784.10	787.72
Co-Hyd	780.00	782.29	Not observed	784.07	787.01

Table C4. 2 Small/large particle density and particle size of different cobalt catalysts.

Catalyst	**Small Particle Density (Particle/μm²)**	**Large Particle Density (Particle/μm²)**	**Overall Particle Size (nm)**	**Small $d_{(Co3O4)}$[a] (nm)**	**Large $d_{(Co3O4)}$[a] (nm)**	**Large $d_{(Co3O4)}$[b] (nm)**
Co-Nit	19039	834	4.6	3.7	13.4	11.4
Co-Ace	9952	611	3.3	3.0	18.3	25.9
Co-Chl	17253	152	5.1	2.8	34.6	35.4
Co-Hyd	10869	228	4.7	4.0	20.4	25.7

[a]Average catalyst diameter from TEM

[b]Average crystallite size from XRD

Table C4. 3 Atomic percent of silica-supported cobalt catalysts from XPS results.

Sample	**O 1s**	**C 1s**	**Co 2p**	**Si 2p**	**Cl 2p**
Co-Nit	69.130	0.412	0.666	0.29792	Not observed
Co-Ace	67.948	2.026	2.297	27.729	Not observed
Co-Chl	37.175	49.847	1.837	10.918	0.196
Co-Hyd	57.195	9.331	14.810	18.664	Not observed

Table C4. 4 Selectivity of the fresh catalysts for the same CO conversion.

CO Conversion: 10%

Products / Catalysts	CH_4 (%)	C2 - C4 (%)	C5+ (%)
Co-Nit	N/A	N/A	N/A
Co-Ace	47	3	50
Co-Chl	47	2	51
Co-Hyd	N/A	N/A	N/A

CO Conversion: 17%

Products / Catalysts	CH_4 (%)	C2 - C4 (%)	C5+ (%)
Co-Nit	N/A	N/A	N/A
Co-Ace	41	3	56
Co-Chl	45	2	53
Co-Hyd	N/A	N/A	N/A

CO Conversion: 55%

Products / Catalysts	CH_4 (%)	C2 - C4 (%)	C5+ (%)
Co-Nit	22	19	59
Co-Ace	N/A	N/A	N/A
Co-Chl	N/A	N/A	N/A
Co-Hyd	43	2	55

CO Conversion: 60%

Products / Catalysts	CH_4 (%)	C2 - C4 (%)	C5+ (%)
Co-Nit	22	16	62
Co-Ace	N/A	N/A	N/A
Co-Chl	N/A	N/A	N/A
Co-Hyd	39	2	59

CO Conversion: 65%

Products / Catalysts	CH_4 (%)	C2 - C4 (%)	C5+ (%)
Co-Nit	17	10	73
Co-Ace	N/A	N/A	N/A
Co-Chl	N/A	N/A	N/A
Co-Hyd	35	3	62

Table C4. 5 EXAFS modeling results of local Co coordination numbers (CNs).

Sample	Co-O (1) CN	Co-O (2) CN	Co-Co CN	Co-Co (hcp) CN
Co-Nit (fresh)[a]	5.51 ± 0.49	4.28 ± 0.67	6.61 ± 0.98	Not observed
Co-Nit (used)[b]	2.87 ± 0.43	Not observed	3.80 ± 0.46	2.23 ± 0.29
Co-Hyd (fresh)[c]	4.99 ± 0.74	4.81 ± 0.97	4.96 ± 0.71	Not observed
Co-Hdy (used)[d]	6.52 ± 0.93	Not observed	3.51 ± 0.49	1.31 ± 0.25

[a] modelling performed with Co_3O_4 and an additional Co-O path from CoOOH
[b] modelling performed with CoO and hcp Co
[c] modelling performed with β-$Co(OH)_2$ and an additional Co-O path from CoOOH
[d] modelling performed with β-$Co(OH)_2$ and hcp Co

Table C4. 6 EXAFS modeling results of nearest neighbor distances (NNDs).

Sample	Co-O (1) NND (Å)	Co-O (2) NND (Å)	Co-Co NND (Å)	Co-Co (hcp) NND (Å)
Co-Nit (fresh)[a]	1.91 ± 0.01 Å	2.87 ± 0.01 Å	3.36 ± 0.01 Å	Not observed
Co-Nit (used)[b]	2.04 ± 0.02 Å	Not observed	3.01 ± 0.01 Å	2.52 ± 0.01 Å
Co-Hyd (fresh)[c]	2.05 ± 0.03 Å	2.83 ± 0.04 Å	3.15 ± 0.02 Å	Not observed
Co-Hdy (used)[d]	2.08 ± 0.02 Å	Not observed	3.13 ± 0.02 Å	2.50 ± 0.01 Å

[a] modelling performed with Co_3O_4 and an additional Co-O path from CoOOH
[b] modelling performed with CoO and hcp Co
[c] modelling performed with β-$Co(OH)_2$ and an additional Co-O path from CoOOH
[d] modelling performed with β-$Co(OH)_2$ and hcp Co

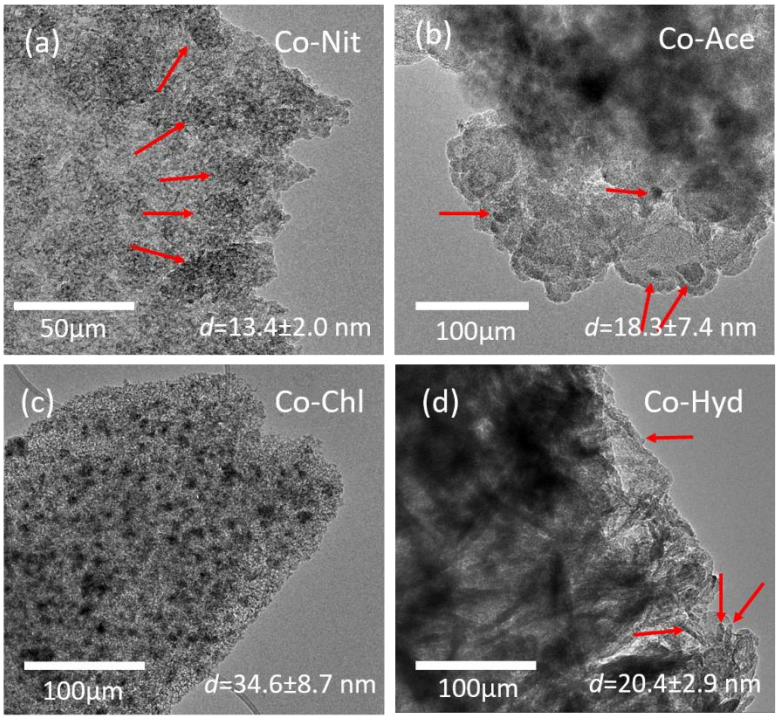

Figure C4. 1 Low-magnification TEM images of fresh silica-supported catalysts prepared from different cobalt precursors: $Co(NO_3)_2$ (a), $Co(C_2H_3O_2)_2$ (b), $CoCl_2$ (c), and $Co(OH)_2$ (d).

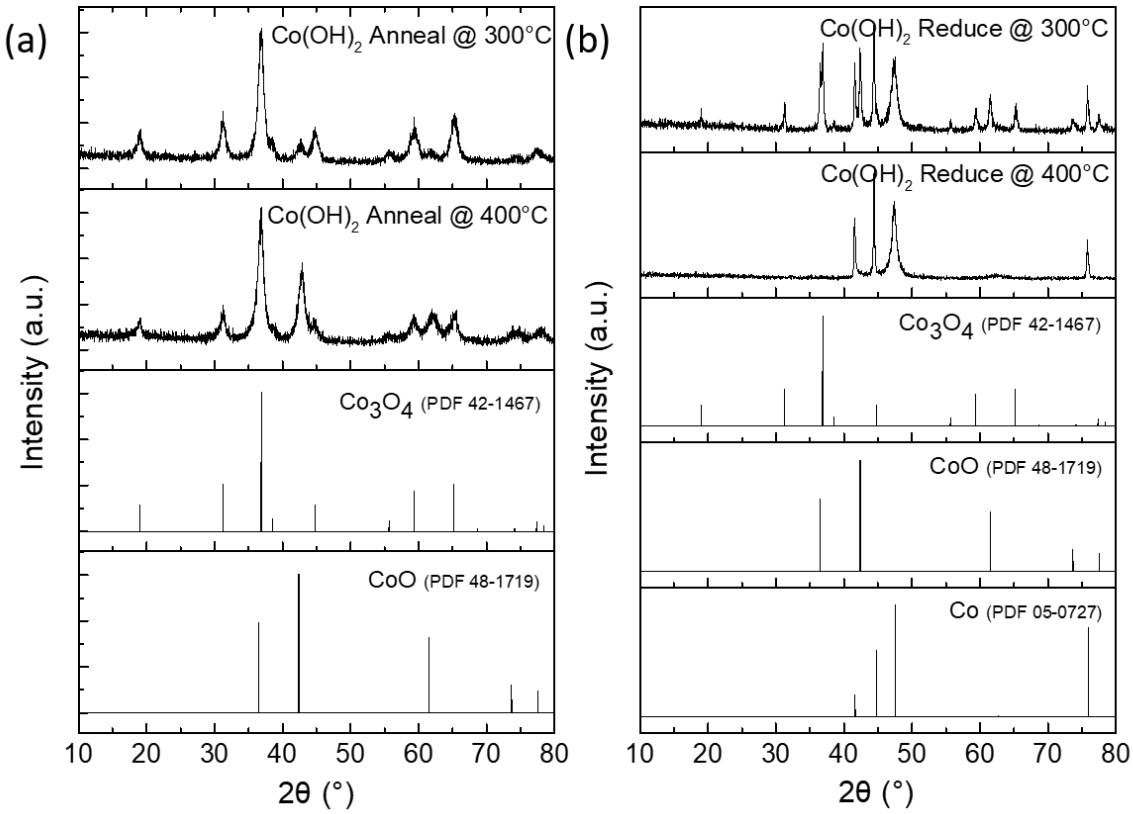

Figure C4. 2 XRD patterns of $Co(OH)_2$ annealed in both N_2 (a) and H_2 (b) at 300 and 400°C.

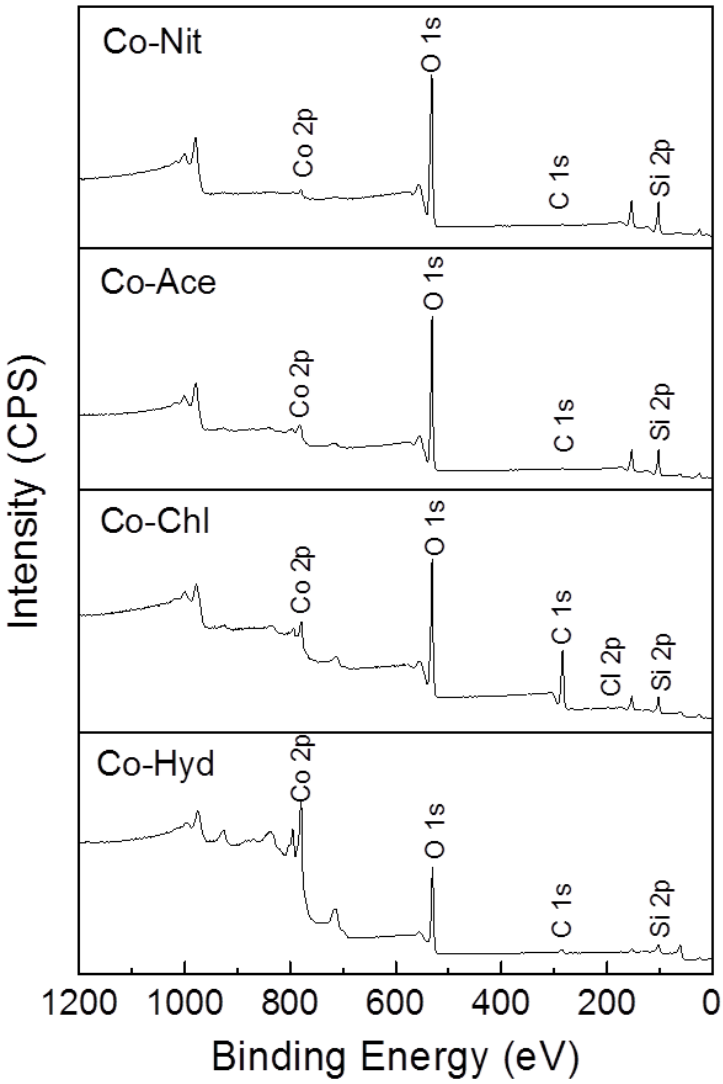

Figure C4. 3 XPS survey scan spectra of silica-supported cobalt catalysts prepared from different cobalt precursors.

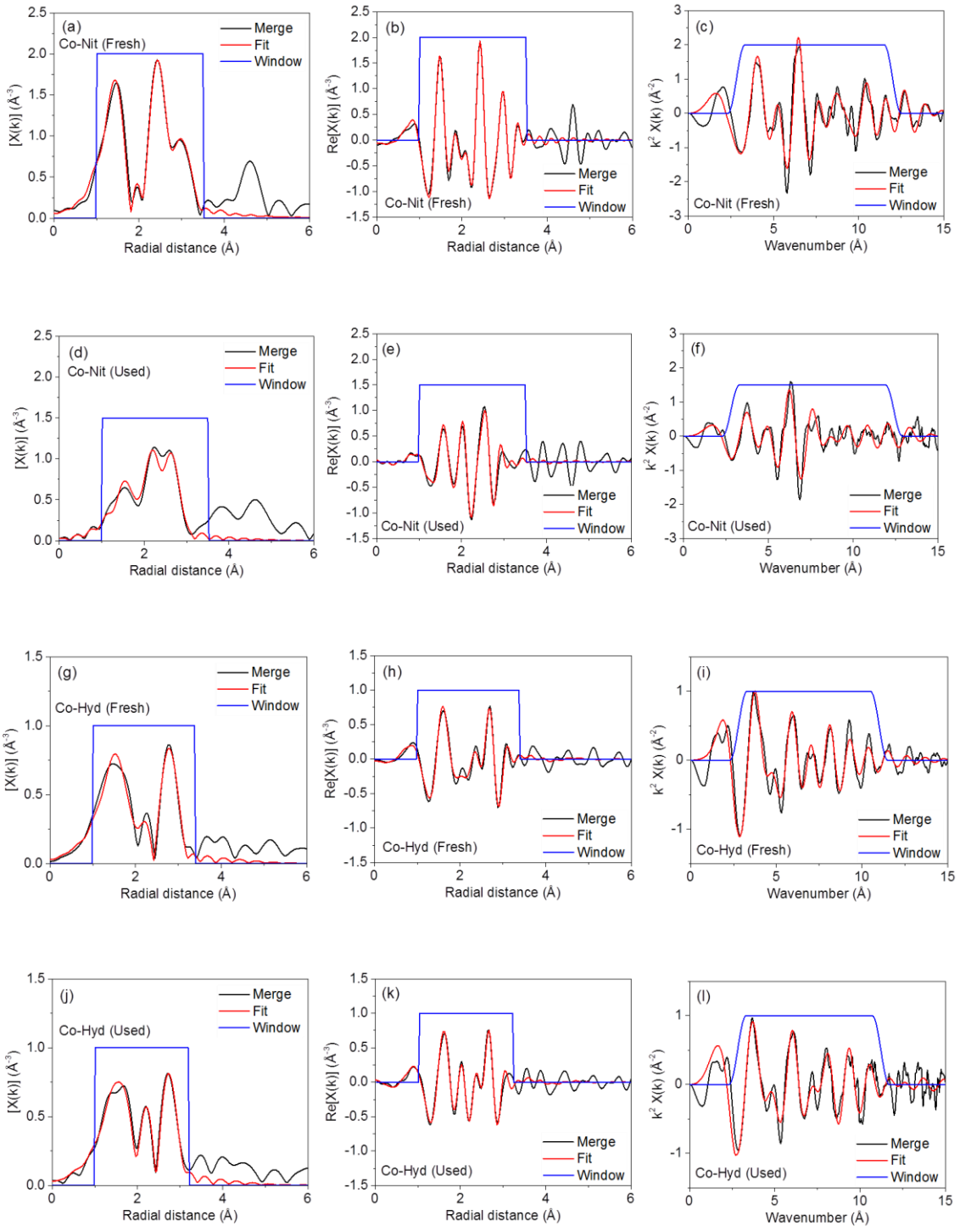

Figure C4. 4 Co K-edge modeling from EXAFS results of fresh Co-Nit catalyst merge in R space (a, b) and merge in k space (c), used catalyst Co-Nit catalyst merge in R space (d, e) and merge in k space (f), fresh Co-Hyd catalyst merge in R space (g, h) and merge in k space (i), used catalyst Co-Hyd catalyst merge in R space (j, k) and merge in k space (l) .